Aus der Universitätsklinik für Thorax-, Herz- und

Gefäßchirurgie Tübingen

Sektion Medizinische Werkstoffkunde und Technologie

Osteoblasts Response to Different UVA-activated Anatase

Implant Coatings

Inaugural-Dissertation

zur Erlangung des Doktorgrades

der Zahnheilkunde

der Medizinischen Fakultät

der Eberhard Karls Universität

zu Tübingen

vorgelegt von

Liang, Lanchen

2018

Dekan: Professor Dr. B. Autenrieth

1. Berichterstatter: Professor Dr. J. Geis-Gerstorfer

2. Berichterstatter: Professor Dr. M. Krimmel

Tag der Disputation: 08.01.2018

Contents

List of Tables

List of Figures

Contents

List of Abbreviations

ALB: albumin

ALP: alkaline phosphatase

ARS: Alizarin Red S

BIC: bone-implant contact ratio

BMP: bone morphogenetic protein

BMSCs: bone marrow stem cells

CAMs: cell adhesion molecule family

CB: conduction band

DPBS: Dulbecco's Phosphate Buffered Saline

e$^-$: electron

ECM: extracellular matrix

Erk: extracellular signal-regulated kinases

FAK: focal adhesion kinase

FGF: fibroblast growth factor

Fn: fibronectin

h$^+$: electron hole

IGFs: insulin growth factors

ISQ: Implant Stability Quotient

MAO: micro-arc oxidation

MAPK: mitogen-activated protein kinase

MB: methylene blue

PLC: Precursor based Liquid Film Coating

PVD: Physical Vapor Deposition

Ra: average roughness

RGD: arginine-glycine-aspartate tripeptide sequence

Rku: kurtosis (2D)

Rmax: maximum roughness height

Rmr: material ratio

Rq: root-mean-square (2D)

Rsk: skewness (2D)

Rz: average maximum height

S: sandblasted

S/A: sandblasted-acid etched

Sa: arithmetic mean height

Sal: autocorrelation length

Sc: core void volume

Sci: core fluid retention index

Sdq: root mean square surface slope

Sdr: developed interfacial area ratio

Sku: kurtosis (3D)

SPS: Suspension Plasma Spray

Sq: root mean square (3D)

Ssk: skewness (3D)

Str: texture aspect ratio

Sv: valley void volume

Svi: valley fluid retention index

TCPS: tissue culture polystyrene

TGF-β: transforming growth factor beta

UV: Ultraviolet

VB: valence band

VEGF: vascular endothelial growth factor

1. Introduction

1.1 Current challenges of dental implants

Dental implants have become widely used in the last decades in dentistry, not only because they improve patients' masticatory function to a great extent and reduce the amount of the preparation of natural teeth or even avoid the preparation compared to other restoration ways, but also on account of the optimal aesthetics and longevity they create. Pure titanium and its alloys are currently considered as ideal implant materials and widely used in clinical restorative procedures because of their optimal biocompatibility and machinability. Despite of this, a 3-6 months healing time has still been considered by dental specialists for years as the necessary condition for dental implants to integrate with bone in the human body. Owing to the development of design and surface modification technologies of dental implants, an increasing number of clinical studies on early and immediate loading of dental implants have been conducted and high survival rates were generally reported [1-3]. Even so, in clinical cases, many adverse conditions can yet compromise osseointegration and, thus, the treatment effectiveness of implantation. For example, the healing time of dental implantation in the posterior maxilla area is longer than that in the mandible, because the alveolar bone there consists only of a thin layer of cortical bone and a mass of low-density trabecular bone. The same issue with poor bone strength raises also for osteoporosis patients, most of whom are the elders and are the people most likely to receive implantation. A good osseointegration is the basis of the function of implants. Therefore, the continuative improvement of both the quality and the speed of osseointegration are prerequisites for the expansion of clinical indications.

1.2 A brief review of osseointegration

In order to improve osseointegration, it is necessary to understand how it proceeds in the first place. Several reviews from Davies [4], Terheyden et al. [5] and Salvi et al. [6] summarized the osseointegration process based on the cutting edge of research findings: after implantation, the water molecules take the lead in contacting the implant surface in the first few milliseconds, followed by proteins and other macromolecules, and finally the cells, which then adhere to the implant surface. Meanwhile, a thin and outermost layer of bone at the implantation site gets necrotic and disintegrates after implantation, including a large number of apoptotic cells and necrotic cells. The phagocytes from the immune system gradually digest and absorb this layer of bone, the tissue debris, and the oral bacteria that remain following the surgical procedure. In the first few days, primitive tissue (blood clot) between the bone and the implant is vascularized from the bony side. Meanwhile, bone absorption was simultaneous with osteogenesis. Osteoclasts, which are activated by a variety of inflammatory factors, attach themselves to the fracture edges of the residual bone, resorbing it and creating lacunas for bone formation. However, this will initially reduce the primary stabilization of the implant. Induced by cellular transforming factors, the undifferentiated mesenchymal stem cells and the osteoprogenitor cells migrate to the implant surface, adhere to it, and differentiate into osteoblasts. To the stimulation of growth factors, the osteoblasts proliferate, differentiate, and secrete extracellular matrix (ECM) proteins. After mineralization, woven bone is eventually formed, promoting increasing secondary stabilization of the implant. The contact osteogenesis coincides with the distance osteogenesis until they integrate into each other. After remodeling, the osseointegration forms at last between the new fused bone and the implant surface. At this time, the gap between the bone and implant surface is filled up by the reparative bone regeneration. This process is similar to the healing process of natural bone fractures. Clinically, the implant achieves a secondary stability eventually [7].

Professor Brånemark [8] summarized the above process as the "Osseointegration" in the 1980s: the formation of a direct interface between an implant and living bone, without intervening soft tissue, which is able to bear loading.

1.3 Interactions between the implant and the host at the interface

During osseointegration, different processes and interactions between the implant and the host tissue affect the rate or quality of osseointegration. Both the host and the implant surface influence these processes.

(1) Influence of the host

Once an implant is set in the body, its surface is immediately wetted by blood. Proteins, Lipids, Glycoproteins, and other biological macromolecules in the blood in consequence attach to the implant surface and form an adsorbed layer. Most of the biomolecules detach due to denaturation and degradation. However, a fraction of proteins and other molecules remain and are involved in regulating the response of the host bone tissue to the implant surface. Besides, the pre-osteoblasts that adhere on the implant surface also secrete specific bone matrix proteins, such as osteopontin, osteocalcin, and alkaline phosphatase, which are attached to the fibrin network [9]. This layer of protein also plays an important role in the adhesion of cells. Under the guidance of the adsorbed protein layer and a series of growth factors, the undifferentiated mesenchymal stem cells and the osteoprogenitor cells that come from the periosteum or the blood vessels [10] migrate onto the implant surface and adhere to it. The adhesion of these cells is a key element in osseointegration. It is the basis for the subsequent biological processes, such as the secretion of ECM proteins, the deposition of inorganic components and the formation, resorption and remodeling of bone.

During cell adhesion, the surface recognition by cells has aroused a great deal of interest. Since the type, configuration, and exposed functional groups of adsorbed proteins are regulated by the surface properties of the implant, cells can "read the information" that is transmitted from different implant surfaces through the adsorbed protein layer. This process of recognizing a surface is mediated by receptors on the cell membrane. Among the receptors, integrins are important members of the cell adhesion molecule family (CAMs). The extracellular domains of integrins can bind to ligands, such as the RGD adhesion motif, in the ECM and then cluster together to form a focal adhesion with the fibronectin in ECM [11]. The intracellular domains of integrins can recruit a series of structural proteins (including actin, vinculin, talin, tensin, paxillin, etc) and protein kinases (including focal adhesion kinase, mitogen-activated protein kinase, etc.). The focal adhesion links to the cytoskeleton through these proteins [12]. According to the composition and configuration of the adsorbed protein layer, integrins and the bound protein kinases activate several intracellular signaling paths, transforming the signals from ECM or implant surface to the cytoskeleton. Then the cytoskeleton reorganizes, and ultimately transfers the external stimuli into the nucleus, regulating the transcription and expression of genes related with cell spreading, proliferation, differentiation, and other behavior [13].

Several studies, for example by Ribeiro et al. [14] and Shen et al. [15], have been conducted to investigate the effect of the anodically oxidized rough titanium surface on the cytoskeleton organization of primary human osteoblasts by F-actin staining. The confocal fluorescence microscope images showed that, after two hours of cell culture, the cytoskeleton was actively rearranged, and the number of filaments increased. Compared to the annular filaments in the machined group that encompassed the nucleus, the coarse stress fibers in the roughened group penetrated the whole cell, and anchored to the sample surface through focal

adhesions on the cell membrane. Additionally, the cell morphology also showed a change from the rounded cell form to a fully spread-out and flat cell morphology. It is also well known that the osteoblasts can act as a "mechanical receptor" that can sense the external stress and subsequently lead to bone remodeling. Therefore, in clinical application, the immediate implantation and immediate loading procedures can affect the bone formation and remodeling by changing the stress on cells.

(2) Influence of the implant

From the machined surface in the early 80s of the last century to today's different surfaces modified by a variety of physical and chemical treatments, a main purpose of implant surface modification has been to enhance the osseointegration. It has been found that [16-22] the type, configuration, and exposed functional groups of the adhered proteins are interactively regulated by the following surface characteristics: roughness, surface morphology, chemical, and wettability.

Many researches have shown that rough surfaces can enhance the mechanical interlocking of fibrin in blood clots, resulting in better stabilization and fixation of early extracellular matrix scaffolds, and subsequently improving the migration, adhesion, and proliferation of osteoblasts on the implant surface. Besides, the micro-nano-topography of the implant surface is also one of the key factors that influence osseointegration. One related phenomenon is that a favorable topography can promote and accelerate bone formation by contact guidance. Studies [23] have shown that nano-topography plays an important role in protein adsorption, osteoblast adhesion and the improvement of osseointegration. Although currently roughening treatments are the state of the art of implant surface modification, some researchers [24, 25] have suggested that the increase

in the incidence of peri-implantitis might be inseparable from the widely used rough surface implants. The rough surfaces offer a hotbed for bacteria to reproduce. The concern for the clinical problems associated with rough surface implants is reasonable. However, it still requires further basic and clinical research to verify.

The roughening surface treatment can only improve osteoconduction of implants, but not the osteoinduction. With the development of coating techniques, the modification of the surface composition is used to improve the osteoinduction of implants. One type of chemical modification methods is to coat inorganic substances, such as hydroxyapatite, on a titanium substrate to promote bone formation, e.g. by electrochemical deposition, micro-arc oxidation, plasma spraying or other methods. Another widely investigated approach is to anchor specific proteins, enzymes, or peptides to the implant surface to induce the differentiation of osteoblasts. Theoretically, the anchored biological factors have a significant effect on the proliferation and differentiation of osteoblasts, so this method is more effective than the conventional physical or chemical surface treatments. The bioactive molecules that are currently adopted can be generally divided into:

1) Extracellular matrix, such as collagen I and chondroitin sulfate, etc. [26, 27];

2) Growth factors, such as bone morphogenetic protein (BMP), transforming growth factor beta (TGF-β), insulin growth factors (IGFs), fibroblast growth factor (FGF) and vascular endothelial growth factor (VEGF), etc. [28, 29];

3) Cell adhesion molecules, such as fibronectin and bone sialoprotein that contain the arginine-glycine-aspartate (RGD) tripeptide sequence. This sequence has been proven to regulate the adhesion of osteoblasts on the implant surface principally [30, 31].

At present, common biomolecule coatings are either hydrogel coatings, which are manufactured by directly adsorption of biomolecules onto the surface of the implant, or the layer-by-layer self-assembly coatings, which are formed through entrapping biomolecules within many polyelectrolyte layers on the implant [32]. For the hydrogel coatings, it is difficult to control either the loading efficiency or the release kinetics. A local overdose of these directly coated biomolecules is prone to induce the malignant transformation of host cells. For the layer-by-layer coatings, although their release kinetics can be controlled by changing processing parameters, the technique is, however, labor intensive, costly, and delamination is likely to occur during surgical procedures. Therefore, the application of biomolecules to implant surface modification still requires further investigations, and is still rare in clinical use.

1.4 Oxide layer of titanium

Besides osseointegration, an understanding of the surface features of titanium is also indispensable to ameliorate the titanium implant. Once the titanium is exposed to the air after manufacturing, it will immediately and automatically start to form a layer of tight titanium oxide. In the oxide layer, titanium exists in the form of Ti^{2+}, Ti^{3+} and Ti^{4+}, respectively, corresponding to TiO, Ti_2O_3 and TiO_2. The vast majority of the maturely formed oxide, however, is TiO_2. Titanium dioxide possesses favorable physical, chemical, and mechanical properties, such as a high dielectric constant that is close to water, stable chemical properties, good corrosion resistance, high hardness, etc. It exists in nature mainly as three well-known mineral forms, rutile, anatase, and brookite. Among them, brookite is relatively scarce, and its physicochemical properties are not fit for application. Anatase and rutile are most commonly technically used and are generally applied as paint pigment, oxygen sensor, photocatalyst, antibacterial layer, etc. Both of them crystalize in the tetragonal system. Each crystal lattice consists of a centric

titanium ion and six surrounding oxygen ions, which forms a TiO_6 octahedron. The difference between the two is that the octahedrons are connected in different ways. In anatase, the octahedrons share four edges with other octahedrons. In rutile, the octahedrons share two edges. According to the Paulin's rules, the more edges the coordination polyhedron shares, the less stable the structure is. Therefore, rutile is most widely distributed among the three variants in nature. Another intriguing character of TiO_2 is the photocatalytic activity for its promising use in generating a bioactive surface for osseointegration. Although both anatase and rutile exhibit significant photocatalytic activity, the anatase form has been demonstrated to be more active [33]. Besides, compared to the crystal forms of TiO_2, amorphous TiO_2 almost shows no photocatalytic activity. In the manufacturing, different crystal structures form with different sintering temperatures. Amorphous structure forms without heating. Anatase crystals generally exist in the low manufacturing temperature. When the temperature is increased to 800℃ or more, all anatase crystals will be converted into rutile crystals. Therefore, the oxide layers of different titanium implants come in many varieties with different proportions of amorphous TiO_2 and crystalline TiO_2 depending on the manufacture techniques.

Metal can corrode in complex environments in the human body and the accompanying corrosion products can be released to the surrounding tissue, triggering systemic or local acute or chronic inflammatory responses, or even a cytotoxic response, and ultimately may give rise to implant failure. Although titanium is an active metal, the solid titanium oxide layer provides a very stable surface that is tolerated by the human body and maintains a passive state in physiological circumstances. This ensures a long-term coexistence of titanium with hosts, so that the calcified bone matrix can be deposited on it. This feature of titanium is the basis of the high biocompatibility of titanium dental implants [34].

However, in the meanwhile, the exposure of the titanium surface to ambient air can also cause "biodegradation" or "biological aging" [35]. The term "time-dependent degradation" refers to the fact that the bioactivity of the titanium surface is continuously decreasing with time elapsing after the surface treatment and exposure to the air. The freshly treated titanium surface is weakly positively charged and has a high surface energy and biological activity. The surface is relatively pure and without organic impurities which can interfere with protein adhesion. Att et al. [35] demonstrated that the "fresh" surface performed better than the 4-week-old surface in the perspective of protein adhesion, cell attachment, and bone-implant contact ratio, which showed that the fresh surface had a higher biological activity compared to the "aged" surface. Additionally, Massaro et al. [36] manifested that the titanium surface can be contaminated by organic substances during exposure to air. These pollutants affected the bioactivity of the surface, thus affecting the osseointegration. Shibata et al. [37] also demonstrated that the adhesion of osteoblasts to the aged surface was significantly reduced due to the attachment of organic impurities, while UV irradiation could effectively remove these organic impurities.

1.5 UV-induced photocatalysis of titanium dioxide

Several approaches are investigated to overcome the undesirable decreased osteoconduction of the titanium implants due to "biodegradation" during storage. Among them, ultraviolet-induced photocatalysis of titanium dioxide is considered as a promising and elegant chair-side procedure to switch the "aged" titanium implant surface from bioinert to bioactive.

(1) Principles of UV-induced photocatalysis of TiO$_2$

In the energy band theory, the energy bands for solids, in which all the outer electrons are, can be hypothetically divided into conduction band (CB) and

valence band (VB). The VB is the highest extent of electron energies at absolute zero, where electrons are bound by nuclei. The CB is the lowest extent of vacant electronic states, where electrons can move freely. The energy range that lies between the VB and CB is the band gap, where no electron states can exist. TiO_2 possesses the characteristics of a semiconductor [38]. The energy bands of semiconductors are typically composed of an electron-filled VB and an empty high-energy CB. When the energy absorbed by the semiconductor exceeds the range of the band gap, the electron (e^-) is excited and jumps from VB to CB, and the corresponding electron hole (h^+) in VB is generated. The electrons move freely in the CB. Under an external electric field, they can move with a direction, which means conductivity. Anatase has a band gap of 3.2 eV at pH = 1. In this case, the wavelength of the radiation necessary for the excitation of electrons is:

1240 (Planck's constant × Velocity of light) / 3.2eV (band gap energy)

= 387.5 nm

Ultraviolet (UV) light is an electromagnetic radiation with a wavelength from 100 to 400 nm, in which the range with wavelengths of 100 ~ 280 nm is termed UVC, the range with wavelengths of 280 ~ 315nm is termed UVB, and the range with wavelengths of 315 ~ 400nm is termed UVA. According to the calculated radiation wavelength above, the energy of UV with the wavelength less than 387nm is able to excite electrons to jump over the band gap of anatase, producing photogenerated electron-hole pairs [39]. The generated h^+ breaks apart the water molecule to form hydroxyl radicals. The e^- reacts with oxygen molecules to form a series of strong reducing agents, e.g. super oxide anions, which can also form hydroxyl radicals in the presence of water. These reactions continue as long as irradiation is available. The photocatalytic mechanism by TiO_2 can be described as follows [40]:

$TiO_2 + h\nu \rightarrow e^- + h^+$

$h^+ + H_2O \rightarrow \cdot OH + H^+$

$h^+ + OH^- \rightarrow \cdot OH$

$e^- + O_2 \rightarrow \cdot O_2^-$

$\cdot O_2^- + H_2O \rightarrow \cdot OOH + OH^-$

$2 \cdot OOH \rightarrow H_2O_2 + O_2$

$\cdot OOH + H_2O + e^- \rightarrow H_2O_2 + OH^-$

$H_2O_2 + \cdot O_2^- \rightarrow \cdot OH + OH^- + O_2$

$H_2O_2 + e^- \rightarrow \cdot OH + OH^-$
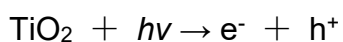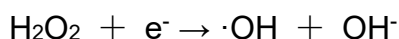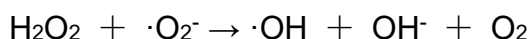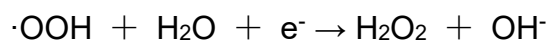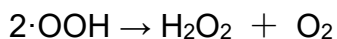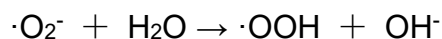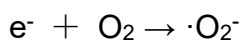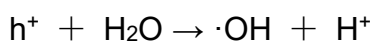
According to the law of conservation of energy, if the electrons in CB and the holes in VB recombine together, this potential energy will transform into thermal or other forms of energy.

(2) Mechanisms of bioactivity improvement of photocatalysed TiO$_2$

1) Decomposition of organic contamination on the titanium surface

The highly reactive agents produced by the photocatalytic reactions promptly interact with any organic contaminant present at the irradiated anatase surface. They attack the carbon hydrogen bonds, which are present in organic molecules and accelerate the decomposition of pollutants into water and carbon dioxide through oxidation. Rupp et al. [41] used XPS to investigate decomposition of organic contaminants on aged anatase surfaces by UV photocatalysis. XPS results confirmed that the photoelectron peak of the hydroxyl group increased significantly after UV irradiation. In the meanwhile, the amount of aliphatic hydrocarbons strongly decreased. This antipollution property of photocatalytic TiO$_2$ creates a clean and fresh surface for proteins and cells to adhere by removing the obstacles of organic contamination.

2) Improvement in wettability

The TiO_2 layer on titanium surfaces is hydrophobic after storage and shows a water contact angle around 72° at 300K. UV photocatalysis is considered effective in improving the wettability of titanium oxide surfaces [42]. Rupp et al. [43] demonstrated that the freshly-processed acid-etched titanium surface is initially superhydrophilic. However, after exposure to ambient conditions, the contact angle of acid-etched titanium could exceed 50° [44]. Al Qahtani et al. [45] manifested that, after 40 minutes UVA exposure, the advancing contact angle of an anatase-coated implant decreased from 111° to 0°. All of these results indicated that UV photocatalysis increases the hydrophilicity of titanium.

One convincing mechanism of photoinduced superhydrophilicity of TiO_2 is that the photocatalytic degradation, as described above, decomposes the organic compounds that are rather hydrophobic, and provide a hydrophilic surface for water molecules to adsorb. Another possible mechanism is the adsorption of ·OH to oxygen vacancy generated by photocatalysis [46]. The presumed mechanism of superhydrophilicity can be divided into three steps. At first, electron-hole pairs are created by excitation during UV irradiation of TiO_2. In a usual photocatalytic reaction, these electron–hole pairs react with the water or oxygen that adhere to the surface and produce highly reactive agents. However, in the condition of photoinduced superhydrophilicity, the superficial TiO_2 molecule itself is reduced from Ti^{4+} to Ti^{3+}, accompanying with the generation of an oxygen vacancy.

$e^- + Ti^{4+} \rightarrow Ti^{3+}$

$4h^+ + 2O^{2-} \rightarrow 2O_2$
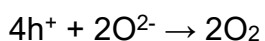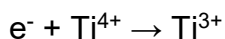
Although this Ti^{3+} can be oxidized by oxygen in the air, these oxygen vacancies generated by the reduction can also be occupied with water molecules in the air, resulting in a hydroxyl group layer on the surface that serves as a chemisorbed water layer. These hydroxyl groups can further absorb water in the air to form a

physisorbed water layer. When blocking the UV illumination, the reverse reaction takes place and the surface reverts to the hydrophobic state.

To verify this theory, researchers compared TiO_2 with another photocatalyst $SrTiO_3$ [47]. The results showed that these two photocatalysts possess similar photocatalytic activity in the degradation of methylene blue. However, the photoinduced hydrophilicity can be only achieved on TiO_2, indicating that the improvement of wettability is not only caused by the photocatalytic degradation of the organic compounds but also may be due to the surface chemistry changes. Although these two phenomena can occur simultaneously on the titanium oxide surface, they are in essence two different processes. In concrete circumstances, the hydrophilicity may not correlate with the photocatalytic activity.

Owing to the increasing hydrophilicity, both the protein adsorption and the cell attachment enhance, leading to improved implant biocompatibility and osseointegration. Hirakawa et al. [48] illuminated anatase-coated titanium disks and implants with UV for 24 hours. After UV treatment, the superhydrophilic surface exhibited enhanced adsorption of serum fibronectin. Moreover, the bone-to-implant contact ratio of the experimental group was also twice as much as that of the control group after two weeks of healing. It is widely shared that the UV irradiation is a promising method to induce superhydrophilicity of titanium implants, which is a beneficial property for osseointegration.

3) Transformation of the electrostatic status of the TiO_2 surface

As long understood [49], TiO_2 surfaces are electronegatively charged. Proteins, e.g. serum albumin, and cells are also electronegative at physiological pH values, so they are repelled at the TiO_2 surface. Therefore, divalent cations, such as Ca^{2+}, must first bridge the gap between the TiO_2 surface and proteins that in turn can

13

attract cells via RGD-integrin interaction. Yet at the same time, some monovalent cations, such as Na^+, which competitively bind to the titanium surface, may block the anion sites, and subsequently prevent proteins and cells from adhering to this part of binding sites. However, the UV treatment could helpfully switch the aged TiO_2 surface from electronegative to electropositive [50]. This positively charged surface could attract anionic proteins to bind without assistance of divalent cations, or even directly attract the anionic cells to attach without protein in between. It showed a shift of the TiO_2 surface from bioinert to bioactive, which significantly enhanced the quantity and speed of both serum albumin adsorption and osteoblast adhesion to the titanium surface [51].

(3) Effect of UV-induced photocatalysis of TiO_2 on osseointegration

In vitro studies, animal studies and clinical studies confirmed the improvement of biological capabilities of titanium surface by UV-induced photocatalysis.

In vitro, Miyauchi et al. [52] observed cytoskeletal proteins of osteoblasts on the titanium oxide surface after UV irradiation by rhodamine staining. The results showed that, in the control group, there was no pseudopod with microfilament after culture for three hours, and the cells were round. However, more internal microfilaments and pseudopods were observed in the irradiated group, and the cells were irregularly shaped, showing a better cellular adhesion. Besides, the results of the single cell detachment experiment also confirmed that the shear force of osteoblast adhesion after UV treatment was significantly higher than that before irradiation. Shayan et al. [53] proved that the adhesion and proliferation of osteoblast cells on the $PMMA/TiO_2$ surface were significantly increased by UVA irradiation even after four-hour treatment. Tsukimura et al. [54] and Hori et al. [55] observed the cell behavior of rat bone marrow-derived osteoblasts on TiO_2 surfaces with either micropits alone, or micropits with 100-nm, 300-nm, or 500-

nm nodules, before and after UV treatment. The results demonstrated that UV irradiation could improve cell adhesion, spreading, proliferation, and mineralization. The nanonodular surfaces, besides, further enhanced the biological capabilities above and showed a synergistic effect with UV irradiation. Moreover, Kawano et al. [56] came to the same conclusion that UVA exposure with a wavelength of 365 nm significantly enhanced the proliferation of osteoblast cells on the anatase surface. In their animal studies, anatase coated specimens in the shape of cylindrical rod (φ 2 mm × 5 mm) were inserted into the femurs of Wistar rats. The histological observation of tissue sections after one month of implant placement revealed an obvious increase of new bone formation around specimens with UVA illumination. The area of new-formed bone without illumination was less than 0.1 mm^2 per section and increased to more than 0.2 mm^2 with UVA treatment. Additionally, the bone-implant contact (BIC) ratio also showed a significant enhancement. After four weeks of healing, the mean BIC ratio with UVA irradiation was close to 90%, whereas that of the non-irradiated group was about 60%.

So far, there is only one split mouth clinical study [57] available as a conference abstract, aiming at investigating whether UV-irradiated dental implants show faster osseointegration with higher implant stability compared to untreated dental implants. Forty patients received two implants each. On one side, the implant with 15-minute UVA pretreatment was placed, and on the other side, the original implant was settled. Implant Stability Quotient (ISQ) is an objective standard for evaluating implant stability. According to Sennerby et al. [58], >70 ISQ is high stability, between 60-69 is considered as medium stability, and low stability means < 60 ISQ. Therefore, ISQ values and bone loss were measured immediately after implantation and at one week, one month, and three months following implant placement. It was observed that UVA illumination accelerated

and enhanced osseointegration. A significantly lesser marginal bone loss was also detected around the irradiated implants.

In conclusion, ultraviolet-induced photocatalysis of TiO_2 shows a favorable prospect in clinical application.

1.6 Effect of morphology of the implant surface on osseointegration

The process of osseointegration involves a variety of cells and biomolecules. The speed and quality of osseointegration depend on the cellular behavior largely. An increasing number of studies have shown that the surface morphology plays a very important role in the regulation of cellular behavior. Thus, the effect of the implant surface morphology on osseointegration is another non-negligible consideration in this study.

According to the dimension, the surface morphology of dental implants can be divided into macroscale, micrometer scale, and nanometer scale morphology. Studies [59, 60] have shown that micromorphology improved the bone regeneration. Many implant surfaces with micromorphology, such as sandblasted and acid-etched surfaces, have been applied clinically. The related clinical studies revealed that these implants exhibited favorable osseointegration and achieved superior clinical outcomes compared to implants with machined surfaces [61, 62]. In this case, the increasing contact area and the enhanced mechanical interlocking between implant and bone may induce the improvement of osseointegration. Besides, Hansson et al. [63] proposed that osteoblasts could act as mechano-biosensors. The stimulation caused by the implant micromorphology could regulate cellular behavior through cell signaling pathways. Although the surfaces with micromorphology display a comparatively high bioactivity, it is generally believed that their ability of regulation is relatively limited.

Recently, it has been found that when the surface roughness of implants is at nanometer scale (1-100 nm), the nanomorphology can directly regulate the ECM composition and cellular behavior compared to the morphology at macro- or micrometer scale. Biomaterials with nanomorphology are closer to the histomorphology of natural bone tissue [64]. Natural bone tissue has a composite morphology that contains nanoscale size elements. The extracellular matrix of bone contains two main components: organic collagen fibers and inorganic mineral. Collagen is composed of tropocollagen helices with a length of 300 nm and a width of about 1.5 nm. The hydroxyapatite is also in nanoscale size. The average crystal size is 10 - 50 nm in woven bone, or with a diameter of 2 - 5 nm and a length of 20 - 50 nm in lamellar bone [65]. Besides, Palin et al. [66] even measured the surface roughness of cortical bovine bone by atomic force microscopy and showed that the root-mean-square (Rq) value was also approximately 32 nm. Additionally, the microenvironment in vivo consists of nanoscale structures as well, such as the basement membrane that is composed of concaves, protrudings, pores, and fibers with a size of 50-200 nm [67]. Therefore, from the perspective of bionics, the surface with nanomorphology can simulate the structure of natural bone tissue better, which provides an ideal environment for bone regeneration. In view of this, controlling cellular behavior by nanostructured materials during osseointegration has drawn increasing attention. Researchers have developed various nanostructured implant surfaces, such as nanocrystalline hydroxyapatite coatings [68] and titanium surfaces with different nanostructures [69, 70]. The results showed that cells could sensitively perceive the nanomorphology, which significantly enhanced the alkaline phosphatase (ALP) activity and the mineralization of bone ECM of both osteoblasts and bone marrow stem cells (BMSCs).

Although a large number of studies have confirmed the improvement of osseointegration caused by nanostructured surfaces, the crucial roles of micromorphology in the primary stability of implant cannot be negligible. Meirelles et al. suggested that nanomorphology alone is not sufficient to induce stable osseointegration [71]. Moreover, natural bone tissue consists of macroscopic nanocomposites that are composed of cancellous bone and cortical bone at macroscale, Haversian system at microscale and collagen fibrils, non-collagenous organic proteins, and hydroxyapatite at nanoscale. These indicate that it is promising to optimize the design of micro- and nanomorphology of implant surfaces based on the mechanisms of the interaction between cells and micro-nanomorphology.

1.7 Aim of the study

As we introduced above, UV-induced photocatalysis of TiO_2 is a feasible and convenient processing option to increase the biological activity of titanium implant surfaces and ultimately to benefit the osseointegration process. The photocatalysis reaction rate of TiO_2 is determined by many influencing factors [72]. An important one is the crystalline form of TiO_2. It is generally approved that the anatase crystal form exhibits higher photocatalytic activity than other forms. Nevertheless, there are several manufacturing methods that can be applied in producing anatase coatings. These various kinds of anatase coatings have different proportions of the crystalline forms and different surface morphologies. So far, although many anatase coatings have been investigated, no study has been made to compare the performance of anatase coatings produced by different manufacturing methods. Therefore, in this study, we investigated the surface characteristics of three differently manufactured anatase surfaces, namely a Suspension Plasma Spray (SPS) surface, a Precursor based Liquid Film Coating (PLC) surface and a Physical Vapour Deposition (PVD) surface.

Besides, we also compared the biological response of human osteoblast cells to them with that to a conventional sandblasted (S) and a sandblasted-acid etched (S/A) titanium implant surface, in order to eventually seek for the most effective anatase modification method to enhance osseointegration.

2. Materials and Methods

2.1 Titanium samples preparation and surface modification treatments

Commercially pure Ti (unalloyed, grade 4) disks with a diameter of 10 mm and a thickness of 1 mm were provided by Dentaurum GmbH & Co. KG (Pforzheim, Germany). The initial, basic treatment applied to all samples was a sandblasting process. Based on this sandblasted (S) surface, the disks were further treated by four different surface modification processes: 1) Acid etching (S/A), 2) Suspension Plasma Spraying (SPS), 3) Precursor based Liquid film Coating (PLC) and 4) Physical Vapor Deposition (PVD) by Institute for Manufacturing Technologies of Ceramic Components and Composites (Stuttgart, Germany). The (S/A) treatment leads to a typical blasted and etched titanium surface while the latter three treatments result in different anatase-enriched surfaces.

Surface characterization and cell culture experiments, described below, laid an emphasis on anatase coated specimens (SPS, PLC, PVD), while titanium samples with a native oxide layer (S, S/A) were used as reference surfaces. Prior to the experiments, all disks were stored in glass Petri dishes covered by aluminum foil under ambient temperature and pressure for more than 3 weeks.

Study of Implant Surfaces				
Group 1	Group 2	Group 3	Group 4	Group 5
sandblasted	sandblasted	sandblasted	sandblasted	sandblasted
	acid-etched	suspension plasma spraying (SPS)	precursor based liquid film coating (PLC)	physical vapor deposition (PVD)
Reference 1 (S)	Reference 2 (S/A)			

Anatase Coating Variants
(new experimental surfaces)
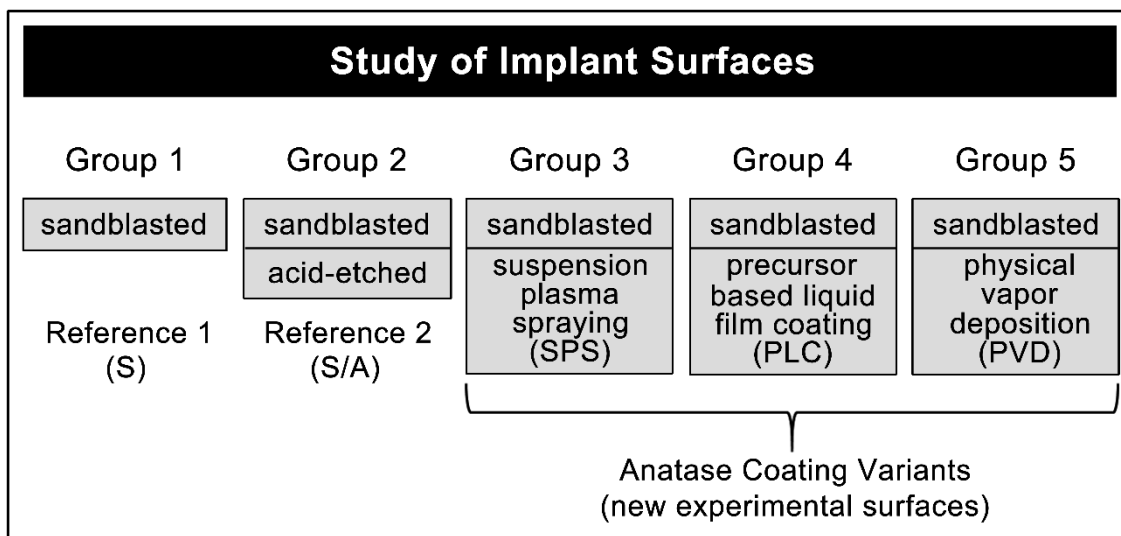
Fig. 2- 1 The grouping of the study

2.2 Surface characterization

(1) Scanning electron microscopy

The three dimensional surface morphology of the samples was visually displayed by a scanning electron microscope (LEO 1430, LEO Electron Microscopy Ltd, England). A photo of the microscope system is in Fig. 2- 2.

Samples were first fixed on holders. A fraction of the sample margin and the adjacent holder were connected with liquid silver paint to make the non-conductive sample surfaces electrically conductive. Then the samples were centered with holders on the stage of the sputter coater (Sputter Coater SCD 050, Bal-Tec, Switzerland). A photo of the sputter coater is in Fig. 2- 3. The chamber was first rinsed with argon a couple of times to remove unwanted gasses, especially water vapor. Then samples were coated for 100 sec with a current of 60 mA to achieve a black Au-Pd coating with a thickness of 20 nm. During coating, a vacuum was produced and maintained in the sealed chamber of the coater.

After coating, samples were placed in serial order into the scanning electron microscope, which was operated at an accelerating voltage of 20 kV in a vacuum. Representative areas for each kind of sample surface were selected and photodocumented at 500 x, 1.000 x, and 5.000x magnification, respectively. Moreover, higher magnification pictures (10.000x and 50.000 x) were kindly provided by Institute for Manufacturing Technologies of Ceramic Components and Composites (Stuttgart, Germany).
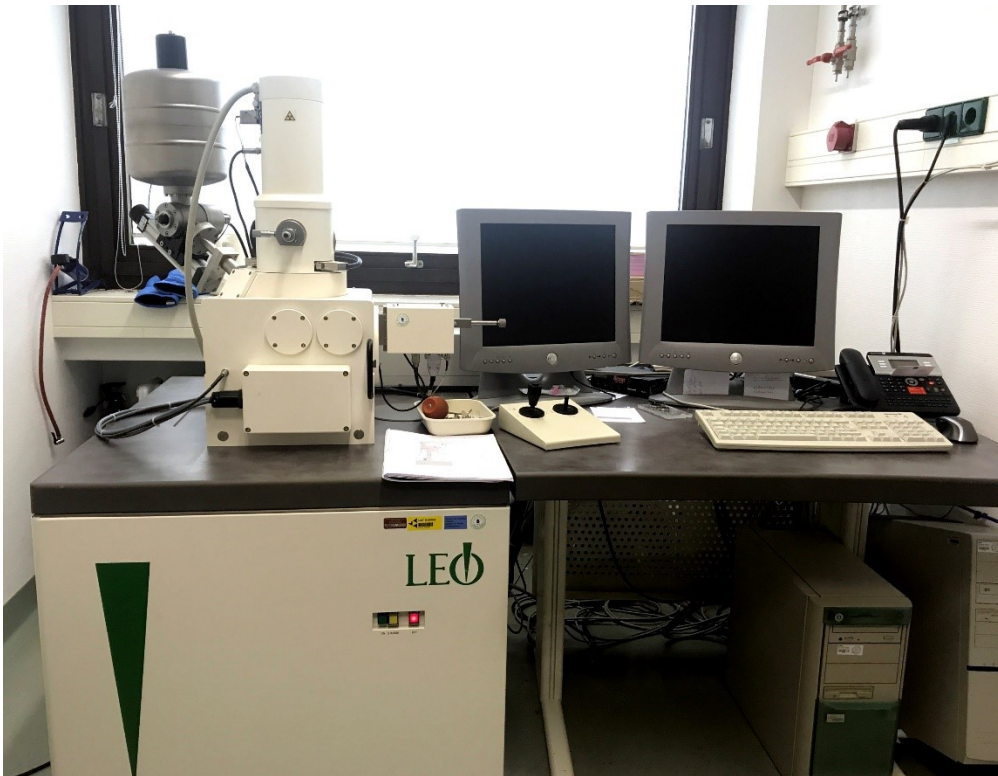
Fig. 2- 2 Scanning electron microscope "Leo 1430"
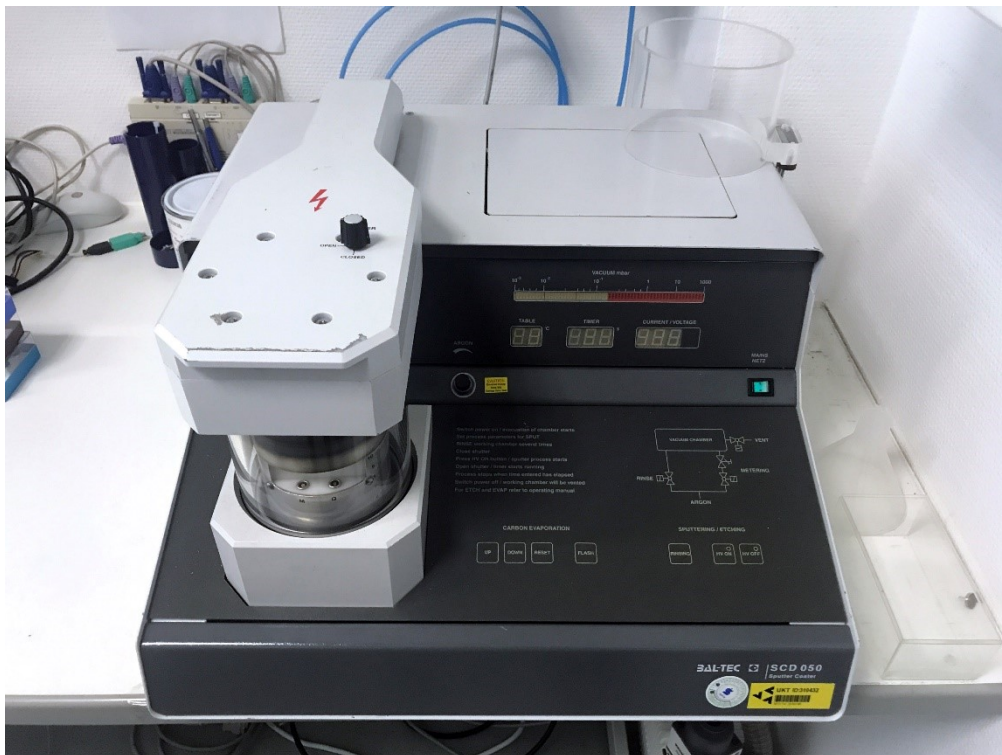
Fig. 2- 3 Sputter deposition system " Balzers Sputter Coater SCD 050"

(2) Surface roughness analysis

From each surface type, five samples were investigated. The three dimensional surface contours of the specimen were measured by a surface texture measurement system (Perthometer PRK, Mahr, Germany). A simplified schematic diagram of the Perthometer is illustrated in Fig. 2- 4. A photo of this system is in Fig. 2- 5.

Samples were first fixed horizontally on the platform of the Perthometer. An area of 3 mm × 3 mm of each sample was measured for the roughness data. Raw profiles were recorded every 25 µm. In other words, 121 raw profiles with 3 mm length each were collected. Then, after correcting the tilt of the samples, a high-pass Gaussian filter of 0.8 mm was applied to separate microscale roughness from form and waviness. A series of two-dimensional roughness parameters were calculated by a surface analysis software (Mountainsmap Universal, Digital Surf, France) according to the standard DIN EN ISO 4287. The details of different roughness parameters are described in Tab. 2- 1.
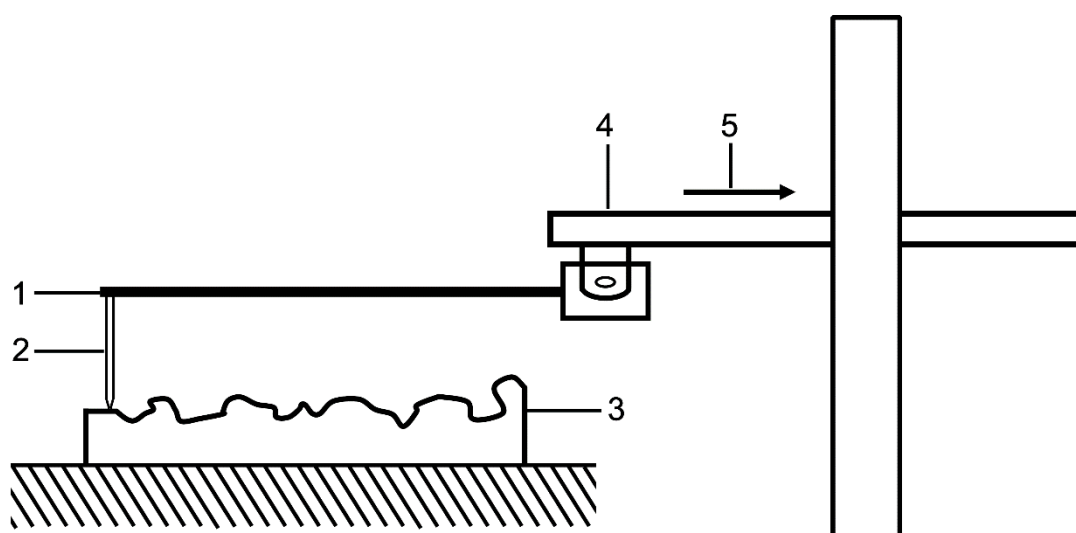
Fig. 2- 4 Schematic diagram of the Perthometer (1 – tracing arm; 2 – stylus; 3 – measuring object; 4 – drive unit; 5 – measuring direction)
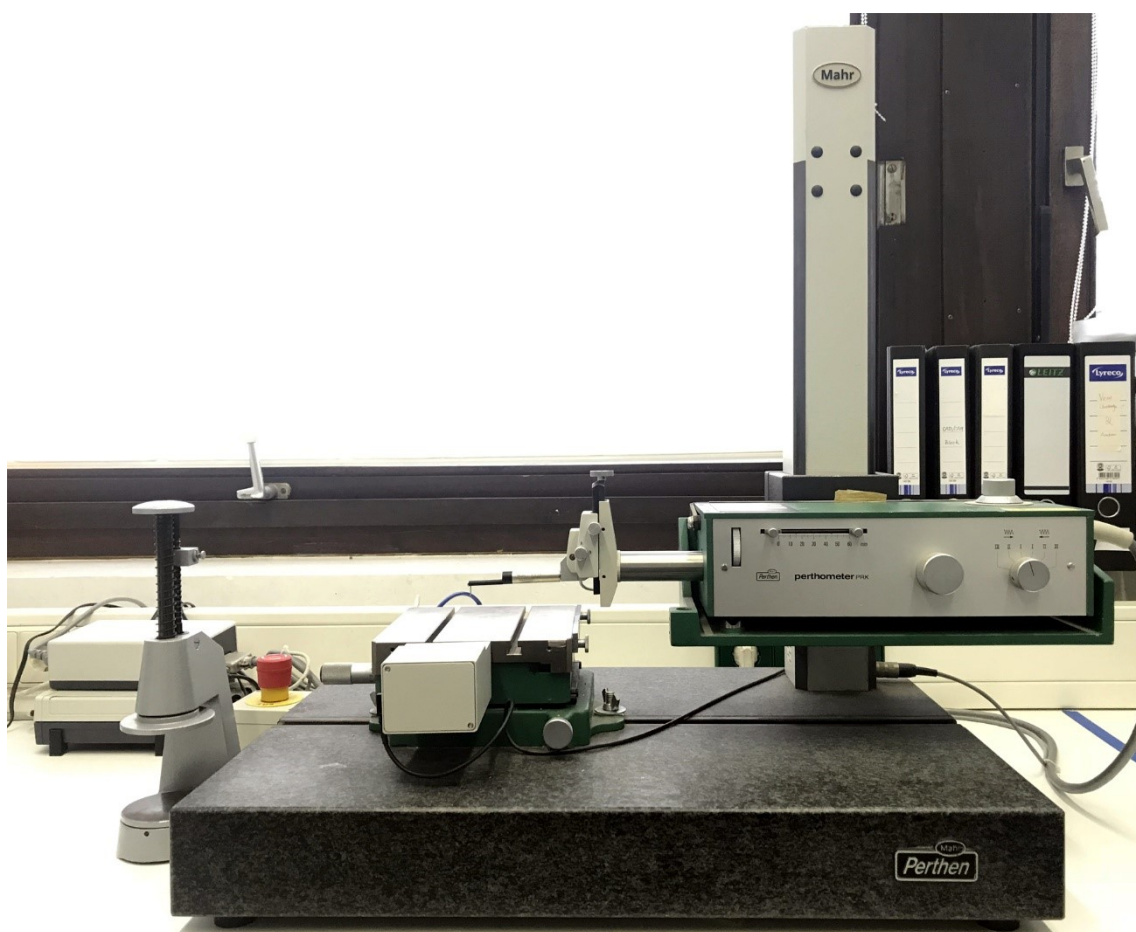
Fig. 2- 5 Surface texture measurement system "Perthometer"

To further characterize surface roughness properties, the three-dimensional roughness was measured by means of optical interference (Bruker ContourGT-K, Bruker, Germany). The relevant parameters were calculated according to the standard DIN EN ISO 25178 by Institute for Manufacturing Technologies of Ceramic Components and Composites (Stuttgart, Germany). The details of 3D roughness parameters are described in Tab. 2- 2. We selected this range of parameters that might be able to describe and explain the investigated biological behavior.

Tab. 2- 1 Description of two-dimensional roughness parameters

Name	Symbol	Description	Mathematical	Type
Average roughness	R_a	arithmetic mean of the absolute ordinate values Z(x) of roughness profile	$R_a = \dfrac{1}{l}\displaystyle\int_0^l \lvert Z(x)\rvert\,\mathrm{d}x$	Amplitude
Average maximum height	R_z	arithmetic mean value of the single maximum roughness height Rzi within a sampling length	$R_z = \dfrac{1}{n}(R_{z1} + R_{z2} + \cdots + R_{zn})$	Amplitude
Maximum roughness height	R_{max}	the maximum single roughness height within the evaluation length	/	Amplitude
Skewness	R_{sk}	asymmetry of the amplitude density curve	$R_{sk} = \dfrac{1}{R_q^3}\left[\dfrac{1}{l}\displaystyle\int_0^l Z^3(x)\,\mathrm{d}x\right]$	Amplitude
Kurtosis	R_{ku}	peakedness of the amplitude density curve	$R_{ku} = \dfrac{1}{R_q^4}\left[\dfrac{1}{l}\displaystyle\int_0^l Z^4(x)\,\mathrm{d}x\right]$	Amplitude
Material ratio	R_{mr}	ratio of the material-filled length at a specified height c (cut level) to the evaluation length, l_n	$R_{mr} = \dfrac{1}{l_n}(L_1 + L_2 + \cdots + L_n)\%$	Functional

Tab. 2- 2 Description of three-dimensional roughness parameters

Name	Symbol	Description	Mathematical	Type
Arithmetic mean height	S_a	arithmetic mean of the absolute value of the height within a sampling area, A	$S_a = \frac{1}{A} \iint_A \left| Z(x,y) \right| dx\, dy$	Height
Root mean square (RMS) height	S_q	root mean square value of the surface departures within the sampling area	$S_q = \sqrt{\frac{1}{A} \iint_A \left| Z(x,y) \right| dx\, dy}$	Height
Skewness	S_{sk}	asymmetry of the amplitude density curve	$S_{sk} = \frac{1}{S_q^3} \left[\frac{1}{A} \iint_A Z^3(x,y)\, dx\, dy \right]$	Height
Kurtosis	S_{ku}	peakedness of the amplitude density curve	$S_{ku} = \frac{1}{S_q^4} \left[\frac{1}{A} \iint_A Z^4(x,y)\, dx\, dy \right]$	Height
Autocorrelation length	S_{al}	horizontal distance of the ACF(tx, ty) which has the fastest decay to a specified value s, with 0≤s<1	$S_{al} = min\sqrt{tx^2 + ty^2}$	Spatial
Texture aspect ratio	S_{tr}	ratio of the horizontal distance of the ACF(tx,ty) which has the fastest decay to a specified value s to that which has the slowest decay to s, with 0≤s<1	$S_{tr} = \dfrac{min\sqrt{tx^2 + ty^2}}{max\sqrt{tx^2 + ty^2}}$	Spatial

(continued)

Root Mean Square Surface Slope	S_{dq}	root mean square of the surface gradient within the evaluated area, A	$S_{dq} = \sqrt{\dfrac{1}{A} \iint_A \left(\dfrac{\partial z^2}{\partial x} + \dfrac{\partial z^2}{\partial y}\right) dx\, dy}$	Hybrid
Developed interfacial area ratio	S_{dr}	ratio of the increment of the area of the evaluated surface over its projected area, A	$S_{dr} = \dfrac{\sum\sum A_{ij} - A}{A} \times 100\%$	Hybrid
Core void volume	S_c	void volume provided by the unit sampling area, enclosed from 10% to 80% of surface bearing area	$S_c = \dfrac{V_v(h_{0.10}) - V_v(h_{0.80})}{(M-1)(N-1)\, dx\, dy}$	Functional
Core fluid retention index	S_{ci}	ratio of the void volume of the unit sampling area at the core zone (5% - 80% bearing area) over S_q	$S_{ci} = \dfrac{1}{S_q}\left[\dfrac{V_v(h_{0.05}) - V_v(h_{0.80})}{(M-1)(N-1)\, dx\, dy}\right]$	Functional
Valley void volume	S_v	void volume provided by the unit sampling area, enclosed from 80% to 100% of surface bearing area	$S_v = \dfrac{V_v(h_{0.80}) - V_v(h_{1.00})}{(M-1)(N-1)\, dx\, dy}$	Functional
Valley fluid retention index	S_{vi}	ratio of the void volume of the unit sampling area at the valley zone (80% - 100% bearing area) over S_q	$S_{Vi} = \dfrac{1}{S_q}\left[\dfrac{V_v(h_{0.80})}{(M-1)(N-1)\, dx\, dy}\right]$	Functional

(3) Corrosion immersion test

To evaluate the corrosion behavior of different anatase surfaces, five specimens of each kind of surface were immersed in tubes of artificial saliva (0.1M NaCl, 0.1M Lactic acid, pH 2.3) at 37℃ (ISO 10271) separately. The artificial saliva was changed after 1-, 4-, 7-, 14-, 21-, 28-, 35- and 42-day immersion. The immersion solutions were collected and the ion release of titanium element from the samples was measured after each collection by an inductively coupled plasma optical emission spectrometry (Optima 4300 DV, PerkinElmer, America). A photo of the optical emission spectrometry is in Fig. 2- 6. The means of the absolute mass loss and the cumulative mass loss of titanium and their standard deviations were calculated. The surface morphology of each kind of sample was also recorded by SEM as described above.

Fig. 2- 6 ICP-optical emission spectroscopy "Optima 4300 DV"

(4) UVA-irradiation

Before the respective experiments, samples in the corresponding groups should be photofunctionalized by UVA irradiation.

First, we adjusted the irradiation dose of the UVA irradiation box (UVACube 100, Dr. Hönle AG UV Tech, Germany) by a UV-Meter (Dr. Hönle AG UV Tech, Germany). The illumination dose of the irradiation box is adjustable by changing the distance between the UV lamp on the top of the box and the lifting platform in the curing chamber. Therefore, we fixed the sensor of the UV-Meter on the platform and changed the platform height until the UV-Meter showed the anticipated illumination intensity (25 mW/cm^2). Then the height of the platform was fixed during the entire experimental process, so that every photofunctionalized sample received the same dose of UVA irradiation.

The titanium disks were treated with UVA (382 nm, 25 mW/cm^2) in the irradiation box immediately before each respective experiment for up to 30 minutes. Photos of the UVA irradiation box and the UV-Meter are in Fig. 2- 7 and Fig. 2- 8 respectively.

Fig. 2- 7 UVA irradiation box "UVACube 100"

Fig. 2- 8 UV-Meter

(5) Sessile-drop contact angle measurement

Two sets of samples each containing 15 samples (three from each of the five specimen types) were stored for three and six weeks, respectively, in petri dishes in the dark at normal pressure and temperature to simulate "aging" of the titanium surfaces. Wettability was quantified by water contact angles measured by a high-resolution drop shape analysis system (DSA 10-MK 2, Kruess, Germany) before and after UVA irradiation. A photo of the analysis system is in Fig. 2- 9.

After three and six weeks, respectively, the stored samples were first removed from the petri dishes and a sessile drop of two-microliter ultrapure water was mounted on each sample with a microsyringe. After 30 seconds wetting time, the contact angle of the air-water-substrate interface was quantified from the respective drop geometry using the DSA calculation software (version 1.90.0.11, Kruess, Germany) and the whole wetting process was recorded by the same software. Afterwards, the same batch of samples was completely dried in a nitrogen stream and was irradiated by UVA as described before for 30 seconds. Immediately after irradiation, the water contact angle was measured once again as represented above. Then, this process was repeated three more times, the irradiation time is 30 seconds for the first two times and 510 seconds for the last time. That is to say that the accumulated irradiation time before each batch of measurements are 30 seconds, 60 seconds, 90 seconds, and 600 seconds, respectively.

Drop shape analysis was performed on the three samples from each specimen type and the averages and standard deviations of the water contact angles were calculated. The drop shape on each sample was also photographed. Wettabilities of samples with different storage time, with different surface modification methods, and with different irradiation duration were compared separately.
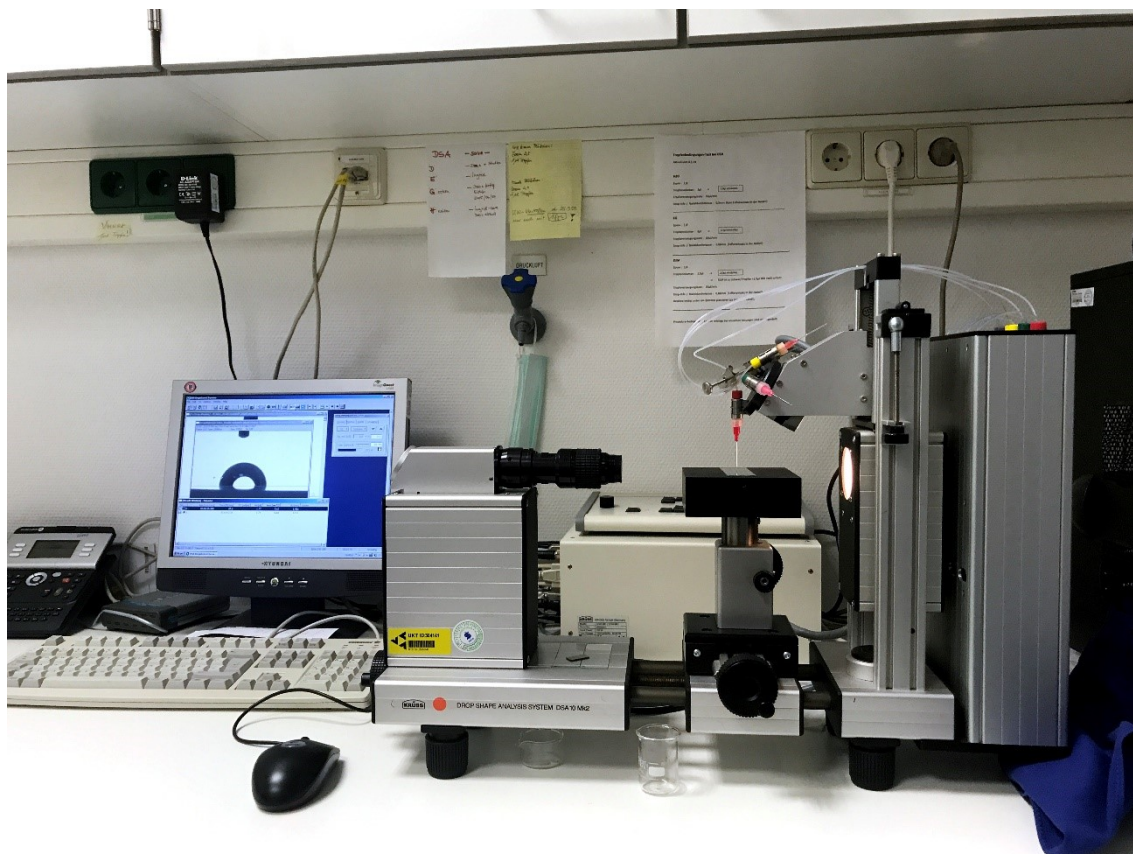
Fig. 2- 9 Drop shape analysis system "DSA 10-MK 2"

(6) Photocatalytic activity measurement

The photocatalytic activity of the specimens was assessed by measurement of methylene blue (MB) photodecomposition. Eight samples from each specimen type were separately incubated in 500 μl 20 μM aqueous MB conditioning solution and stored in the dark over night to allow pre-adsorption of MB to saturate the surfaces of samples and wells. The pre-adsorption step minimizes the artificial error of photocatalytic activity, caused by adsorption. On the following day, the MB conditioning solution was first removed. Then the samples were rinsed with 500 μl of a 10 μM MB measuring solution once and then placed in 250 μl MB measuring solution. Working solutions (20 μM and 10 μM) were prepared using a 1% methylene blue stock solution (Epignost GmbH., Germany) and pyrogenfree water (Ampuwa, Germany). UVA irradiation of four samples from

each group was conducted as described above, while four other samples from the same group were stored in the dark as references. After every ten-minute irradiation, 200 µl MB measuring solution was removed from each well, and the absorbance of the solution at 620 nm was measured in an ELISA reader (EAR 340 ATTC, SLT Lab. Instruments, Austria). After measurement, the solution was returned to the respective sample well and the UVA irradiation was continued. The irradiation was carried out for 30 minutes in total, thus the absorbance measurements were repeated three times in the whole experimental process.

Except for photocatalysis, the evaporation of water caused by the high ambient temperature during irradiation also influenced the concentration of MB, which subsequently affected the photocatalysis reaction rate. In order to keep the results with different irradiation time comparable, every time after the measured solution was returned, the volume of evaporated water from each well was calculated individually according to the weight loss measured by a laboratory electronic balance (Laboratory LC 4800 P, Sartorius, Germany). Then the corresponding volume of pyrogen-free water was filled accordingly to ensure that there was 250 ml solution in each well every time before the irradiation started.

This experiment was repeated two times. The absorbance change of the measuring solution for each sample group was then averaged and the respective rate constants of the photocatalysis reaction were calculated.

2.3 Cell culture model and assays

(1) Cell culture

SAOS-2, a human osteogenic sarcoma cell line, was obtained from German Collection of Microorganisms and Cell Cultures GmbH (DSMZ, Braunschweig, Germany). Cells were cultured in culture flasks (CellBind T-75, Corning, USA) in McCoy's 5A medium (Sigma-Aldrich, USA), supplemented with heat-inactivated 15% fetal bovine serum (Gibco, USA), 1% L-glutamin (Gibco, USA) and 1% penicillin and streptomycin (Gibco, USA), at 37 ℃ in an atmosphere of 5% CO_2 and 95% humidity in a cell incubator (Heracell™ 150i, Thermo Fisher Scientific, USA).

As for cell subculture, the spent culture medium was first removed and discarded from the flask. Then the cells were washed by 10 ml Dulbecco's Phosphate Buffered Saline (DPBS, Gibco, USA) to remove residual serum, calcium and magnesium that inhibit cell dissociation. The DPBS was gently added to the side of the flask opposite the attached cell layer to prevent disturbance to the cells. After the flask was rocked back and forth several times to completely rinse, the DPBS was removed and discarded from the flask. Then 1.5 ml pre-warmed trypsin-EDTA was added to the side of the flask. The flask was again gently rocked to get complete coverage of the trypsin-EDTA on the cell layer. Then the flask was incubated at 37℃ for 3-5 minutes. When more than 90% of the cells were detached, 5 ml pre-warmed complete medium (McCoy's 5A) was added to stop dissociation and was dispersed several times by pipetting over the cell layer. Afterwards the cells were transferred to a 15 ml conical tube and a 10 μl sample was removed for cell counting. A disposable hemocytometer chip (DHC-N01, NanoEnTek, USA), a mechanical piece counter (T123 IVO, Checkline Europe, Netherlands) and an inverted microscope (CK2, Olympus, Japan) were used to

determine the total number of cells and to calculate the concentration of the single-cell suspension. Then the appropriate volume of cell suspension was dispensed into a new T-75 flask and was diluted with fresh culture medium to 10 ml. Then the flask of cells were returned to the incubator. The subcultivation ratio is 1:3, and the seeding density is about 5 X 10^5 cells per flask (T-75). The cells were passaged, when they reached 80% confluence, normally two times per week.

Before cell biology experiments, the cells were subcultured several times until a consistent growth rate was achieved and the cells were in good health status and showed reproducible behavior. All the procedures of cell culture and assays were conducted in a clean bench (LaminAir HB 2472, Heraeus, Germany).

(2) Saos-2 cell proliferation assay

Eight samples from each anatase coated group (SPS, PLC, PVD) and four samples from each reference group (S, S/A) were placed in 48-well tissue culture plates. To distinguish between effects caused by irradiation regime, and effects caused by the altered surface structure of the anatase-coated samples compared to the reference surfaces, the anatase lots were divided in half. Four samples were irradiated by UVA for 10 minutes to achieve hydrophilicity immediately before seeding the cells, the other four were used without irradiation. Since the previous measurement of methylene blue photodecomposition has proven that the photocatalytic activity of the reference surfaces was negligible compared to the anatase surfaces, all the samples in the reference groups were also used without irradiation. Four other specimens from each group acted as background controls without cells. Four vacant wells were applied as tissue culture polystyrene (TCPS) proliferation controls and three other wells were used as blank that contained neither samples nor cells.

35

After group dividing and irradiation, SAOS-2 cells were seeded at a density of 30.000 cells/cm^2 on the experimental samples and TCPS controls, and were incubated for 24 hours with 300 µl complete medium per well before measurements. Since the well diameter of the plates was 11 mm, the samples with a diameter of 10 mm almost completely covered the bottom of the wells, which ensured that the vast majority of cells were seeded on the sample surfaces. After the incubation period, 150 µl of the premixed XTT labeling reagent was added to each well. The final XTT concentration was 0.3 mg/ml. The microplates were then incubated at 37 ℃ in an atmosphere of 5% CO_2. After an appropriate incubation time, 300 µl mixture of the XTT reagent and the medium from each well was transferred into a 96-well tissue culture plate. The absorbance was then measured spectrophotometrically by the ELISA reader at 492 nm with a reference wavelength at 620 nm. The mitochondrial dehydrogenase activity of cells was repeatedly quantified 24, 48, 72, and 96 hours after seeding with the XTT Cell Proliferation Kit II (Roche, Switzerland). A photo of the kit is in Fig. 2- 10. The culture medium was changed every 24 hours at the end of each activity measurement. The appropriate incubation time lengths, which were 2-4 hours normally, were varied from day to day during experiments, and were determined by the rate of color development. We optimized the incubation time to ensure that the color intensities in different wells were in the range that the absorbance differences could be measured sensitively by the ELISA reader (between 0.5 and 1.5 preferably). To account for the different incubation times for color development, absorbance values were modified as OD / hour.

The whole experiment was repeated three times. The modified means and standard deviations of the optical density of different samples were calculated under the consideration of the different reaction times. Additionally to the absolute values, the relative XTT reduction rates, referring to the original sandblasted

group, were calculated. For this purpose, the modified mean OD value of the sandblasted group at each time point was set to 1.0, and the modified means of other groups at the same time point were divided by this value for better comparison.
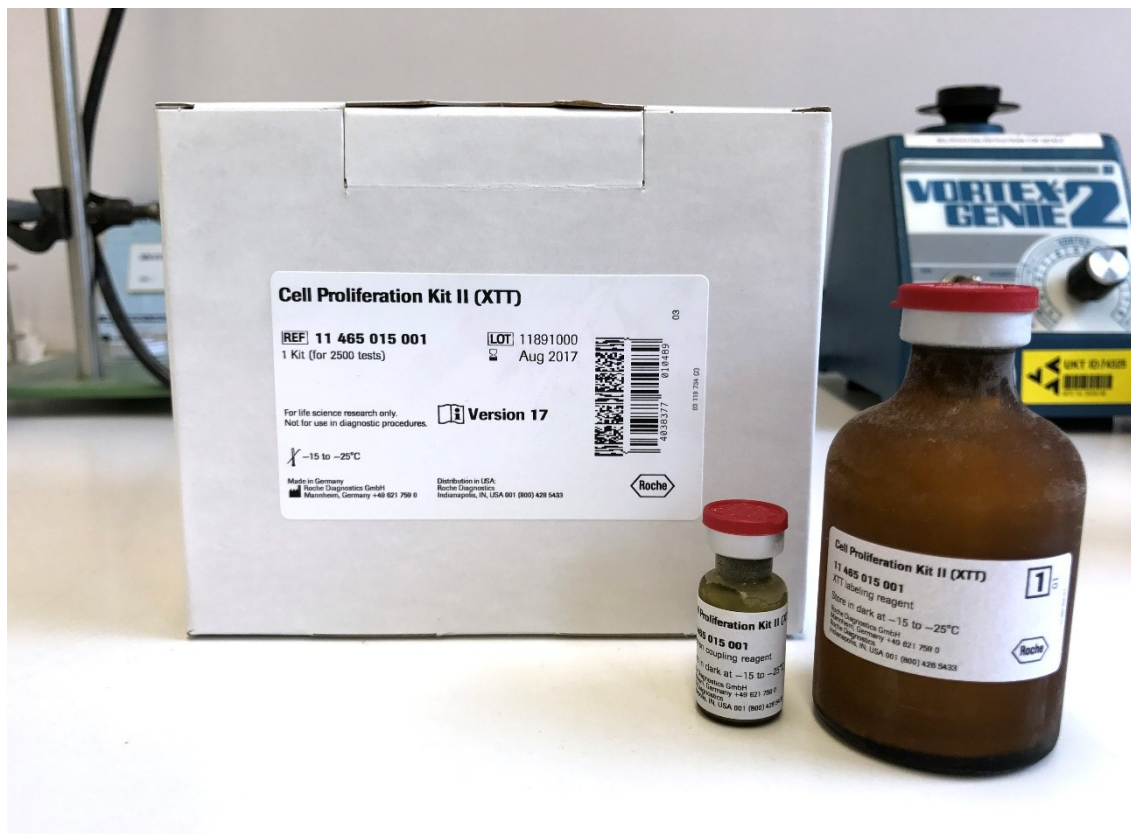
Fig. 2- 10 Cell Proliferation Kit II (XTT)

(3) Surface coverage measurement

After four days in culture, the experimental samples, as well as background controls, TCPS controls and blank groups in the proliferation assay were subjected to measurement of the cell coverage of sample surfaces. Immediately after the proliferation assay, each well was rinsed with 400 μl Hank's Salt Solution (Biochrom AG, Germany) to remove unattached cells. Then the adhering cell layer was fixed with 400 μl 3% paraformaldehyde (MERCK, Germany) in DPBS (Gibco, USA) for 15 minutes at room temperature. After the aldehyde fixative was

removed and discarded, the wells were washed with distilled water three times. Subsequently, each well was stained with 200 µl 0.5% crystal violet dye (Sigma-Aldrich, USA) in 20% methanol (MERCK, Germany) solution for 15 minutes at room temperature. Then each well was thoroughly rinsed with 400 µl distilled water at least three times. Photographs of the sample surfaces were taken with a zoom macroscope (M400, Wild Heerbrugg, Switzerland) equipped with a digital single lens reflex (EOS 500D, Canon, Japan) and the EOS Utility software program. Subsequently, all samples were transferred into a new 48-well plate except for the TCPS and blank groups that cannot be transferred. The cell-staining dye in each well was solubilized with 250 µl pure methanol (MERCK, Germany) for 15 minutes at room temperature. The samples were turned over in the wells during dissolution to ensure the dyes were completely dissolved. When the discoloration of all cells was observed through the macroscope, 230 µl of the dissolving solution from each well was transferred into a 96-well plate. The absorbance was measured at 550 nm in the ELISA reader.

This experiment was also repeated three times. The averages and standard deviations of the optical density of different sample stains were calculated and compared.

(4) Osteogenic differentiation assay

Alizarin Red S (ARS) staining was used to identify mineralized depositions as specific marker for osteogenic maturation. Twelve samples from each anatase coated group (SPS, PLC, PVD) and six samples from each reference group (S, S/A) were placed in 48-well tissue culture plates. As in the proliferation assay, to distinguish between effects caused by the irradiation regime or by the altered surface structure, the anatase specimens were divided in half. Six samples were irradiated by UVA for 10 minutes to achieve hydrophilicity immediately before cell

seeding; the other six were used without irradiation. Samples in reference groups were not irradiated. The influence of the surface morphologies and the irradiation treatment on mineralization was investigated under two different conditions:

1) cells incubated in normal, non-inducing medium, the complete McCoy's 5A medium (Sigma-Aldrich, USA);

2) cells cultured in "osteogenesis inducing" medium, the complete McCoy's 5A medium, supplemented with 100 µM L-ascorbic acid 2-phosphate, 10 mM β-glycerol phosphate disodium, and 4 µM dexamethasone (all from Sigma-Aldrich, USA).

Six specimens of different surfaces in irradiated group and non-irradiated group, respectively, were divided equally again to culture cells in the two respective media. Besides, three other specimens for each kind of surfaces were used as background controls without pretreatment and cell seeding. The TCPS controls and blank groups were also set as before.

After group dividing and irradiation, SAOS-2 cells were seeded at a density of 30.000 cells/cm^2 on the samples and were first incubated for 24 hours with 300 µl complete medium per well before induction. The next day, 500 µl of either osteogenic-induced medium or non-induced medium was added respectively into corresponding wells. The cells were grown for three weeks with medium replacement 2-3 days a time. After 21 days of culture, media were discarded and the degrees of osteogenic differentiation were determined by ARS staining.

Cells were first gently rinsed with 500 µl Dulbecco's phosphate-buffered saline (DPBS, without calcium and magnesium, Gibco, USA) two times and fixed with 500 µl 3% paraformaldehyde (MERCK, Germany) in DPBS (Gibco, USA) for 30 minutes at room temperature. After the formalin solution was removed gently but completely, cells were rinsed with 500 µl double distilled water three times and

stained with 500 µl 40 mM ARS (Sigma-Aldrich, USA) in sterile water (Ampuwa, Germany) (pH = 4.1, adjusted by hydrogen chloride) for 30 minutes with gentle shaking at 37 ℃. Then ARS solution was completely removed and wells were thoroughly rinsed with 750 µl double distilled water four times, at least five minutes each time. The stained calcium depositions were then visualized by the macroscopic photography system that was mentioned before. During these procedures, all reagents were added and removed gently and indirectly to the cell layers to avoid the detachment of cells.

For ARS quantification, 0.5 M hydrogen chloride (HCl, MERCK, Germany) supplemented with 5% sodium dodecyl sulfate (SDS, Sigma-Aldrich, USA) was added to each well for 30 minutes with gentle shaking at room temperature to elute the bound stain. Light absorbance of the extracted dye was subsequently quantified at 405 nm by the ELISA reader.

This experiment was repeated two times. The averages and standard deviations of the optical density of different sample stains were calculated and compared.

2.4 Statistical analysis

Statistical analyses were performed with SPSS Version 23.0 statistical analysis program (SPSS Inc., USA). Paired student's t-test was used to analyze the significant differences between the samples with the same surfaces but different treatments, e.g. before and after UVA irradiation. One-way analysis of variance followed by Student-Newman-Keuls test (with equal variances) or Dunnett's T3 test (with unequal variances) was used to perform multiple comparisons among the groups with different sample surfaces. Unless otherwise indicated, all data were presented as $\bar{x} \pm s$ and the differences were regarded as statistically significant at $p < 0.05$.

3. Results

3.1 Surface characterization analyses

(1) Surface morphological characterization

The morphology of each kind of tested surfaces was characterized by SEM images along with a photo of the whole sample. The sandblasted (S) surface (Fig. 3- 1) showed irregular, angular facets in appearance of valleys and peaks caused by the sand blasting process. Numerous scratches and some pit defects from blasting can be observed on images at high magnification. The sandblasted surface represented the basis for all subsequent additional treatments.
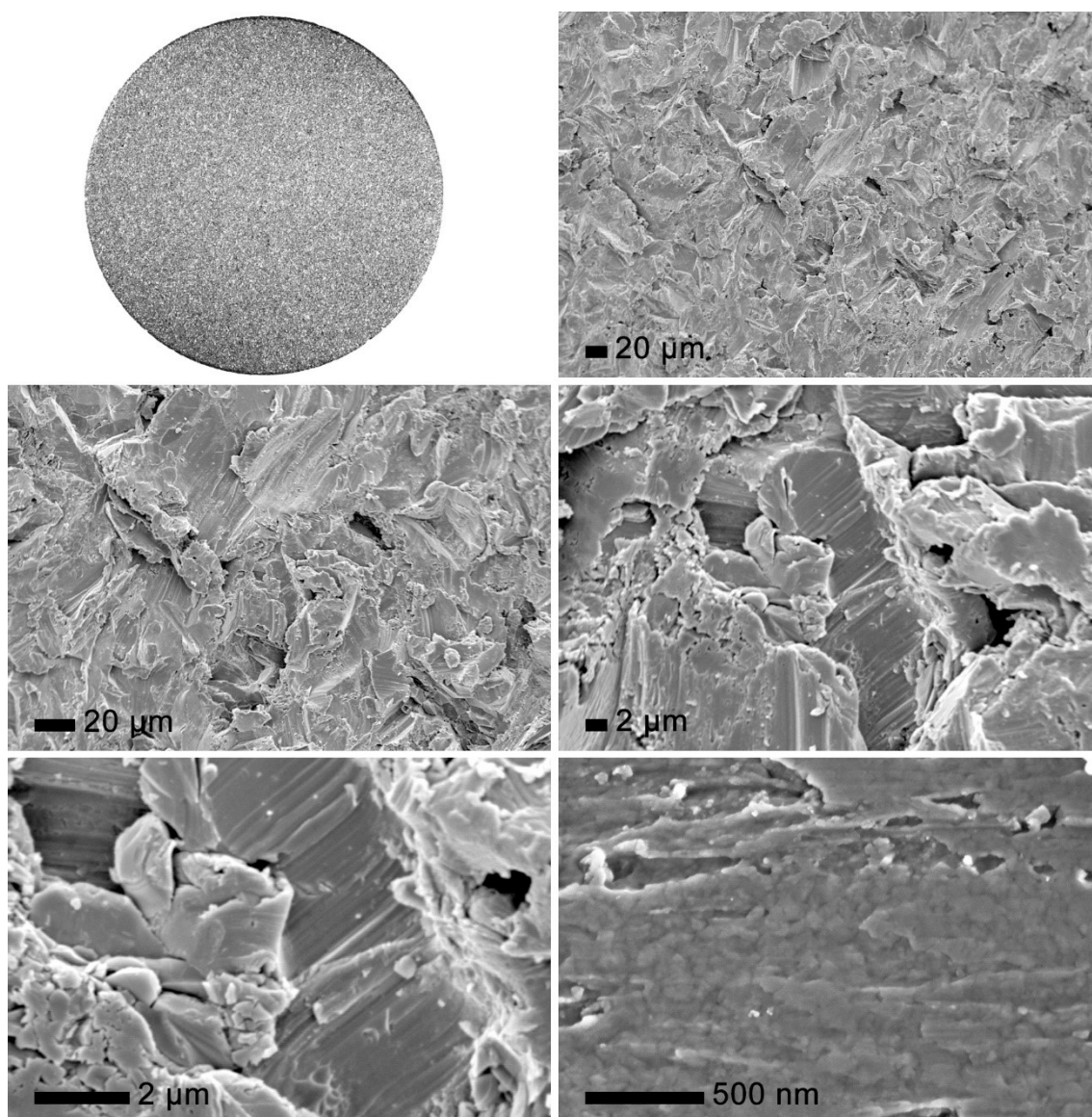
Fig. 3- 1 SEM images of sandblasted surface (reference)

In the S/A group (Fig. 3- 2), the sample surface showed a typical structure after the sandblasting and acid-etching treatment. The acid etching process significantly smoothened the peaks and valleys caused by the sandblasting treatment and generated relative homogeneous ridges and pits with a smaller size. It can be easily identified from the SEM images that the ridges have a lighter color and the pits show as darker regions. These three-dimensional structures formed a wavy surface on both micro- and nano-scales.
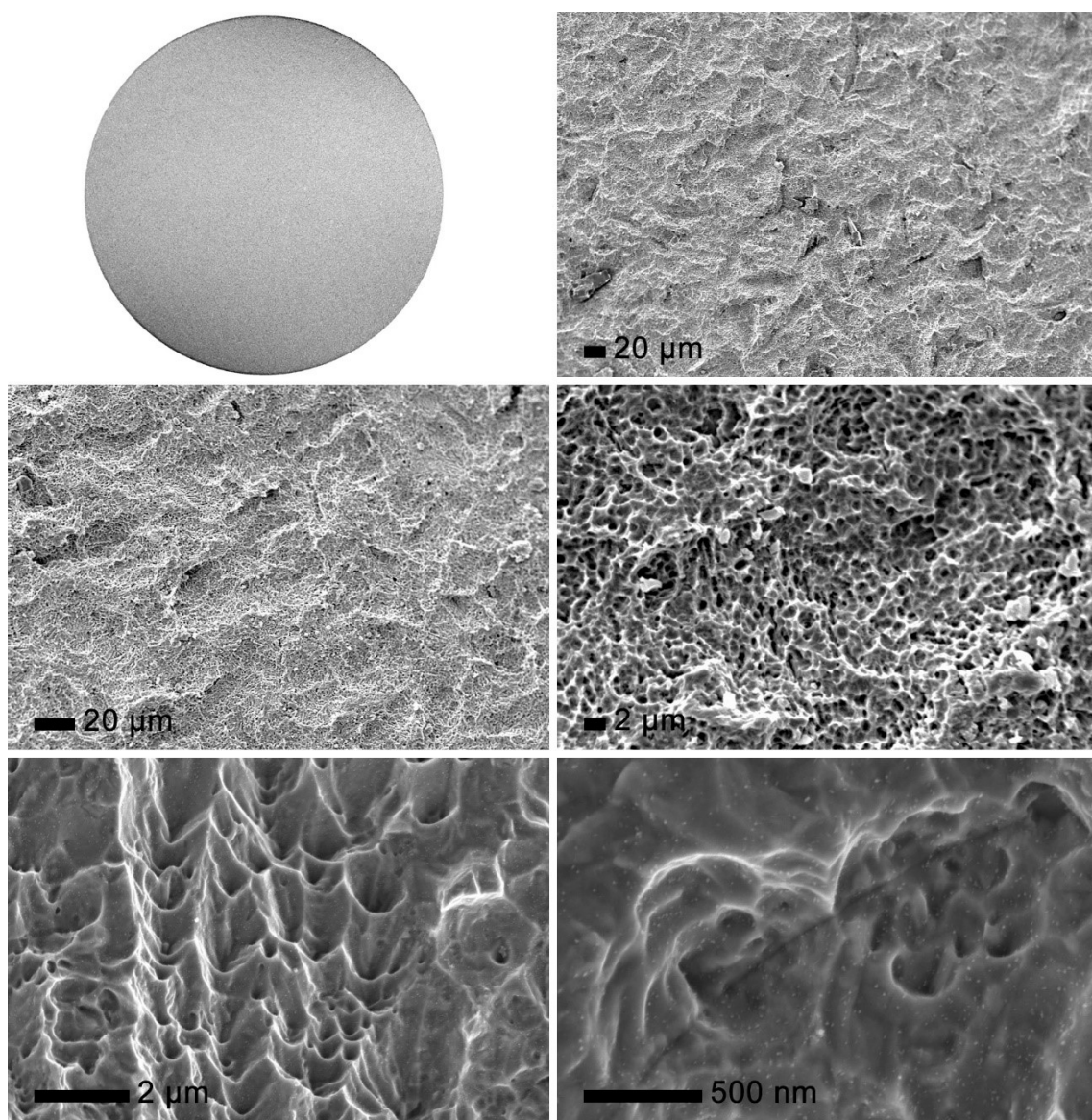
Fig. 3- 2 SEM images of sandblasted and acid-etched surface (reference)

The SPS surface (Fig. 3- 3) showed a cauliflower-like appearance. Since the anatase coating was produced by a plasma jet, the particles from the inner, hot zone of the jet melted, aggregated, and formed the dense part of the coating, while the particles from the outer zone of the jet formed the spherical and smaller agglomerates on top. These combinational structures caused a rougher surface compared with the sandblasted one. Moreover, it can be seen that the SPS process also changed the morphology of the sandblasted surface largely by superimposing the anatase coating on it.
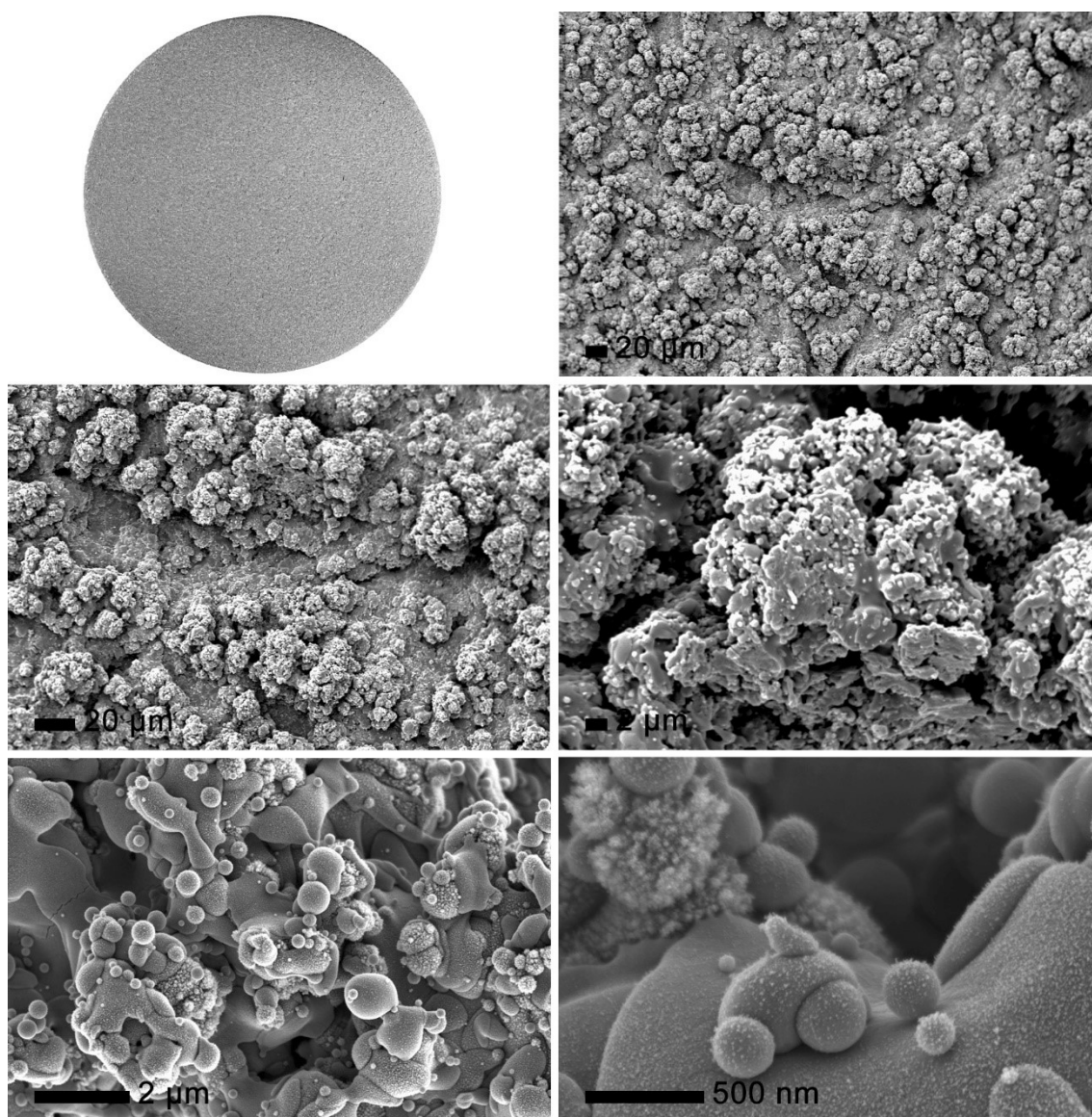
Fig. 3- 3 SEM images of suspension plasma spraying surface (anatase)

The PLC samples (Fig. 3- 4) displayed a cracked-mud-like morphology as a product of coating contraction during the cooling process after heat treatment. The surface consisted of flat and sharp-fractured blocks in a size range of 5-20 µm, which displayed a relatively smooth surface. Additionally, some smaller crystallites were presented in the crevices between the fragments. Besides, we can see from the high magnification image that the surface of the blocks is relatively homogenous on nanoscale. Moreover, the PLC process also changed the morphology of the sandblasted surface a great deal as the SPS process.
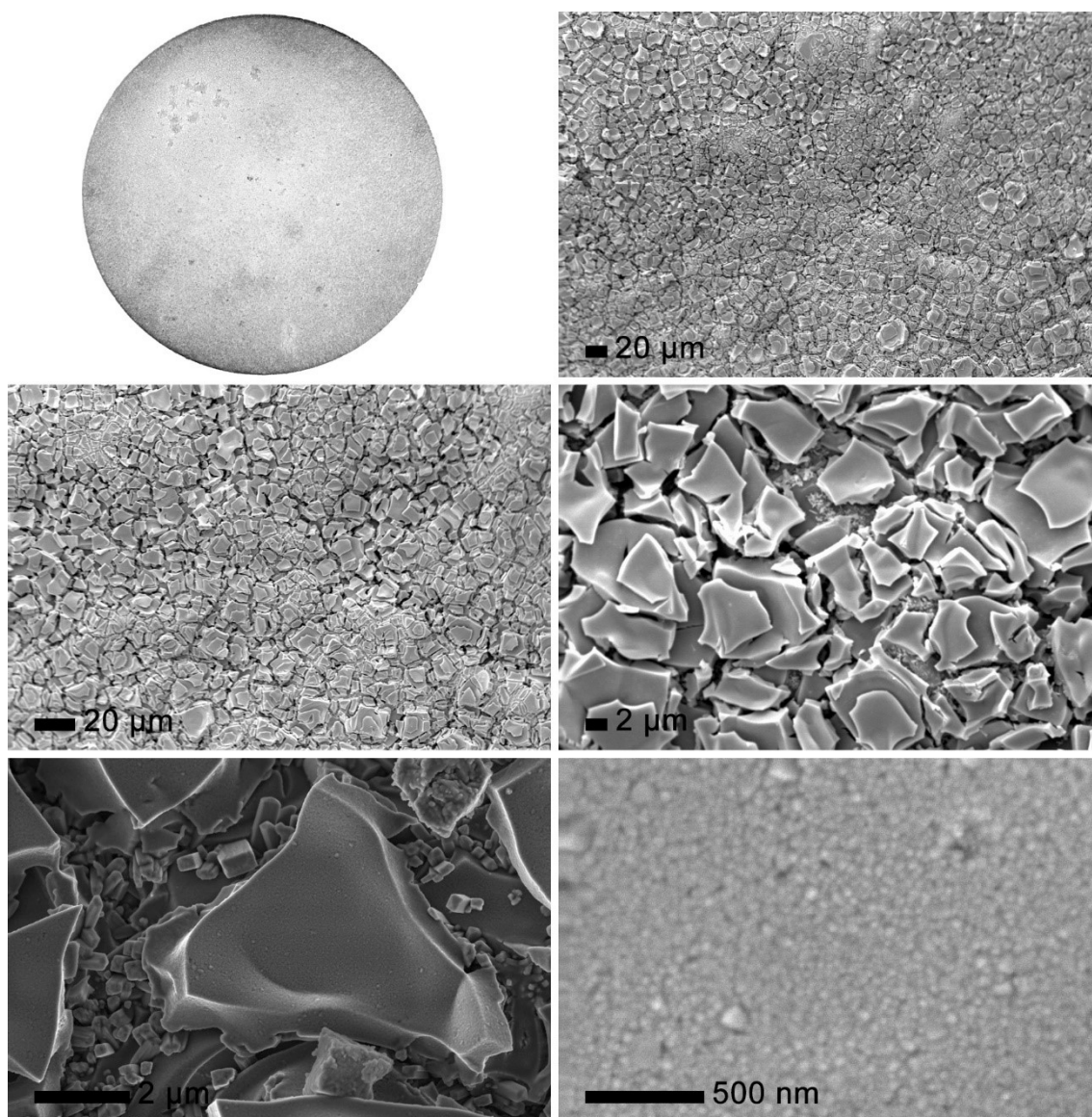
Fig. 3- 4 SEM images of precursor based liquid film coating surface (anatase)

The PVD coating process (Fig. 3- 5) resulted in a thin but dense layer. Thus, it slightly smoothened the sandblasted surface without changing the original microstructure. No significant difference can be observed in the low magnification images compared with the original sandblasted surface. In contrast, a clear difference can be found on the nanoscale between these two groups. On the PVD surface, uniformly distributed spherical particles with a size of 50–150 nm could be recognized. In summary, the above-mentioned results indicated distinct differences in morphology among the investigated surfaces.
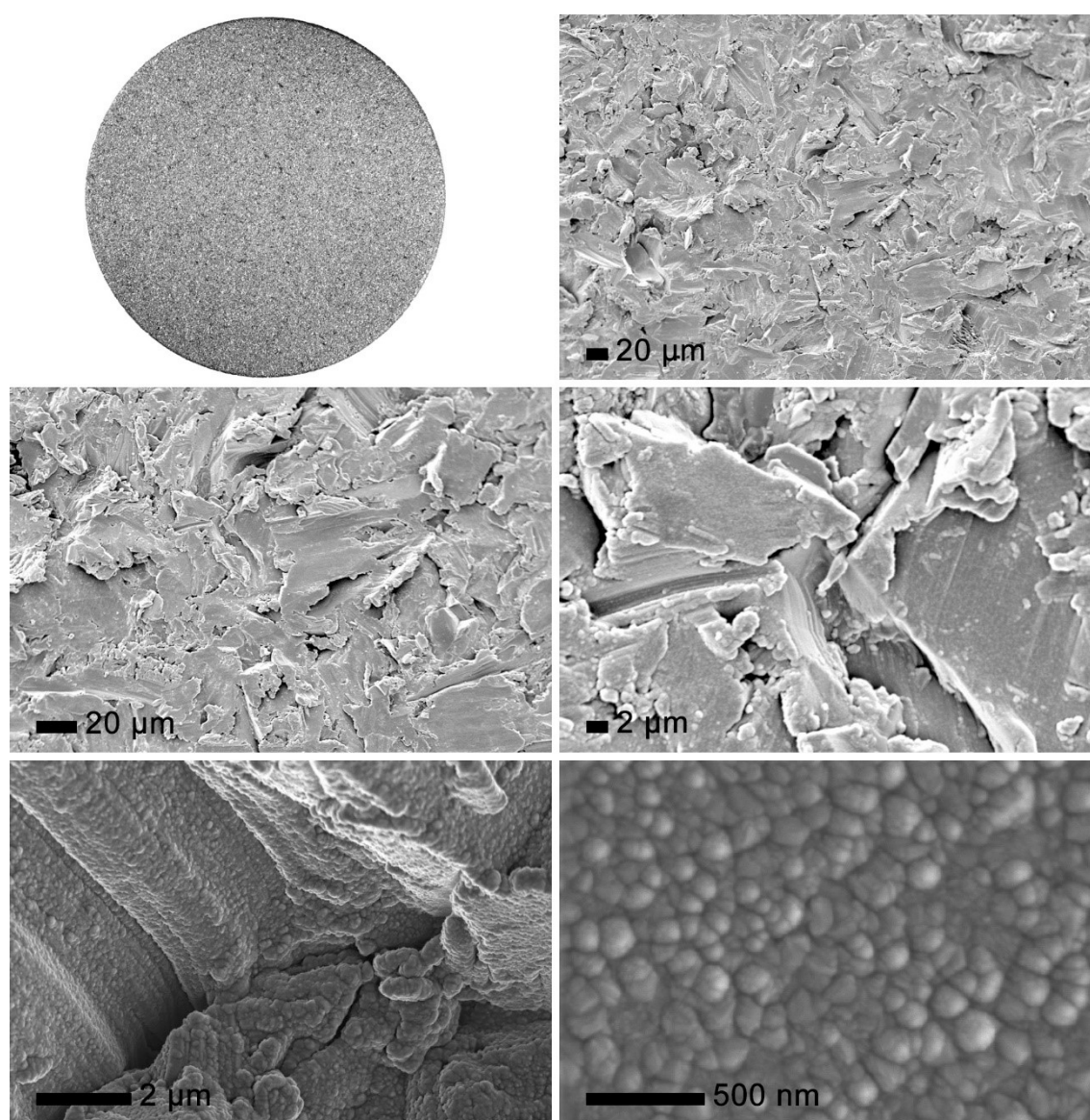
Fig. 3- 5 SEM images of physical vapor deposition surface (anatase)

(2) Surface roughness characterization

1) Two-dimensional roughness characterization

The results of the two-dimensional roughness measurement are shown in Tab. 3- 1. First, the data of the amplitude parameters, Ra, Rz, and Rmax, showed the same tendency for all tested surfaces, resulting in nearly identical patterns in the graphs. In Fig. 3- 6, data for Ra are shown as an example. S/A and PLC surfaces show no significant differences and are relative smooth among all the surfaces. The value of the S surface is also not significantly different from that of the PVD surface, but both of them are higher compared to the values of S/A and PLC surfaces. Moreover, the Ra of the SPS surface is the highest and considerably higher than all the other surfaces.
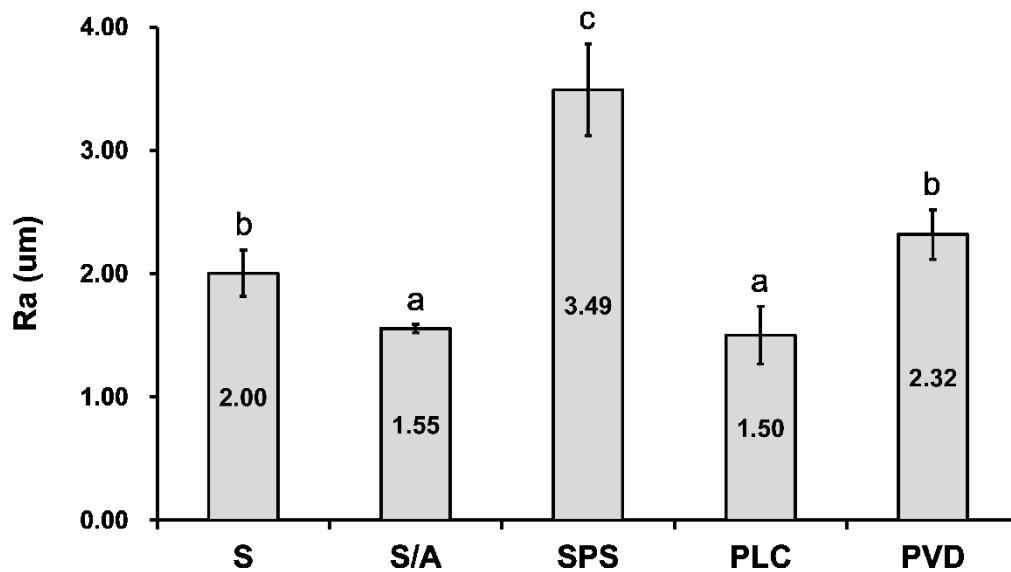
Fig. 3- 6 Amplitude parameter – 2D average roughness ($\bar{x}$ ± s, $p<0.05$, the identical superscripts denote no significant difference.)

Rsk and Rku represented the asymmetry and peakedness of the surface morphology, respectively. For SPS and PLC surfaces, the Rsk values were greater than zero, indicating the predominance of peaks comprising these surfaces. On the contrary, since the Rsk values were smaller than zero, valleys

were, to variable extents, the main structures on the S, S/A, and PVD surfaces. For Rku, the values of S/A and SPS surfaces were about or less than three, suggesting that these surfaces were comparatively moderately structured. Conversely, for the S, PLC, and PVD surfaces with an Rku more than three, extreme high peaks or extreme deep valleys are present on these surfaces.

The Rmr here showed the ratio of the cross sectional length to the evaluation length at the profile section level of one micrometre under the highest peak. Although significant differences existed between the S/A, PLC groups and the S, SPS, and PVD groups, the absolute values of all of them were about 1% and quite small.

Tab. 3- 1 Two-dimensional roughness characterization

Sample / Parameter	S	S/A	SPS	PLC	PVD
R_a (μm)	2.00 ± 0.19 [b]	1.55 ± 0.03 [a]	3.49 ± 0.37 [c]	1.50 ± 0.23 [a]	2.32 ± 0.20 [b]
R_z (μm)	13.94 ± 1.26 [b]	10.31 ± 0.21 [a]	21.43 ± 2.08 [c]	10.67 ± 1.27 [a]	16.14 ± 1.09 [b]
R_{max} (μm)	15.87 ± 1.63 [b]	11.22 ± 0.25 [a]	23.54 ± 2.25 [c]	12.17 ± 1.40 [a]	18.15 ± 1.21 [b]
R_{sk} (/)	-0.06 ± 0.16 [bc]	-0.14 ± 0.05 [b]	0.12 ± 0.09 [c]	0.14 ± 0.09 [c]	-0.36 ± 0.07 [a]
R_{ku} (/)	3.52 ± 0.10 [b]	3.05 ± 0.09 [a]	2.93 ± 0.07 [a]	3.71 ± 0.23 [b]	3.54 ± 0.15 [b]
R_{mr} (%)	0.81 ± 0.12 [a]	1.14 ± 0.04 [b]	0.65 ± 0.02 [a]	0.99 ± 0.14 [b]	0.68 ± 0.02 [a]

Means that have no superscript in common are significantly different from each other (Tukey's HSD, $p < 0.05$).

2) Three-dimensional roughness characterization

The results of the three-dimensional roughness measurement are shown in Tab. 3- 2. The amplitude parameter, Sa (Fig. 3- 7), for the S, S/A, PLC and PVD surfaces varied in magnitude between 1 µm and 2 µm. However, the value of SPS surface, 3.03 µm, was statistically significantly different from all the other surfaces. Besides, the Sa of S and PVD surfaces were also significantly higher than the Sa of the S/A surface. Additionally, the results of another amplitude parameter, Sq, were generally in accordance with the results of Sa, except that only the value of SPS had significant differences with the other groups.
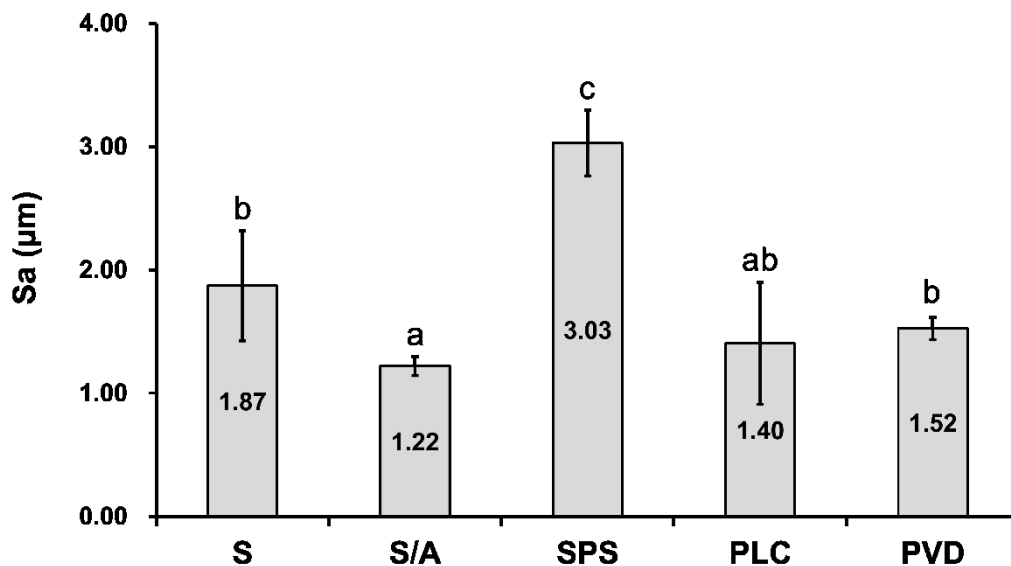

Fig. 3- 7 Amplitude parameter – 3D average roughness ($\bar{x}$ ± s, $p<0.05$, the identical superscripts denote no significant difference.)

Referring to Ssk and Sku, all surfaces, except for SPS, displayed a negative skew and a kurtosis greater than three, indicating that the presence of inordinately deep pits or valleys dominated the morphology of these surfaces, especially the S/A surface. Whereas the values of Ssk and Sku of the SPS surface were 0.09 ± 0.12 and 2.97 ± 0.12, respectively, which demonstrated a moderately varied and normally distributed surface height free of extreme peaks or valleys.

With respect to the spatial parameter, the values of autocorrelation length (Sal) of all experimental surfaces showed only little differences, ranging from 12 mm to 15 mm, except that the Sal of PVD was significantly higher than that of PLC, denoting that the components, which dominated the PVD surface, had relative lower spatial frequency than those on the PLC surface. Besides, since the texture aspect ratios (Str) were all above or very close to 0.5, it was indicated that all surfaces had significant multi-directional uniformity and had no specific texture direction or pattern on the surfaces.

The hybrid parameters, RMS surface slope (Sdq) and developed area ratio (Sdr), are affected by both texture amplitude and spacing so that they may further differentiate surfaces of similar average roughnesses. The results of these parameters showed statistically significant differences among the surfaces. The S/A, PLC and PVD surfaces had significantly lower numerical values for both Sdq (Fig. 3- 8) and Sdr compared with that of the S surface, suggesting that these three surface modification methods decreased the spatial intricacy of the texture after sandblasting in various degree. Moreover, the results of S and SPS surfaces stayed at the same level for these parameters. For consideration of the significantly higher Sa of the SPS surface compared with the S surface, it was indicated that the suspension plasma spraying treatment also decreased the spatial complexity of the sandblasted surface and offered it a wider spaced texture compared with the original finer-spaced features.
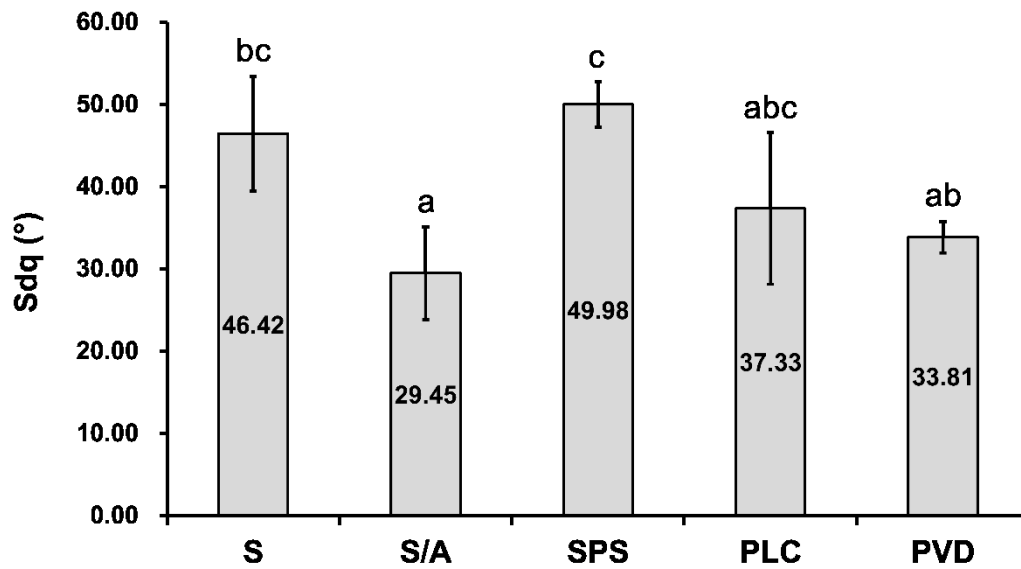
Fig. 3- 8 Hybrid parameter – root mean square surface slope ($\bar{x}$ ± s, *p*<0.05, the identical superscripts denote no significant difference.)

The functional parameters we measured characterize the fluid retention properties of surfaces. The core void volume (Sc) indicates how much fluid would fill the measurement surface from 10% to 80% of surface bearing area, and the valley void volume (Sv) indicates the void volume from 80% to 100% of surface bearing area. According to the bar chart (Fig. 3- 9), the SPS surface was able to retain the maximum volume of fluid in the core area compared with all other surfaces. Meanwhile, the Sc of S and PVD groups were at the intermediate level, and the values of S/A and PLC surfaces were significantly smaller than those of other surfaces. As for Sv, the Sv of SPS and S surfaces were about two times as much as other surfaces. Even so, since the Sv values were almost one order of magnitude lower than those of Sc were, the actual differences of Sv among the experimental surfaces were not as crucial as the differences of Sc, and it can be concluded that the fluid retention of these surfaces is concentrated on the core zone.
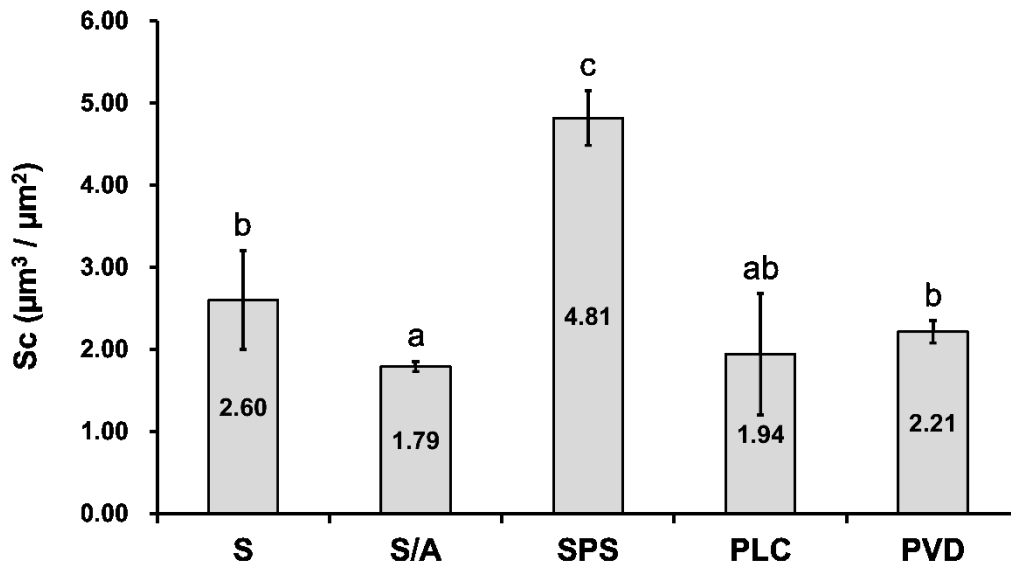
Fig. 3- 9 Functional parameter – core void volume ($\bar{x} \pm s$, *p*<0.05, the identical superscripts denote no significant difference.)

Since the Sa of the experimental surfaces were significantly different from each other, the heights of the core area of these surfaces had also big differences. Thus, rather than analyzing the functional parameters with absolute values, the functional indexes, which were the normalized void volume by Sq, were also interesting for research. For the core fluid retention index (Sci), the value of SPS was still the highest and indicated the greatest fluid retention capacity. However, after normalization, the differences of Sci among the experimental surfaces decreased compared with those of Sc. Besides, the valley fluid retention index (Svi) of SPS even dropped to the smallest one. These indicated that the great fluid retention capability of SPS surface might be mainly attributed to its high average roughness (Sa).

Tab. 3- 2 Three-dimensional roughness characterization

Parameter \ Sample	S	S/A	SPS	PLC	PVD
S_a (µm)	1.87 ± 0.50 [b]	1.22 ± 0.09 [a]	3.03 ± 0.30 [c]	1.40 ± 0.55 [ab]	1.52 ± 0.10 [b]
S_q (µm)	2.60 ± 0.70 [a]	1.70 ± 0.31 [a]	3.79 ± 0.37 [b]	1.85 ± 0.69 [a]	1.99 ± 0.15 [a]
S_{sk} (/)	-0.76 ± 0.53 [a]	-1.41 ± 1.72 [a]	0.09 ± 0.12 [b]	-0.29 ± 0.27 [a]	-0.21 ± 0.10 [a]
S_{ku} (/)	8.71 ± 4.22 [b]	19.74 ± 19.71 [b]	2.97 ± 0.12 [a]	5.38 ± 1.67 [b]	4.28 ± 0.37 [b]
S_{al} (mm)	12.13 ± 0.59 [ab]	14.12 ± 0.99 [ab]	14.24 ± 0.77 [ab]	11.96 ± 1.33 [a]	14.97 ± 2.69 [b]
S_{tr} (/)	0.51 ± 0.19 [a]	0.64 ± 0.13 [a]	0.60 ± 0.13 [a]	0.49 ± 0.11 [a]	0.58 ± 0.15 [a]
S_{dq} (°)	46.42 ± 7.80 [bc]	29.45 ± 6.32 [a]	49.98 ± 3.09 [c]	37.33 ± 0.32 [abc]	33.81 ± 2.13 [ab]
S_{dr} (%)	48.81 ± 23.98 [b]	14.01 ± 5.90 [a]	58.12 ± 10.58 [b]	32.24 ± 29.96 [ab]	19.76 ± 2.80 [a]
S_c (µm^3/ µm^2)	2.60 ± 0.67 [b]	1.79 ± 0.07 [a]	4.81 ± 0.37 [c]	1.94 ± 0.83 [ab]	2.21 ± 0.15 [b]
S_{ci} (/)	1.35 ± 0.10 [a]	1.40 ± 0.16 [a]	1.62 ± 0.05 [b]	1.35 ± 0.08 [a]	1.46 ± 0.03 [ab]
S_v (µm^3/ µm^2)	0.36 ± 0.11 [b]	0.20 ± 0.04 [a]	0.39 ± 0.06 [b]	0.23 ± 0.06 [a]	0.24 ± 0.02 [a]
S_{vi} (/)	0.143 ± 0.003 [c]	0.116 ± 0.008 [ab]	0.102 ± 0.005 [a]	0.131 ± 0.01 [bc]	0.123 ± 0.004 [b]

Means that have no superscript in common are significantly different from each other (Tukey's HSD, $p<0.05$).

(3) Corrosion resistance characterization

The stable and inert oxide film provides titanium with outstanding corrosion resistance in a wide range of aggressive media. However, in this study, anatase coatings, which were manufactured by various coating technologies, displayed different surfaces with diverse porosities, thicknesses, and crystal morphologies. These varied surfaces might influence the corrosion resistance [73]. Therefore, we measured the mass loss of the experimental surfaces after immersion for different periods to clarify if the novel coating procedures compromise the corrosion resistance of the samples.

The line graph below (Fig. 3- 10) shows the absolute mass loss of titanium element during the immersion for one day to 42 days.
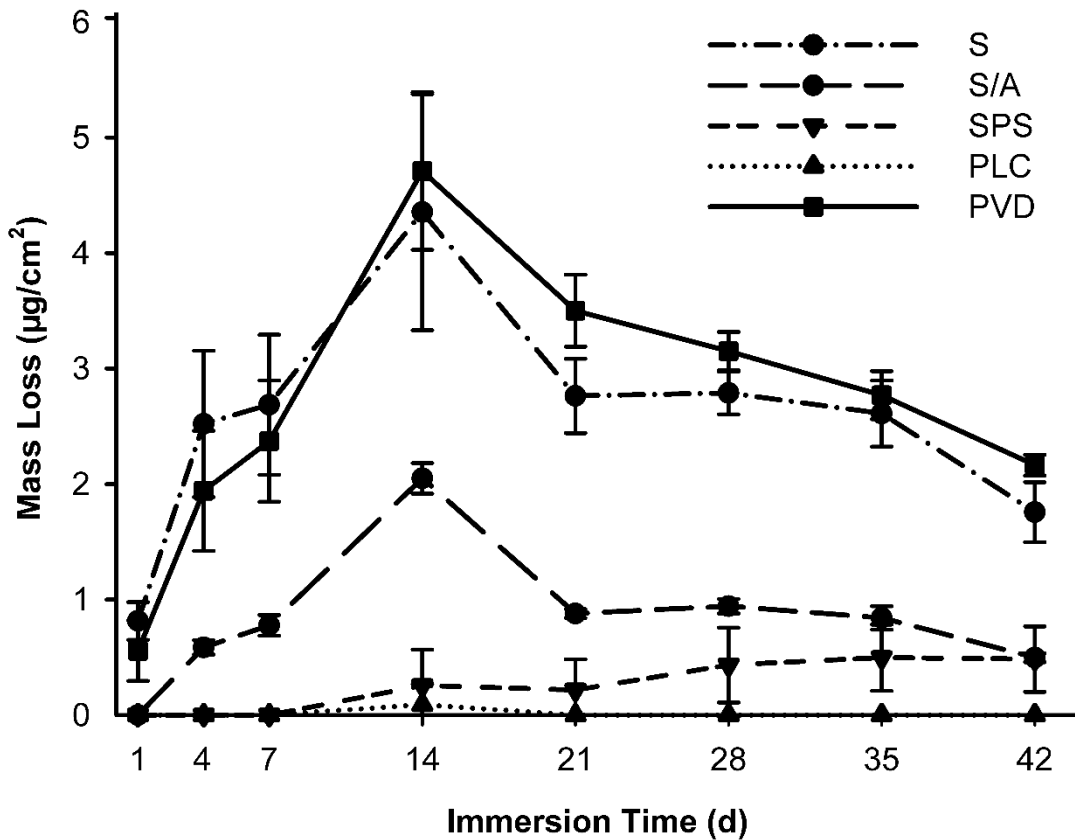
Fig. 3- 10 Absolute mass loss per sq. cm. of titanium element ($\bar{x}$ ± s)

The figure illustrates clearly that the corrosion resistance of anatase coatings differs significantly. The pattern of mass loss of the PVD surface kept pace with that of the S surface. Just from one day after immersion, when there were no mass losses from any other groups, these two surfaces started to release titanium ions. The mass loss of them sharply went up and peaked at more than 4 $\mu g/cm^2$ 14 days after immersion. From then on, their mass loss continuously decreased to about 2 $\mu g/cm^2$ after 42 days after immersion. Similarly, the mass loss of the S/A surface also first increased, reached a peak after 14 days, and then decreased gradually until the end of the incubation period. However, it reached the highest point at only 2.05 ± 0.13 $\mu g/cm^2$. Additionally, the mass loss of the SPS surface kept an upward trend from 7 days after immersion to 0.48 ± 0.28 $\mu g/cm^2$. Last but not the least, there is no mass loss from the PLC surface during the whole immersion except for a minimal amount of 0.09 ± 0.18 $\mu g/cm^2$ at day 14.

Fig. 3- 11 exhibits the cumulative mass loss per square centimeter of titanium element during six weeks immersion. Just like in the previous diagram, the accumulated mass loss from the S and PVD coating increased most to 20.3 ± 2.7 $\mu g/cm^2$ and 21.2 ± 2.4 $\mu g/cm^2$, respectively, after 42 days immersion. The cumulative mass loss of the S/A group retained a moderately increasing rate and rose to 6.6 ± 0.28 $\mu g/cm^2$ eventually. Besides, the SPS and PLC coating both dramatically reduced the accumulated released amount from the original S surface to 1.9 ± 1.34 $\mu g/cm^2$ and 0.1 ± 0.18 $\mu g/cm^2$ respectively.

The data above lead to the conclusion that anatase coatings influence corrosion resistance differently. The thin PVD coating did not affect the corrosion behavior of a typical sandblasted implant surface significantly. On the contrary, anatase coatings manufactured by SPS and PLC increased the corrosion stability of S
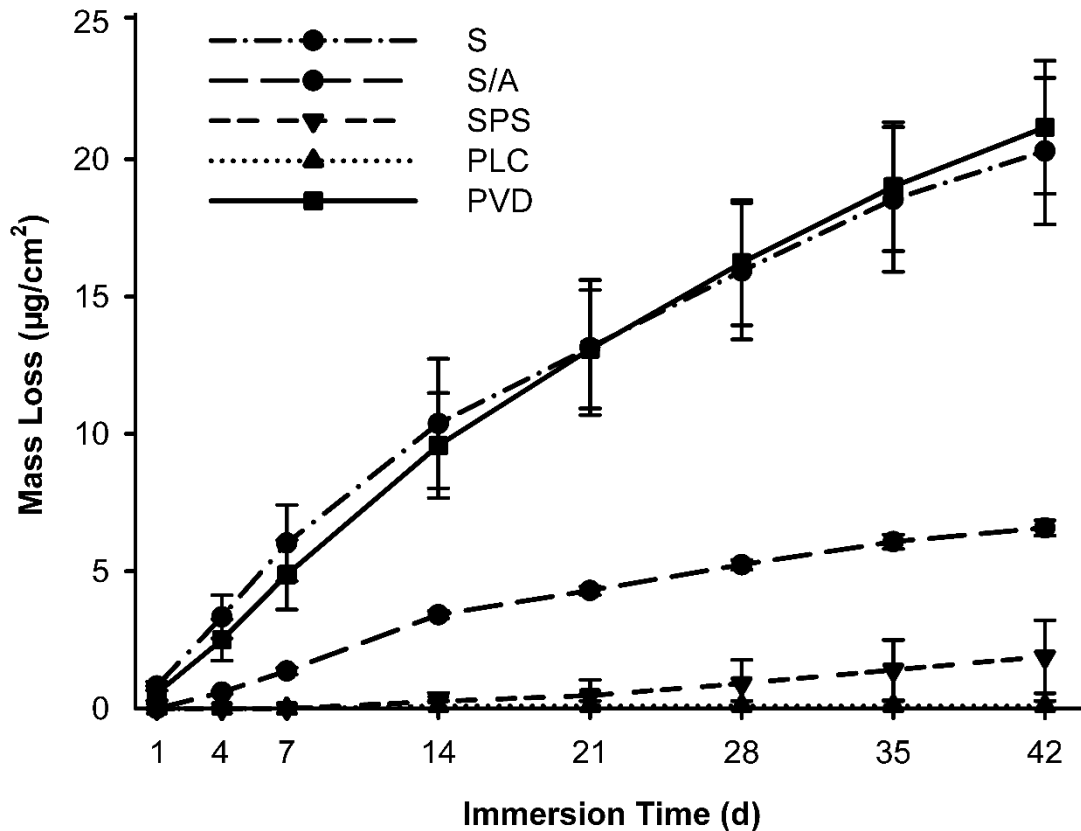
Fig. 3- 11 Cumulative mass loss per sq. cm. of titanium element ($\bar{x}$ ± s)

surface effectively and even showed superior corrosion resistance compared to the commercially used, sandblasted and acid-etched surface. Moreover, these results also demonstrate that the corrosion resistance, which acts as an important influence on the long term success of osseointegration, is not compromised by any of these surface modifications. The accumulated ion release amounts of titanium element from all experimental surfaces are acceptable according to EN ISO 22674.

Furthermore, from the SEM images (Fig. 3- 12) of the experimental surfaces at 5000 x magnification before and after six weeks-immersion, no visible sign of corrosion or overall uniform attack can be seen on specimens as well. It is necessary to note here that all SEM photos were taken at different locations so

that an exact side-by-side comparison cannot be done. Even so, all of these are

exemplary images that give a general picture of the surfaces.
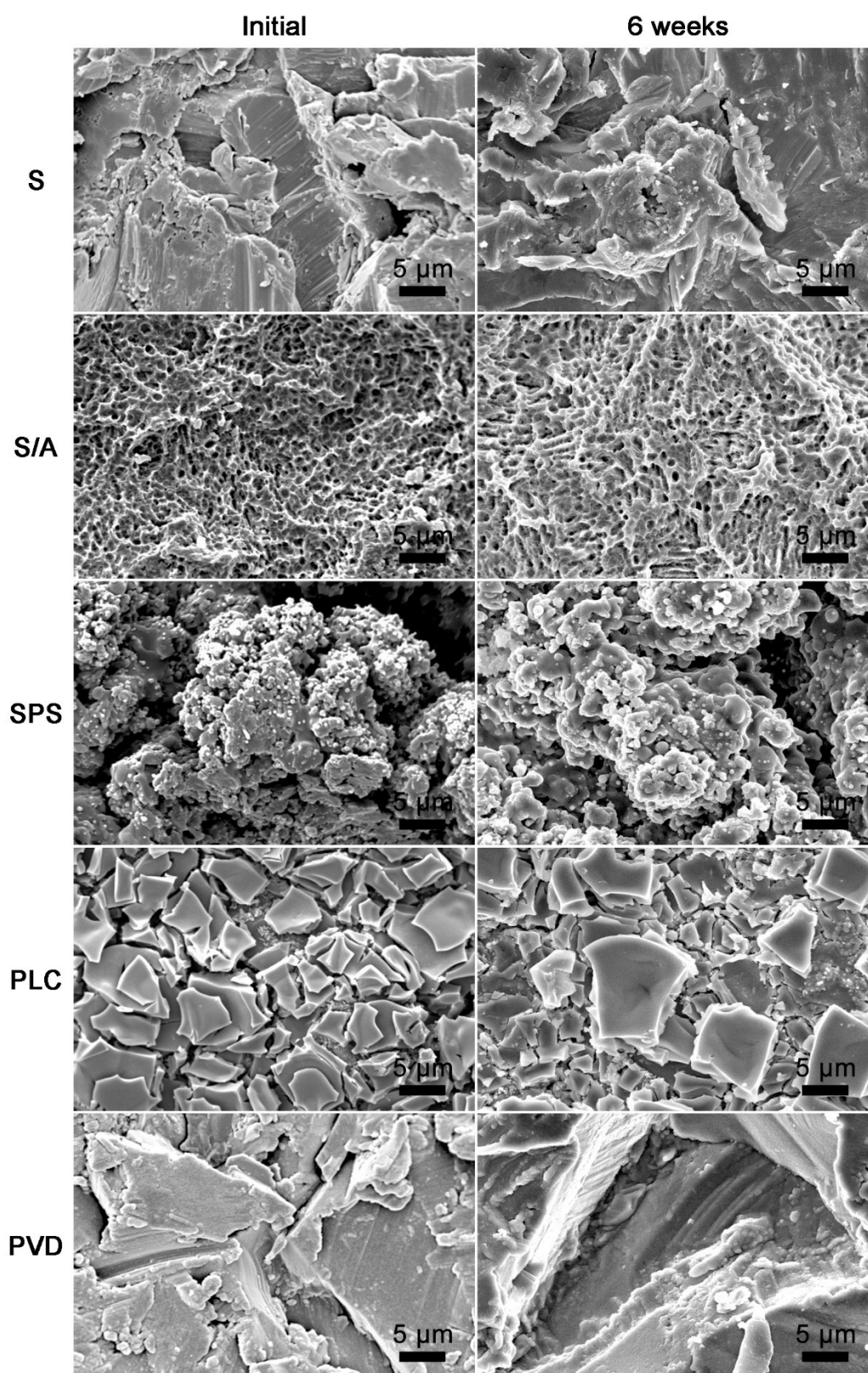
Fig. 3- 12 Exemplary SEM images before and after 6 weeks-immersion

(4) Contact angle analysis

The improvement of hydrophilicity is a significant phenomenon during the photocatalytic activation by anatase. This phenomenon is quantitatively represented by the reduction of contact angles. Thus, in this study, contact angle was used as an indicative parameter that showed the degree of photocatalysis as a function of UVA irradiation. After three and six weeks of aging (storage in the dark), the static contact angles between water and the experimental surfaces were measured before and after different periods of UVA irradiation.

Fig. 3- 13 describes the changes of the contact angles on the experimental surfaces over irradiation time after three weeks storage. According to the line chart, the contact angles on PVD and PLC samples showed a significant decline after UVA treatment. The initial contact angle was 50 ± 1.4° for the PVD group and 37 ± 5.0° for the PLC group. In the PVD group, the value of contact angle decreased drastically, e.g. from 50° to about 19° in the first 30 seconds of irradiation, and dropped to 0° at a moderate rate in the end. Meanwhile, the contact angle in the PLC group declined more smoothly and reached its lowest value with 22 ± 3.1° after 600 seconds irradiation. However, unlike the previous two groups, there was no significant difference before and after UVA-exposure in the other three groups. The SPS surface, surprisingly, exhibited a contact angle of 0° before irradiation. Therefore, no further time-dependent decrease of contact angle caused by photocatalysis could be observed. Besides, the contact angles in the S group and S/A group also remained at almost the same level from about 102° to 95°. Additionally, Fig. 3- 14 illustrates the water drops on the corresponding surfaces before and after 600 seconds irradiation. These photos further vividly visualized different changes of drop shape on the various experimental surfaces before and after irradiation.
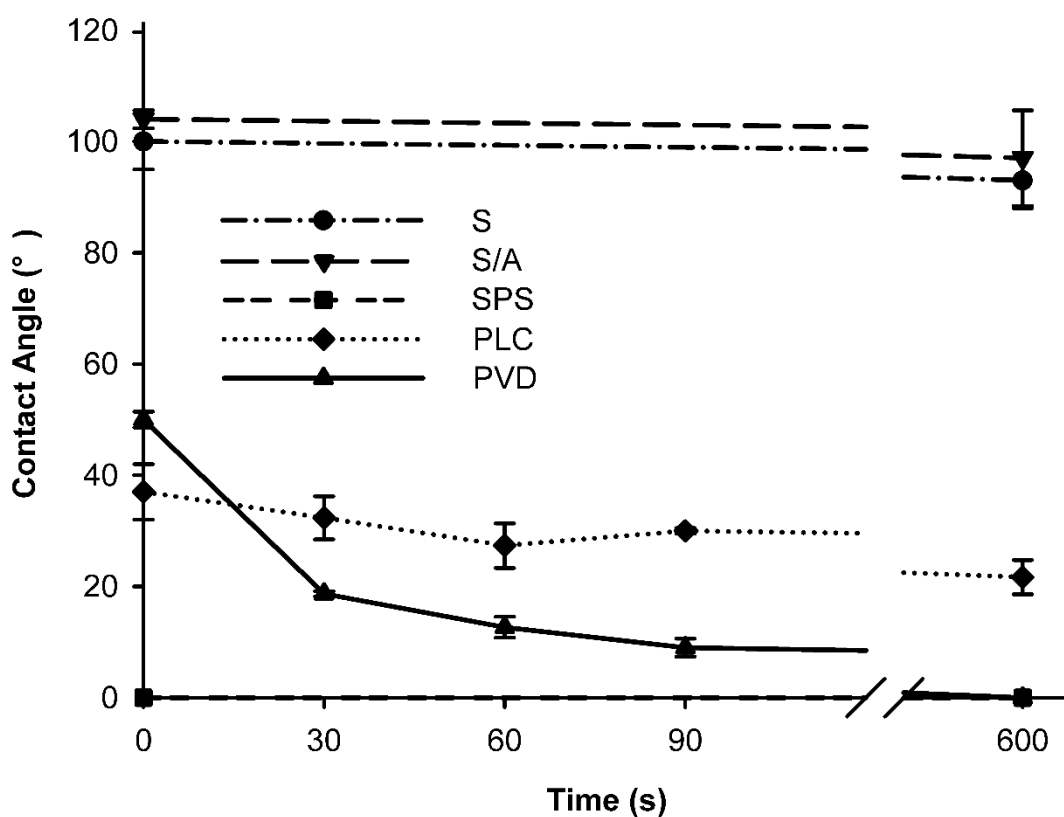
Fig. 3- 13 Contact angle changes over irradiation time (after 3w storage)
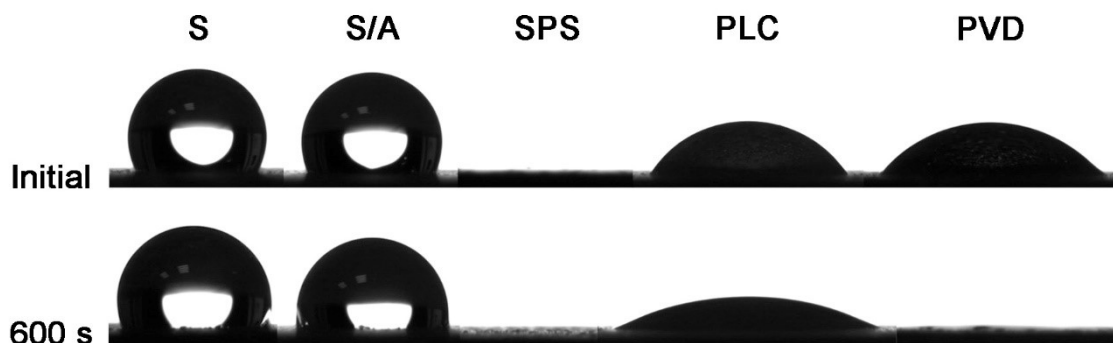
Fig. 3- 14 Drop shape change before and after irradiation (after 3w storage)

The trends of contact angles' changes after six weeks storage (Fig. 3- 15) were similar to those after three weeks. The relative larger initial contact angles may be caused by the longer period of storage that resulted in higher amount of contamination.
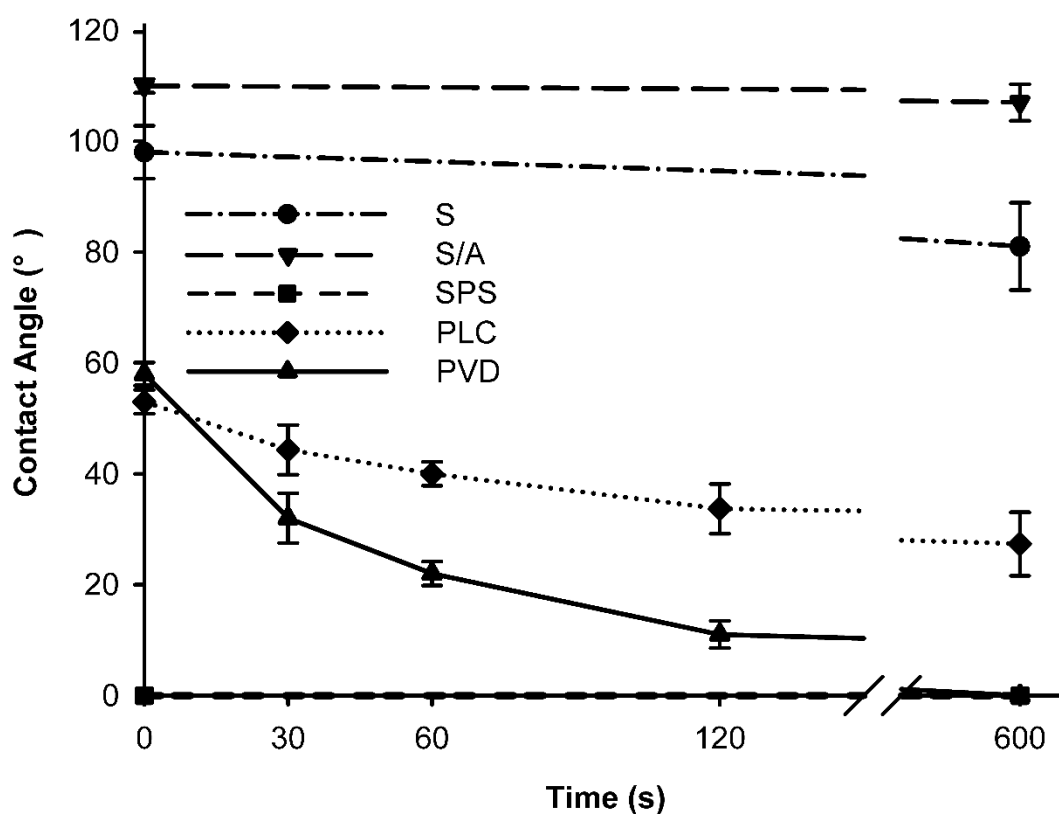
Fig. 3- 15 Contact angle changes over irradiation time (after 6w storage)

In conclusion, the figures above indicate that the photocatalysis rate of the PVD surface is higher than that of PLC surface. The S and S/A surfaces, which were without anatase coating, exhibited complete absence of anatase-mediated, photoinduced hydrophilization and remained hydrophobic all along. However, this method could not be used to evaluate the photocatalysis activity of the SPS surface since its contact angle remained at 0° from beginning to the end.

(5) Photocatalytic degradation of methylene blue

To quantify the photocatalysis activity of different anatase modifications further, especially of the SPS surface that could not be evaluated by contact angle analysis, photocatalytic degradation of methylene blue (MB) was investigated. The decreases in MB concentration as a function of UVA-irradiation time of the experimental surfaces were monitored photometrically in tissue culture well plates. Wells without titanium samples (tissue culture polystyrene, TCPS) were used as additional controls for direct photodecomposition of MB by UVA light.

Tab. 3- 3 shows the optical density of MB after different irradiation times of the tested surfaces and the statistical differences among the data that was measured at the same time point. Fig. 3- 16 further depicts these changes of optical density vividly.

Tab. 3- 3 Optical density of MB after various irradiation time ($\bar{x} \pm s$, O.D.$_{620}$)

	S	SPS	PLC	PVD	TCPS
0 min	0.38 ± 0.00^a	0.38 ± 0.00^a	0.38 ± 0.00^a	0.38 ± 0.00^a	0.38 ± 0.00^a
10 min	0.37 ± 0.01^a	0.32 ± 0.02^b	0.37 ± 0.01^a	0.36 ± 0.02^a	0.38 ± 0.00^a
20 min	0.36 ± 0.01^a	0.22 ± 0.02^c	0.35 ± 0.01^{ab}	0.32 ± 0.02^b	0.37 ± 0.02^a
30 min	0.34 ± 0.01^a	0.14 ± 0.02^c	0.32 ± 0.01^a	0.28 ± 0.03^b	0.34 ± 0.00^a

Data without the same superscript are significantly different from each other (Bonferroni, $p<0.05$).

From the table above, we can clearly see that the S surface exhibits a very low rate of MB degradation, which is comparable to the rate observed in the TCPS group. This indicates that the MB degradation on S surface can be solely attributed to the direct photodecomposition by UVA irradiation. On the SPS and
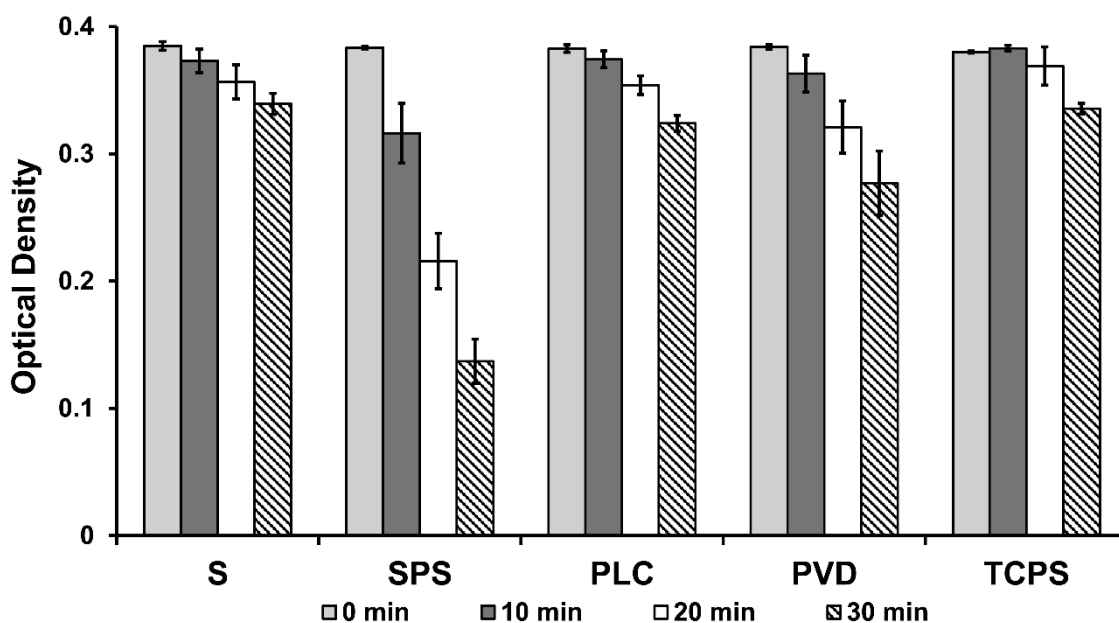
Fig. 3- 16 Optical density of MB after different irradiation time ($\bar{x} \pm s$)

PVD surfaces with anatase coatings, MB molecules were decomposed faster and ultimately reduced to 35.7% and 72.1% of their initial concentrations, respectively. This indicated that these anatase modifications showed effective photocatalytic activity, especially the SPS surface that significantly reduced the MB concentration compared to all other surfaces already after irradiation for ten minutes. However, the photocatalytic activity of the third anatase coating, the PLC surface, was comparative lower. Although the concentration of MB in the PLC group was decomposed to 84.6% of its initial value, this was comparable to the values of the S surface (88.2%) and the TCPS group (88.3%), indicating that this decomposition was solely caused by direct photolysis.

Researchers have found that the photocatalytic-oxidation reaction rates of most organic dyes could be expressed through the Langmuir-Hinshelwood (L-H) model [74, 75]. Xu et al. also indicated that the photodegradation of MB followed the first-order reaction law [76]. Therefore, simple linear regressions (Fig. 3- 17) were performed between the irradiation time and the natural logarithm of the ratio
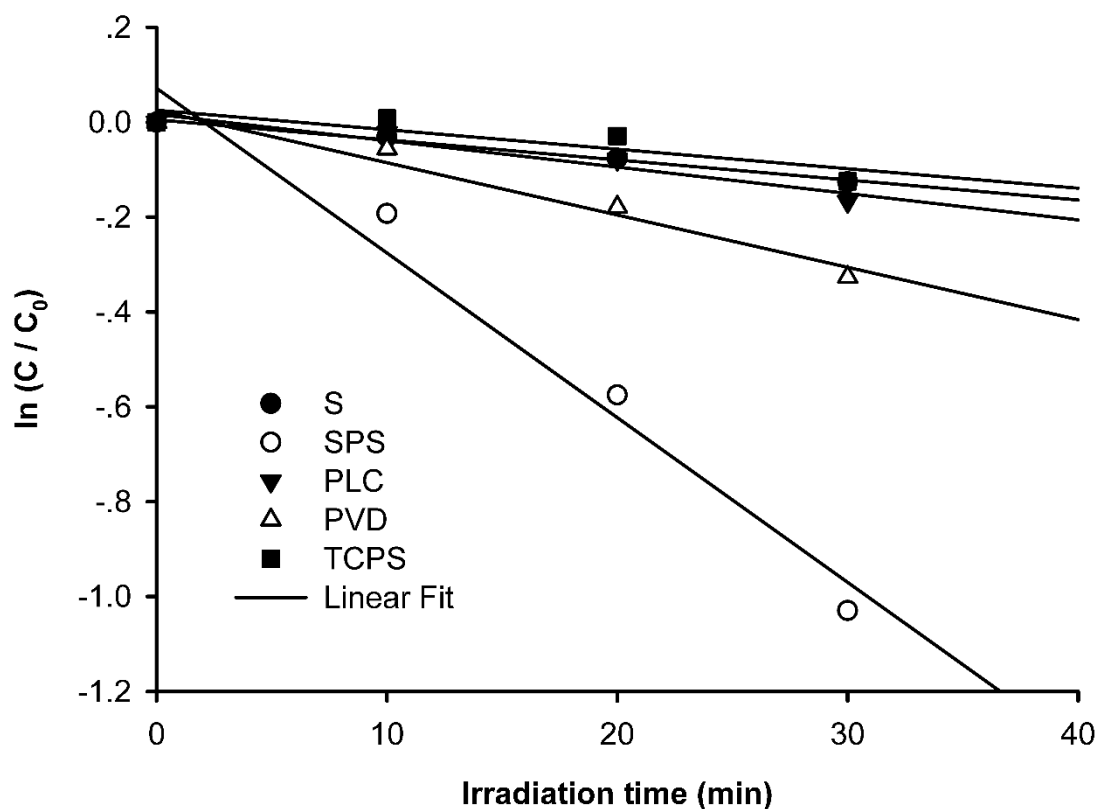
Fig. 3- 17 Photocatalytic degradation kinetic behavior of methylene blue

between the final concentration and the initial one. The linear plot above verifies that the photocatalytic degradation of MB in this study followed a pseudo-first order reaction kinetics as well. Thereby the rate equation of MB degradation reaction can be presented as follows:

$\ln (A_0/A) = \ln (C_0/C) = kt$

in which A_0 is the initial MB absorbance, A is the absorbance after treatment for time t. C_0 and C are the corresponding concentrations respectively. Then the first-order rate constant k can be calculated from the regression of experimental data.

A comparison of the calculated photocatalytic rate constant k of the experimental surfaces is presented in Fig. 3- 18. The results manifested that this experiment successfully quantified the photocatalysis activity of the SPS surface. The rate
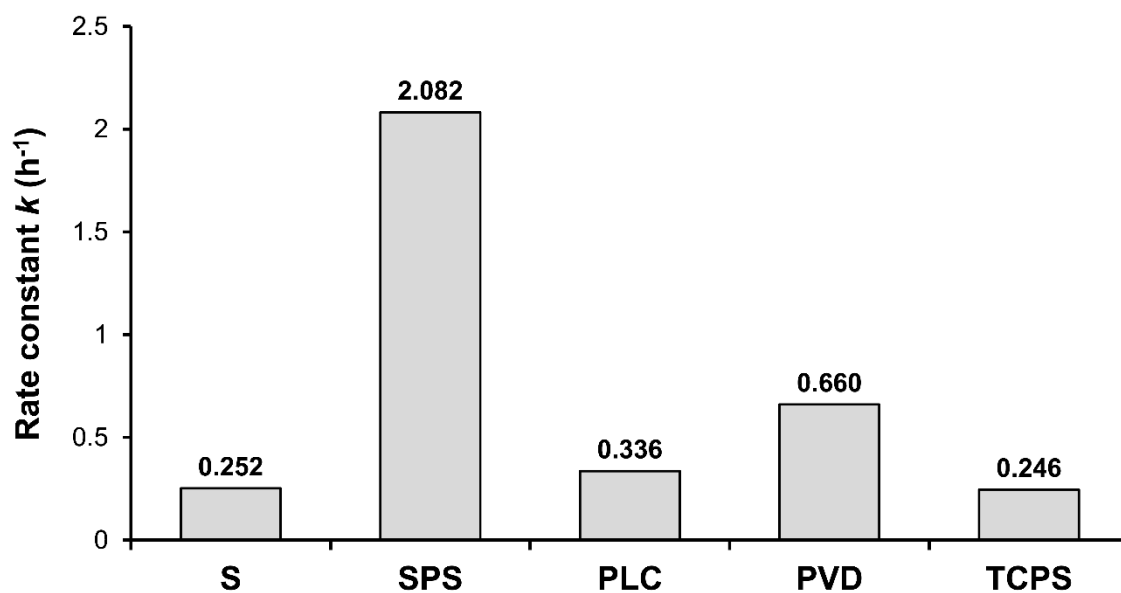
Fig. 3- 18 Calculated photocatalytic rate constant *k* of experimental surfaces

constant of SPS was 2.082/h, which was more than eight times larger than that of the original sandblasted surface. Actually, at the end of experiments, the MB solution in the SPS group was nearly complete-decolorized, indicating an almost complete degradation of MB. Furthermore, other results here coincide with those of contact angle analysis. The rate constant of the PVD surface was larger compared with the PLC surface, and the rate constant of the S surface showed no difference with that of the negative control, TCPS.

3.2 Biological analyses

(1) Proliferative activity of osteoblasts

To determine the effects of both surface modifications and UVA irradiation on the proliferation of human osteoblasts, we used the XTT colorimetric assay to estimate the number of metabolically active cells. Fig. 3- 19 shows the original data, the mean optical density, of the cells on each kind of experimental surface after 1, 2, 3, and 4 days culture in the first experiment as an example. As can be seen from the figure, in all groups the metabolic activity continuously increases over the 4 days culturing time, indicating that the osteoblasts on all surfaces keep proliferating and maintain a proper state. Except for Fig. 3- 19, other figures in this results section are all calculated means, derived from three replications of the XTT assay. In order to be able to combine data from different experiments, they were normalized to S as internal reference. For each experiment, the mean value of the S samples at each respective time point was set to 1.0, and all other data were related to this value. The data thus are given as normalized fold change in XTT absorbance in relation to the value of the S surface, because the original data in different replications cannot be directly averaged and compared.
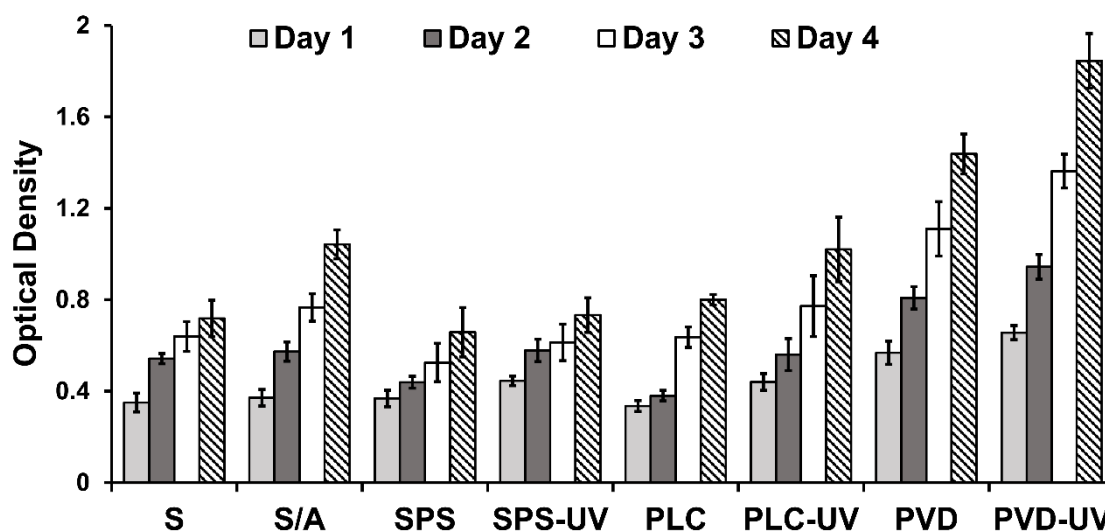
Fig. 3- 19 Exemplary absolute values of optical density in XTT assay ($\bar{x} \pm s$)

1) Influence of surface composition and structure

Above all, Fig. 3- 20 describes the comparison of cellular proliferation among the experimental surfaces without UVA irradiation. From the figure, we can clearly see that the two referential surfaces have no significant differences in XTT absorbance throughout the experiment. Moreover, the proliferation rate of osteoblasts cultivated on the PVD surfaces persistently remained significantly faster than those of all other surfaces are. After 4 days culture, the metabolic activity was more than 1.6 times higher compared to the sandblasted reference. For SPS and PLC, although the figure shows relatively low values of both of them in day 2, 3, and 4, the statistical analysis demonstrated that only the values of the PLC surface in the last three days were statistically smaller than those of the S and S/A were. From the results above, we can conclude that the anatase coating manufactured by PVD significantly stimulates the proliferation of osteoblasts compared to all other surfaces, while the PLC surface decreases the proliferation rate of cells.
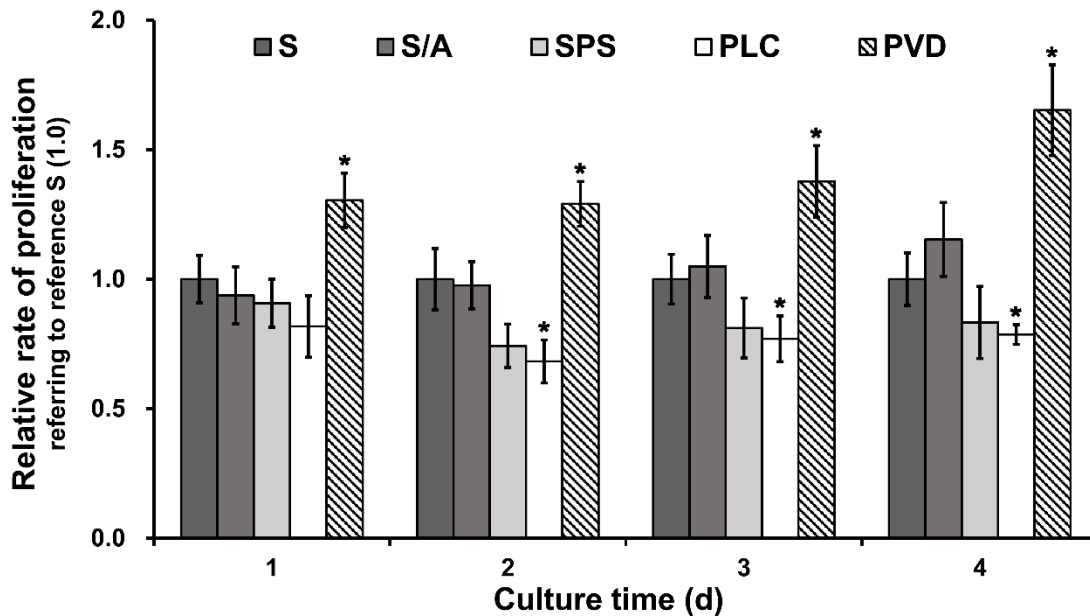
Fig. 3- 20 Relative proliferative activity (XTT absorbance) of SAOS-2 osteoblasts cultivated on different non-irradiated surfaces. For each time point, the mean absolute absorbance value of the reference S was set to 1.0 and the relative activity in relation to this value was calculated for the other surfaces. (* = statistically significant difference to S surface, $p<0.05$)

2) Influence of UVA irradiation

Then, Fig. 3- 21, Fig. 3- 22, and Fig. 3- 23 respectively present the differences of XTT absorbance in the SPS, PLC, and PVD groups with and without UVA irradiation. According to the figures, the proliferation rates of the UVA-treated surfaces in all three anatase groups are significantly higher compared to the corresponding untreated ones at all time points. This indicates a photocatalytic "biological activation" of these surfaces, which results in an improvement of cellular proliferation. These results were consistent with our previous finding [77]. Besides, unlike the metabolic activity of the SPS surface that remained steady, the metabolic activity of the PVD surface rose over time, whether the surface was irradiated or not. For example, in the 3rd day, the proliferation rate of the irradiated PVD surface was already significantly larger than those in day 1 and 2 were, and the value in day 4 even had statistically significant differences with those of the previous three days. While the proliferation rate of the PLC surface only started to increase after UVA irradiation.
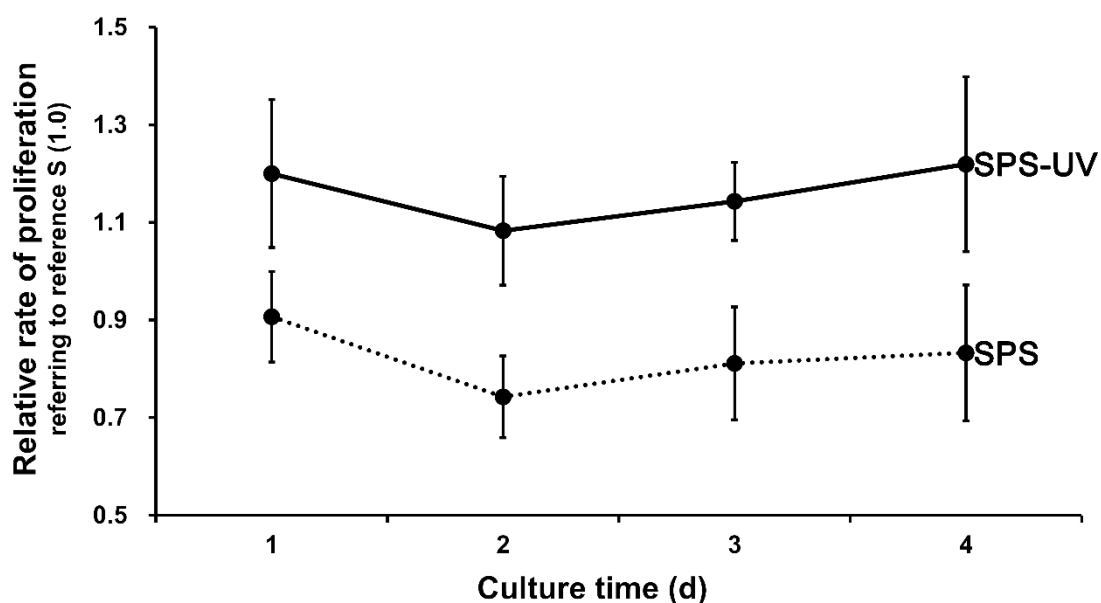
Fig. 3- 21 Relative proliferative activity (XTT absorbance) of SAOS-2 osteoblasts cultivated on SPS surface with and without UVA irradiation. The relative activity of SPS groups was derived from dividing the mean absolute absorbance values of SPS groups by that of the reference S at each time point.

67
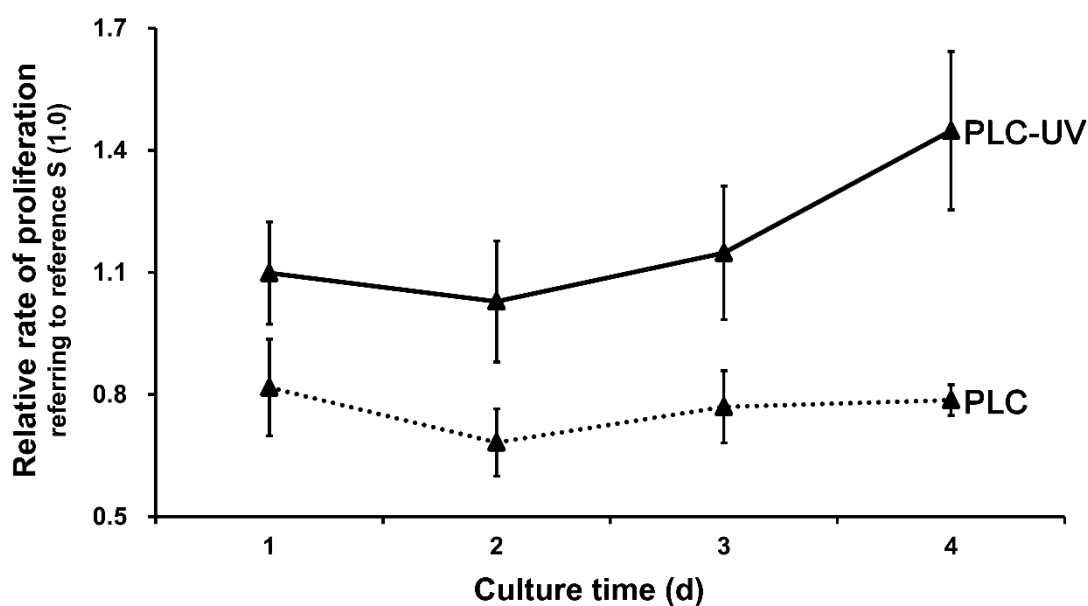
Fig. 3- 22 Relative proliferative activity (XTT absorbance) of SAOS-2 osteoblasts cultivated on PLC surface with and without UVA irradiation. The relative activity of PLC groups was derived from dividing the mean absolute absorbance values of PLC groups by that of the reference S at each time point.
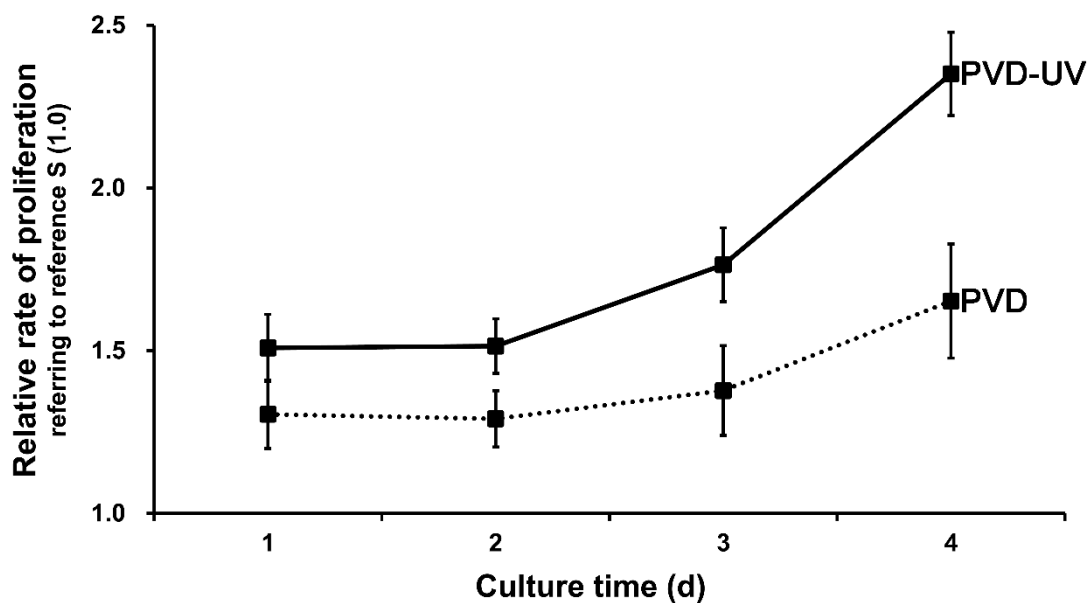
Fig. 3- 23 Relative proliferative activity (XTT absorbance) of SAOS-2 osteoblasts cultivated on PVD surface with and without UVA irradiation. The relative activity of PVD groups was derived from dividing the mean absolute absorbance values of PVD groups by that of the reference S at each time point.

Additionally, Fig. 3- 24 depicts the relative proliferation rates of all anatase surfaces with and without UVA irradiation. As is demonstrated in the figure, even without UVA treatment, the PVD surface already shows a proliferation rate at a slightly higher level than the irradiated SPS and PLC surfaces. Besides, as mentioned before, the UVA irradiation further improved the proliferation of osteoblasts significantly on the PVD surface. Thus, from day 2 on, the proliferation on the irradiated PVD surface was significantly more pronounced than the irradiated SPS and PLC surfaces. Actually, this photocatalytic "biological activating" effect of irradiation was most prominent in the PVD group in comparison to the other two anatase surfaces. Meanwhile, the proliferation rates of the SPS and PLC surfaces kept similar with each other under both the irradiated and the non-irradiated conditions.
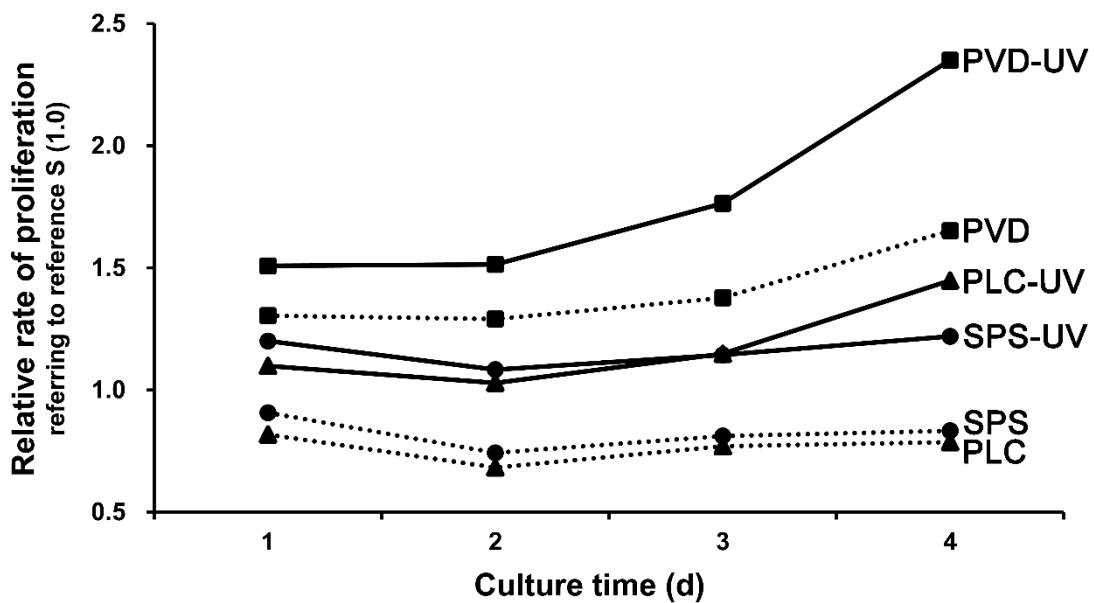

Fig. 3- 24 Relative proliferative activity (XTT absorbance) of SAOS-2 osteoblasts cultivated on all anatase surfaces with and without UVA irradiation. The relative activity of different groups was derived from dividing the mean absolute absorbance values of different groups by that of the reference S at each time point.

At last, Fig. 3- 25 compares the proliferation rates between the irradiated anatase surfaces and the references. In comparison with the non-irradiated surfaces in Fig. 3- 20 where the proliferation on the SPS and PLC surfaces was lower than on the S and S/A samples, the proliferation rates of the irradiated SPS and PLC surfaces here achieved about the same level as the references. At day 4, the metabolic activity of the PLC group was even significantly higher than that of the sandblasted reference. Moreover, the proliferative activity of the irradiated PVD surface consistently was the highest among all surfaces, achieving approximately 2.4 times enhancement compared to the sandblasted reference at day 4. Therefore, it can be concluded that, i: none of the photo-activated anatase coatings compromised the proliferative activity of osteoblasts in comparison with the original S surface, and ii: that the irradiated PVD coating even doubled the osteoblast population compared with the most commonly used S/A surface.
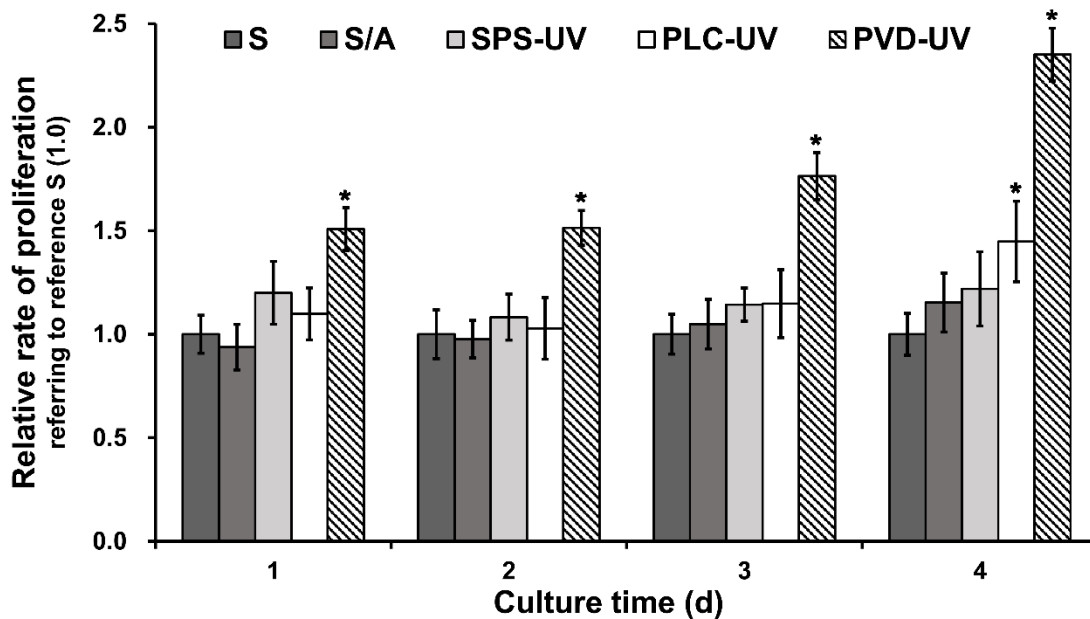

Fig. 3- 25 Relative proliferative activity (XTT absorbance) of SAOS-2 osteoblasts cultivated on irradiated anatase surfaces and reference surfaces. For each time point, the mean absolute absorbance value of the reference S was set to 1.0 and the relative activity in relation to this value was calculated for the other surfaces. (* = statistically significant difference to S surface, $p < 0.05$)

(2) Surface coverage analysis

To gain a more intuitive proof of the influence on the osteoblast proliferation by the surface modifications and the UVA irradiation, we then stained the cells on the samples with crystal violet to determine the osteoblast coverage of the experimental surfaces after the four-day culture. Fig. 3- 26, Fig. 3- 27, Fig. 3- 28, and Fig. 3- 29 illustrate the results of the crystal violet staining of all tested groups. For each group, an exemplary picture of the whole sample and another one in high magnification are presented.

The results of the staining coincided well with the results of XTT test. Through the macroscopic observation of the pictures, we can clearly see that the osteoblast-covered areas of all UVA-treated anatase surfaces are significantly larger than those in the corresponding untreated surfaces are. Moreover, except for the PVD surface, the cellular coverages in all the other untreated anatase surfaces appeared to have no obvious difference compared with the S and the S/A references. On contrast, on all irradiated anatase surfaces, the stained osteoblasts covered more area than on the references. Among them, the osteoblasts on the irradiated PVD surface still showed the highest surface coverage.
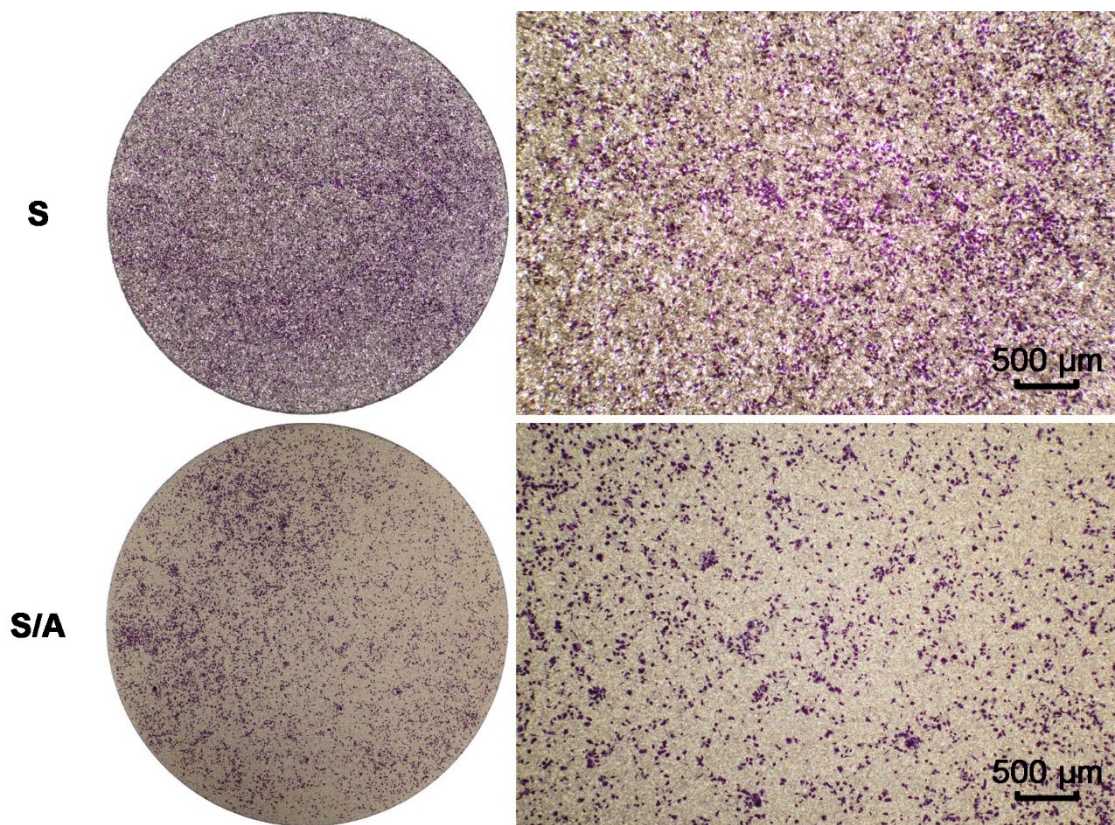
Fig. 3- 26 Crystal violet staining of S and S/A surfaces as the references
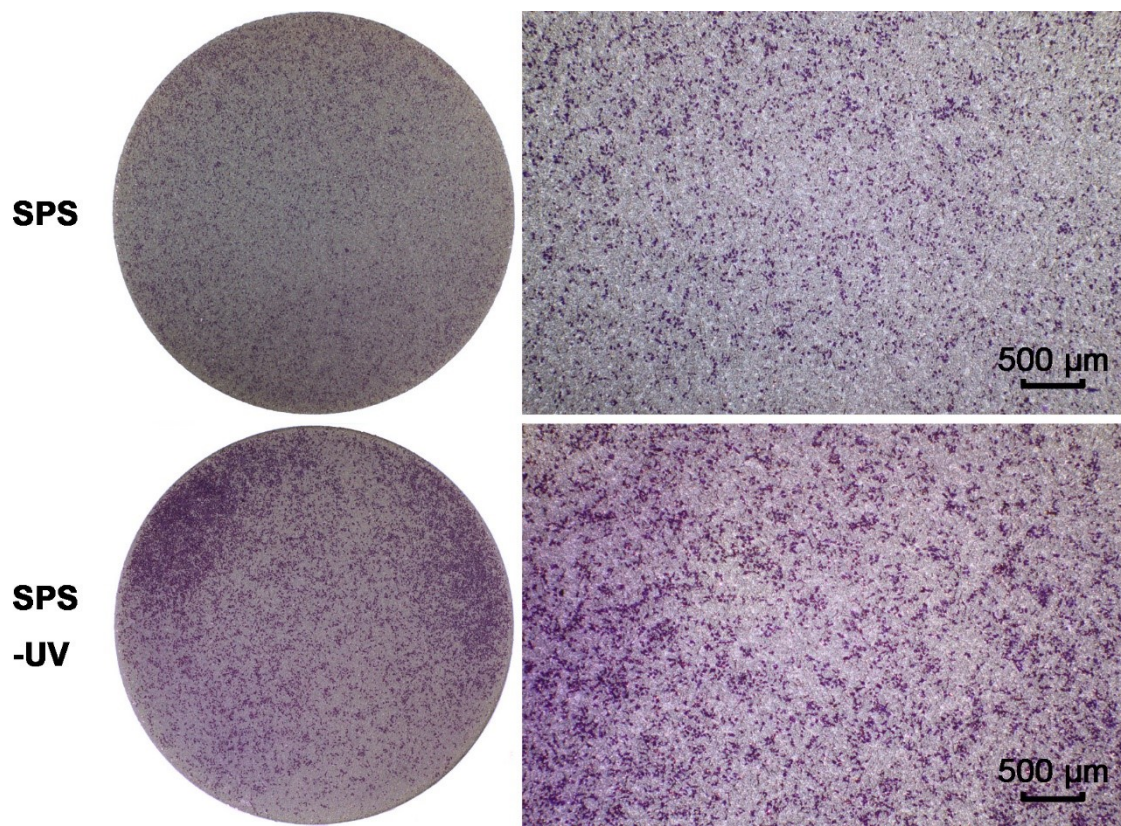
Fig. 3- 27 Crystal violet staining of SPS surfaces with and without irradiation
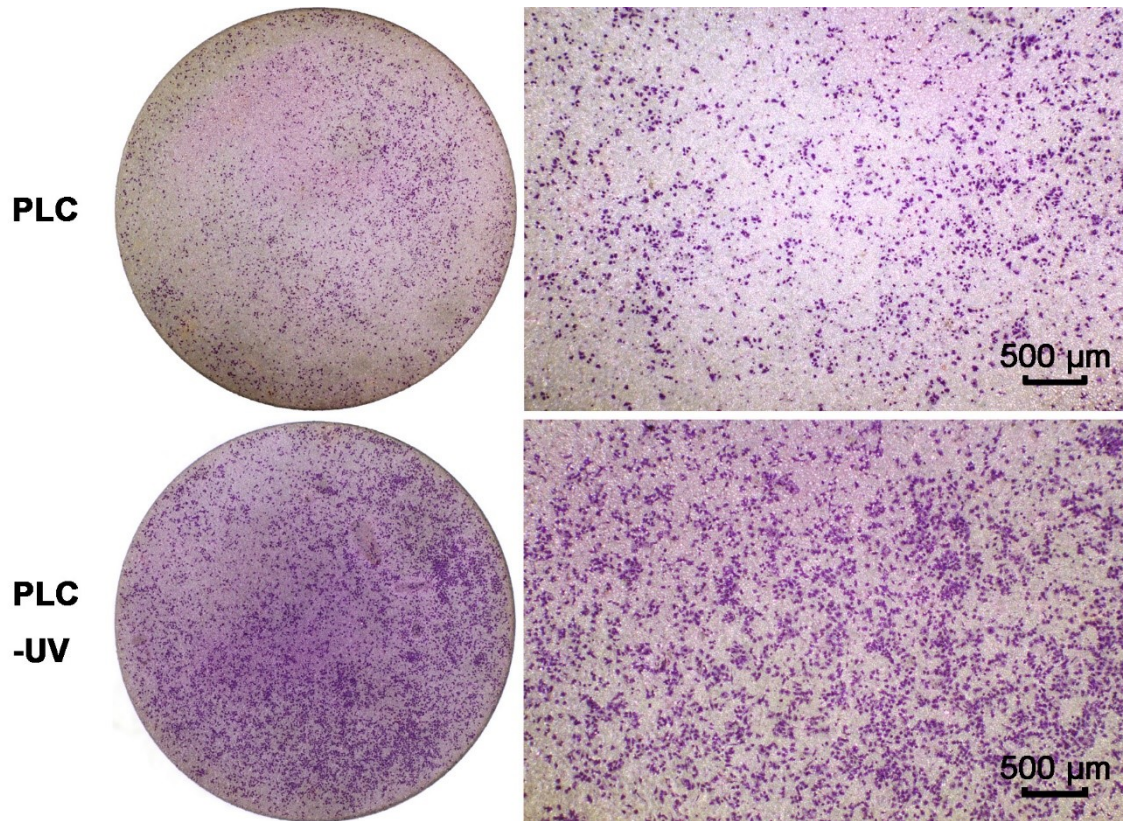
Fig. 3- 28 Crystal violet staining of PLC surfaces with and without irradiation
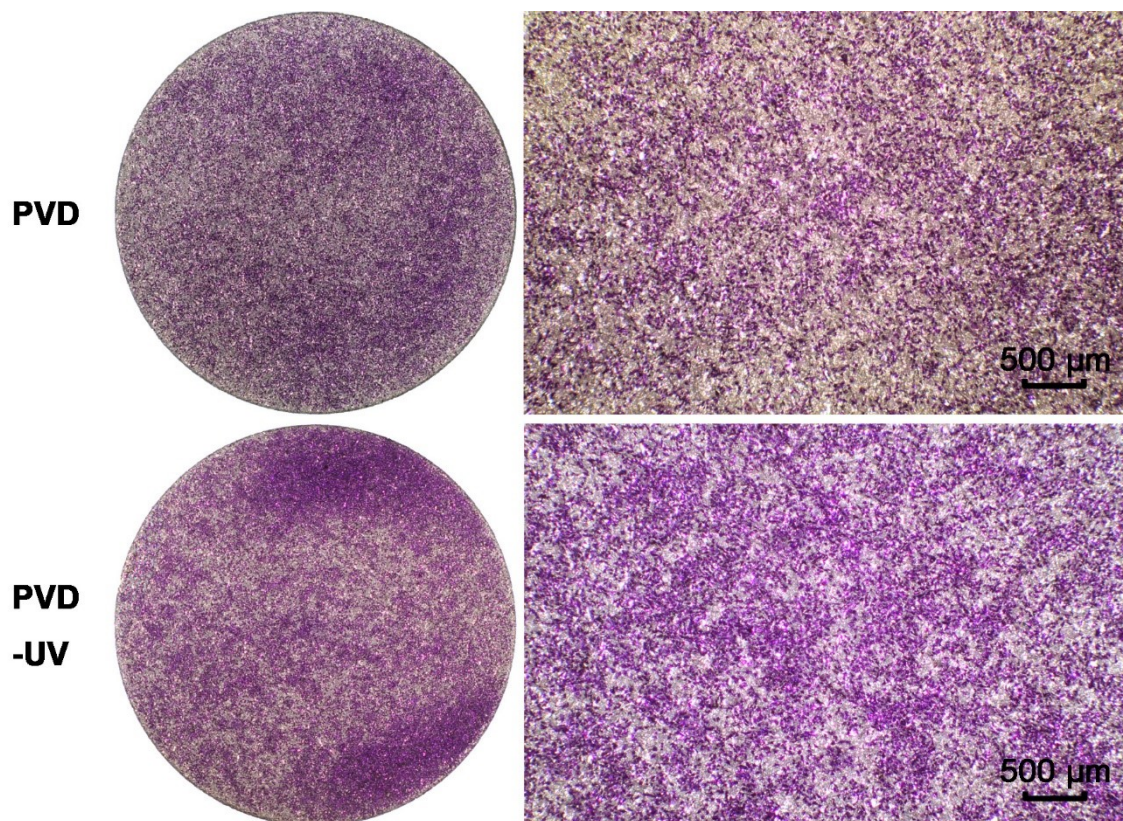
Fig. 3- 29 Crystal violet staining of PVD surfaces with and without irradiation

Additionally, cell coverage was determined by elution of the bound crystal violet, followed by photometric quantification. Fig. 3- 30 shows the relative amounts (in relation to the reference S) of the crystal violet dye that was dissolved from the stained osteoblasts on different experimental surfaces. The results from this quantitative assessment further confirmed the findings from the previous macroscopic observation. As is revealed in the figure, the amount of crystal violet dye of the PVD-UV group is approximately two times more than that from the S surface, and is more than 1.5 times the amount of the non-irradiated PVD group. Besides, the SPS-UV group also showed a large relative amount of crystal violet, which was about 1.7 times as much as those of both the S and the non-irradiated SPS groups were. For the PLC group, although the amount of the dissolved dye increased significantly after UVA treatment, it was still not significantly different from those of the references. In summary, the UVA irradiation effectively improved the osteoblast coverage on all anatase surfaces, especially for the PVD and SPS surfaces.
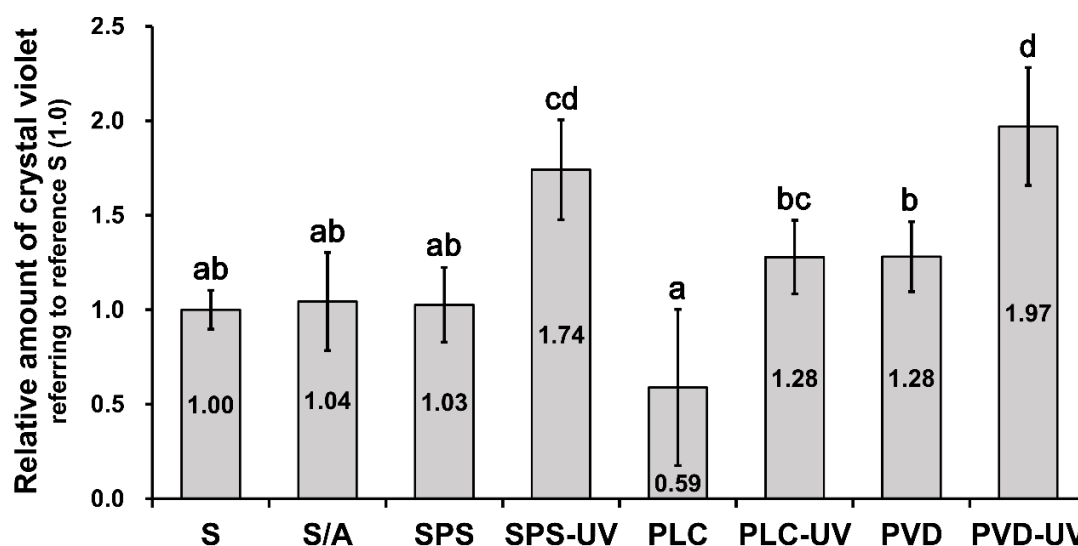
Fig. 3- 30 Relative amounts of the dissolved crystal violet dye from SAOS-2 osteoblasts cultivated on different surfaces after a four-day culture. For each experiment replication, the mean absolute absorbance value of the crystal violet of the reference S was set to 1.0 and the relative amount in relation to this value was calculated for the other surfaces. The identical superscripts in the figure denote no significant difference. ($p < 0.05$)

(3) Differentiative activity of osteoblasts

As a mark of osteoblast differentiation, mineralized nodules were determined by ARS staining after 21 days of cell culture. In this study, the osteoblasts were investigated under two different culture conditions: i. in the normal culture medium, and ii. in the differentiation inducing condition (100 μM L-ascorbic acid 2-phosphate, 10 mM β-glycerol phosphate disodium, and 4 μM dexamethasone supplemented in normal medium). Therefore, this section consists of two parts that respectively show the osteogenic differentiation of osteoblasts in two different culture conditions.

1) Differentiative activity of osteoblasts in normal culture condition

First, Fig. 3- 31, Fig. 3- 32, Fig. 3- 33 and Fig. 3- 34 respectively illustrate nodule formation by exemplary pictures of the ARS staining of the non-osteogenic-induced groups with and without UVA irradiation. For each displayed group, a photo of the whole sample and another one in high magnification are presented.

The osteoblasts of all groups exhibited positive ARS staining, which indicated that calcium phosphate deposits formed on all tested surfaces. As can be seen in the figures, the dark-red stained nodules of different groups are in various amounts and sizes. Before UVA irradiation, the S/A surface exhibited the greatest number of nodules with the largest sizes. The mineralized status of the PVD surface was similar to that of the S surface, and the nodules on SPS surface outnumbered both of them. The PLC surface also showed nodules with large sizes, but the distribution of them was quite uneven. After UVA irradiation, the amounts of mineral deposits on both SPS and PVD surfaces increased significantly. However, it is difficult to notice a difference between PLC groups with and without irradiation.
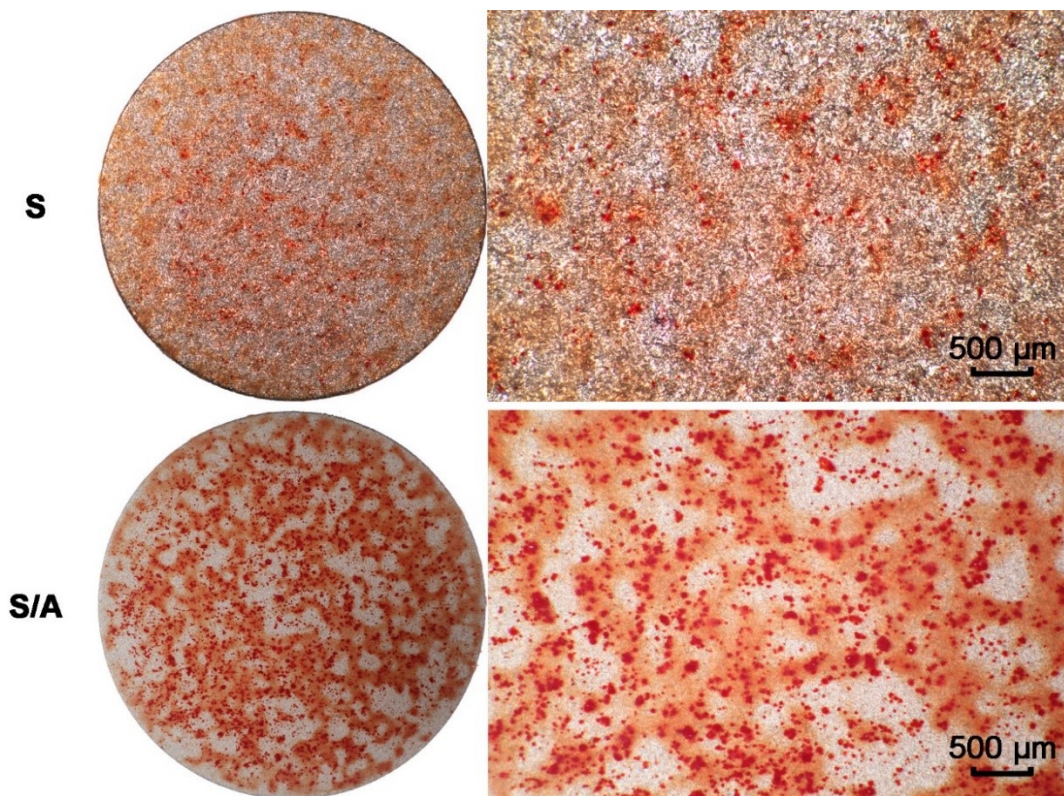
Fig. 3- 31 ARS staining of S and S/A surfaces under normal culture condition (references)
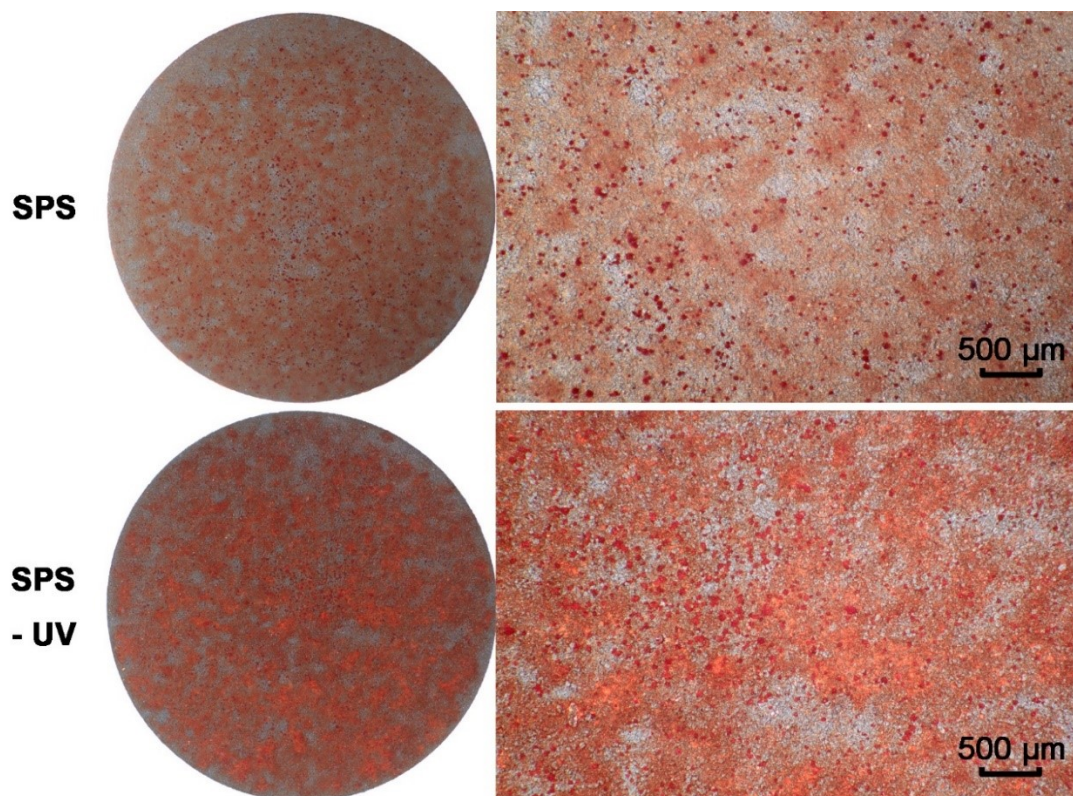
Fig. 3- 32 ARS staining of SPS surfaces with and without UVA irradiation under normal culture condition
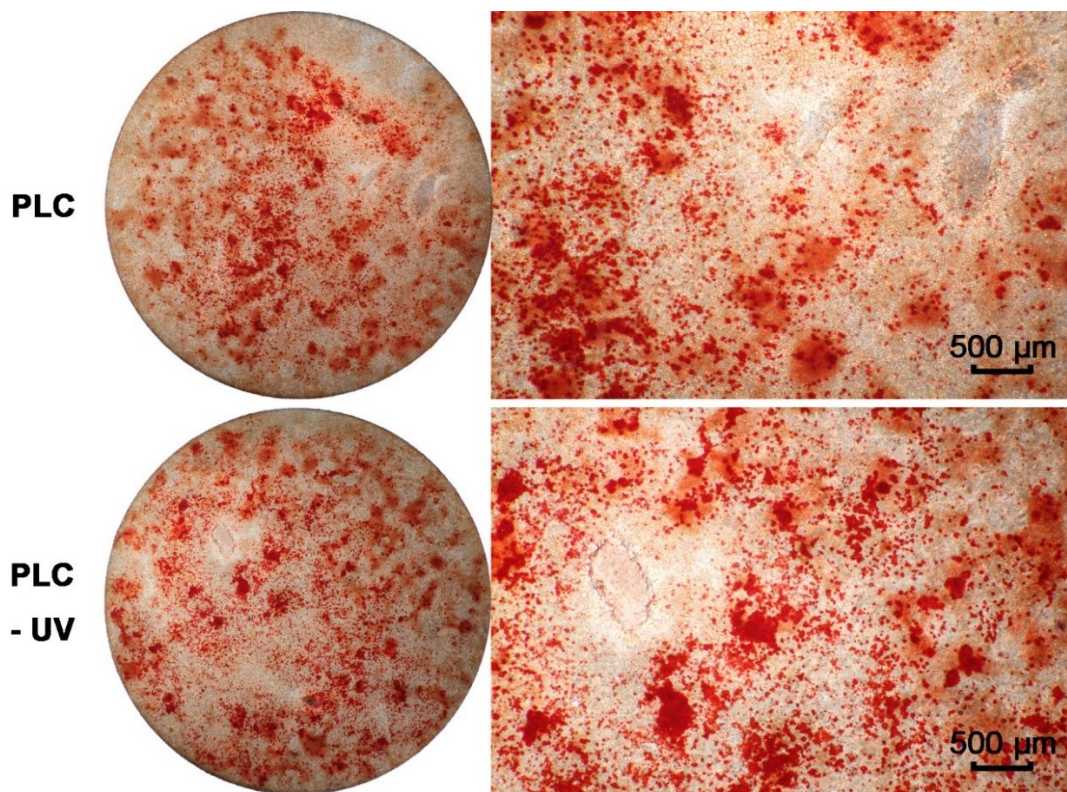
Fig. 3- 33 ARS staining of PLC surfaces with and without UVA irradiation under normal culture condition
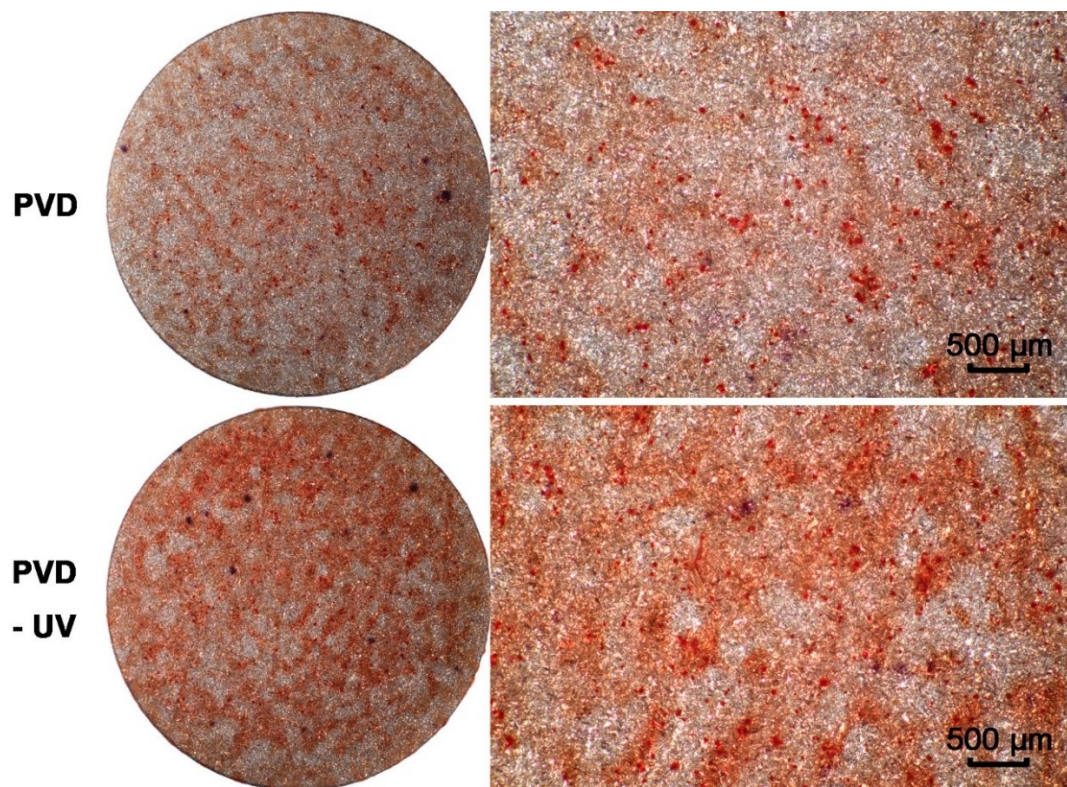
Fig. 3- 34 ARS staining of PVD surfaces with and without UVA irradiation under normal culture condition

In addition, Fig. 3- 35 depicts the quantification of the ARS dye that was dissolved from the stained mineral deposits of non-induced groups with and without UVA irradiation. This spectrophotometric quantification confirmed the above observations.

Before UVA treatment, the relative amount of ARS of the S/A group was 2.15 times larger than that of the S group. The value of the PVD group was at the same level with that of the reference S, but was significantly lower compared with the other two anatase surfaces. Besides, the differentiative activity of the SPS and the PLC surfaces had no significant difference, but were increased 1.52 and 1.83 times, respectively, compared with the reference S.

After UVA treatment, the relative amounts of the SPS and the PVD surfaces raised significantly compared with the non-irradiated ones. The irradiated SPS surface even showed a high amount comparable to the reference S/A. The differentiative activity of the cells on the PLC surface with and without irradiation was not significantly different from the reference S/A. Interestingly, the PLC surface was the only anatase modification that did not show a significantly enhanced cell differentiation after illumination. By far the highest mineralization was detected on the TCPS.
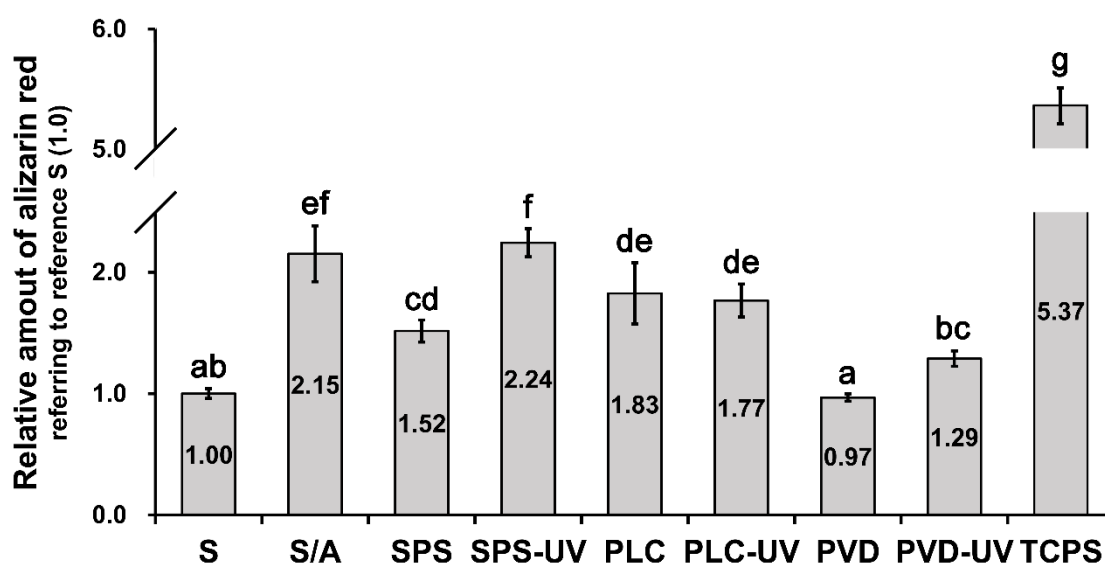
Fig. 3- 35 Relative amounts of the dissolved ARS dye from the mineral nodes generated on the non-osteogenic-induced groups with and without UVA irradiation after a 21-day culture. For each experiment replication, the mean absolute absorbance value of the ARS of the reference S was set to 1.0 and the relative amount in relation to this value was calculated for the other surfaces. The identical superscripts in the figure denote no significant difference. ($p<0.05$)

2) Differentiative activity of osteoblasts in differentiation inducing condition

From another aspect, Fig. 3- 36, Fig. 3- 37, Fig. 3- 38 and Fig. 3- 39 respectively illustrate the exemplary pictures of the osteogenic-induced groups with and without UVA irradiation. For these pictures, a different photographic set up was used. The photographs of the non-induced groups were taken with the light source located right above the samples to avoid shadows. The following pictures of the induced groups were taken with the light source inclined to the left side of the samples to create shadows and to distinguish the morphologies of the mineralized deposits on the different surfaces. Without this modification, the pictures of the different induced groups would have looked nearly the same, because the nodules almost completely covered all tested surfaces.

From the figures, we can clearly see that the osteogenic induction improved the formation of mineral deposits largely. The coverage area of the dense red-stained deposits was boosted on all kinds of surfaces compared with the corresponding non-induced ones. For the reference S/A, the deposits covered the whole surface. Besides, they also covered the vast majority of the SPS and the PVD surfaces except some tiny fractions on the edge. The uncovered area on the S and the PLC surfaces were more evident compared with other groups. Moreover, after irradiation, it seemed that more deposits formed on the edge of SPS and PLC surfaces.

Fig. 3- 36 ARS staining of S and S/A surfaces by osteogenic induction

Fig. 3- 37 ARS staining of SPS surfaces by osteogenic induction with and without UVA irradiation
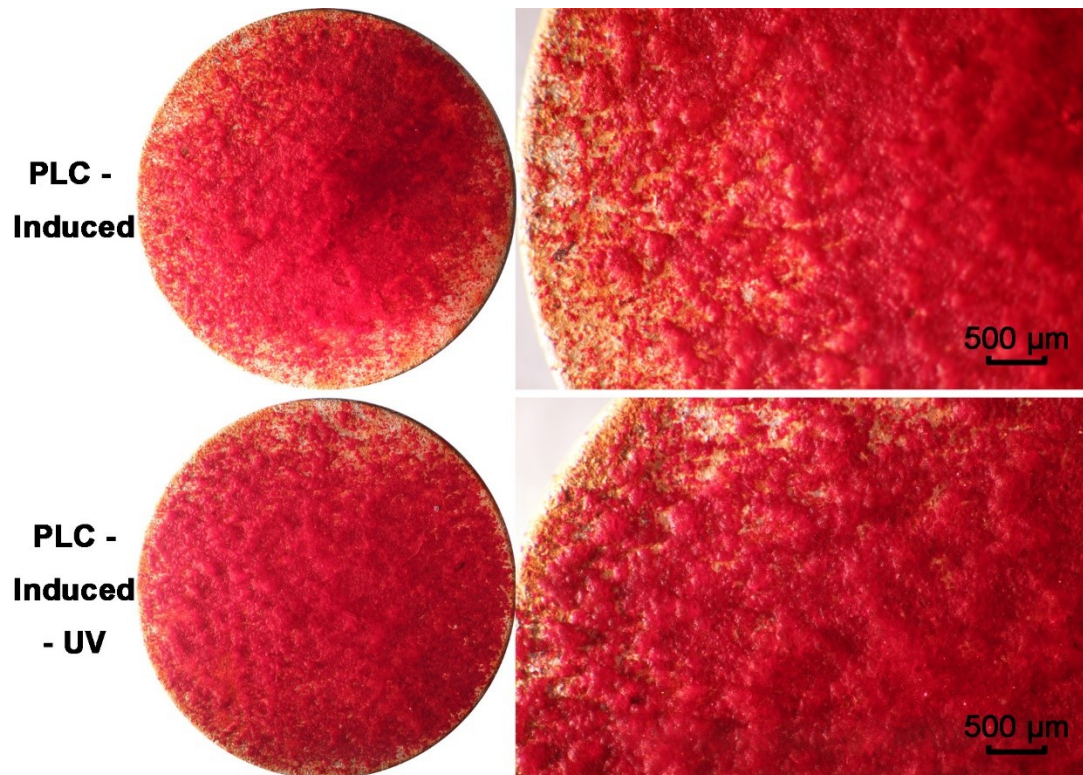
Fig. 3- 38 ARS staining of PLC surfaces by osteogenic induction with and without UVA irradiation

Fig. 3- 39 ARS staining of PVD surfaces by osteogenic induction with and without UVA irradiation

Additionally, Fig. 3- 40 demonstrates the relative amounts of the ARS dye of the osteogenic-induced groups with and without UVA irradiation. As can be seen in the figure, the osteogenic induction significantly narrows the gaps between all tested groups and the TCPS control. The relative amount of ARS of the induced TCPS control was 1.77-fold compared with the 5.37-fold in the non-irradiated TCPS control. Besides, the induction also reduced the differences among the experimental groups. This indicates that the osteogenic induction might lower the surface-sensitivity of osteogenic differentiation. In addition, the UVA treatment significantly improved the differentiative activity of the SPS and the PLC groups. After irradiation, the relative amount of the SPS group was significantly larger than that of the reference S/A was. The PLC and the PVD groups also exhibited the same level of the mineral deposition amounts compared with the reference S/A.
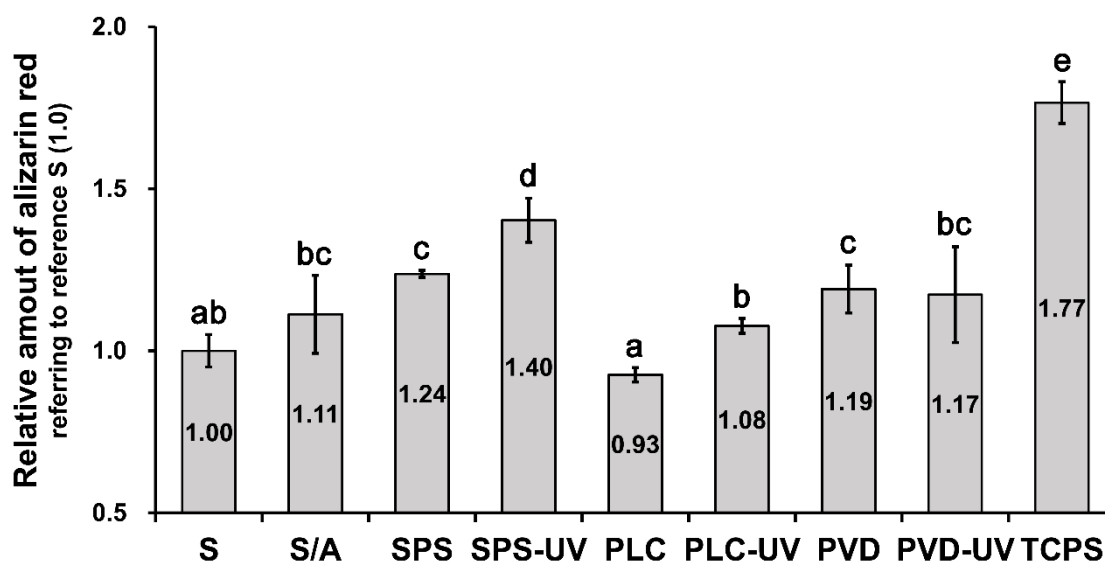
Fig. 3- 40 Relative amounts of the dissolved ARS dye from the mineral nodes generated on the osteogenic-induced groups with and without UVA irradiation after a 21-day culture. For each experiment replication, the mean absolute absorbance value of the ARS of the reference S was set to 1.0 and the relative amount in relation to this value was calculated for the other surfaces. The identical superscripts in the figure denote no significant difference. ($p<0.05$)

Moreover, the osteoblasts cultured on different surfaces reacted differently to the induction. Fig. 3- 41 showed the comparison of the absolute optical density values of the non-induced groups and the corresponding induced groups in ARS staining. The figure illustrates that the larger increase of deposition amount caused by the osteogenic induction were detected on the PVD (13.1 times) and the S (10.65 times) surfaces compared with the SPS (8.70 times) surface, while the S/A (5.51 times) and the PLC (5.40 times) groups exhibited the least increase of differentiative activity among all tested surfaces.

In summary, without the osteogenic induction, the SPS and the PLC surfaces enhanced differentiation of osteoblasts, both with and without UVA irradiation, compared with the sandblasted reference. With UVA treatment, the mineral deposition amounts on these two anatase surfaces achieved the same level of
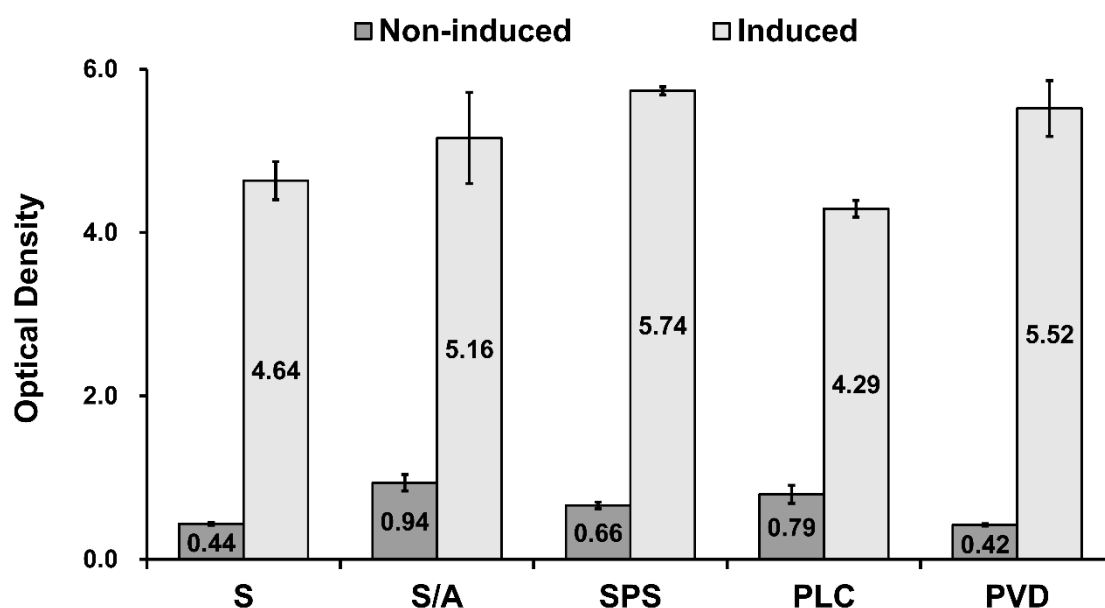
Fig. 3- 41 Comparison of the absolute optical density values of the non-induced groups and the corresponding induced groups in ARS staining ($\bar{x}$ ± s). All groups mentioned in this figure were without UVA irradiation. The extraction solution of the induced groups was diluted so that the absorbance differences could be measured sensitively by the ELISA reader. Consequently, the absolute optical density values of the induced groups were converted according to the dilution rates.

that on the S/A surface, which was successfully applied in many clinically used implant systems at present. With osteogenic induction, the SPS and the PVD surfaces showed superior osteogenic differentiation capabilities compared with the reference S even without irradiation. The highest amount of mineral deposition in this part of ARS staining was determined on the irradiated SPS surface, where the osteoblasts generated even more mineral deposits than those on the S/A surface did. Therefore, we can conclude that, none of the photo-activated anatase coatings compromises the differentiation capability of osteoblasts in comparison with the original S surface, and the SPS surface with UVA irradiation even improved the osteoblast differentiation compared with the S/A surface, at least under osteogenic induction conditions.

4. Discussion

The clinically used dental implants have inevitably been stored for a certain period between being manufactured and being placed in patients, which normally results in a time-dependent "aging" or "biological degradation" of the implant surface [35]. The UV-induced photocatalysis of anatase surfaces is considered as an elegant chair-side procedure to transform the "aged" implant surface from hydrophobic to hydrophilic, and from bioinert to bioactive, which eventually improves the osseointegration of the stored implant to the level a freshly made implant can achieve.

A titanium surface with a high proportion of anatase can be achieved by different techniques. In the present study, three differently manufactured (SPS, PLC and PVD) anatase coatings of a typical sandblasted titanium implant surface were first physicochemically characterized. In addition, the influence of the UVA pretreatment on the proliferative activity, the cell-covered area and the differentiative activity of the human osteoblast cells cultivated on these three kinds of anatase surfaces were evaluated, and compared with the respective values of the original sandblasted surface (S) and the commonly applied sandblasted and acid etched surface modification (S/A).

The aim of the current study was to find out the anatase surface that shows the most potential to improve the osseointegration. The insight into how the surface characteristics of different anatase surfaces affect the biological behavior of osteoblasts will be conducive to achieve a fast and firm osseointegration between dental implant and alveolar bone.

4.1 Effect of the UVA-induced photocatalysis on the biological response of human osteoblasts

(1) Photocatalysis activity of the anatase coatings

In this study, we first concerned the influence of the photocatalysis activity of the experimental surfaces on the biological behavior of osteoblasts, because it affects the efficiency of the UVA-induced decontamination and hydrophilization of the implant surface. Therefore, we first evaluated the photocatalytic activity of the anatase surfaces by measuring the contact angle changes before and after UVA irradiation. The results (Fig. 3- 13) showed that the PVD surface exhibited a favourable photocatalytic activity, proves by the generation of a superhydrophilic surface with a contact angle of 0° after UVA irradiation for just ten minutes. However, by contact angle measurement it was not possible to assess the photocatalytic activity of the SPS surface, since the contact angle of the SPS group displayed 0° even before UVA irradiation, which was most likely due to a structural effect. For quantifying the photocatalytic activity of the SPS surface, the methylene blue degradation test was conducted. In general, this test is considered as a model system to determine the activity of a catalyst to decompose organic molecules. Based on the results of this test (Fig. 3- 18), the degradation rate constant of the SPS group was the highest (2.1/h) among those of all the three anatase variants; while the photocatalysis activity of the PVD group was substantially lower, but still higher compared to the PLC group (rate constant, 0.66 vs. 0.34/h, resp.), just as in the contact angle measurements. However, it should be noted that, although the rate constant of the SPS group was about three times as high as that of the PVD group, the developed area ratio (Sdr) of the SPS group was also approximately three times that of the PVD group (Tab. 3- 2). Thus, the overall higher photocatalytic activity of the SPS surface may be attributed to the larger catalytically effective area whereby the quantum efficiency per area of both surfaces might be similar.

(2) Influence of the UVA-induced photocatalysis on the biological behavior of osteoblasts

After characterising the photocatalysis activity of the anatase coatings, the influence of the UVA-induced photocatalysis on the biological behavior of osteoblasts was further investigated. The results showed that the UVA irradiation led to the "activation" of all anatase variants, resulting in significantly increased proliferation of osteoblasts and generally enhanced differentiation.

For proliferation, this "activation" effect was most pronounced in the PVD group. The results of the XTT test (Fig. 3- 25) revealed that, after four days of culture, the proliferation rate of osteoblasts on the irradiated PVD surface was more than two times higher than that of the original sandblasted surface. The outcomes of the surface coverage measurement (Fig. 3- 30) corresponded well to the findings of the XTT test. They confirmed again that the UVA pretreatment significantly improved the proliferation of osteoblasts on all the irradiated anatase surfaces, and the coverage area of osteoblasts on the PVD-UV surface was the largest.

Likewise, the osteogenic differentiation was also generally enhanced by the UVA irradiation (Fig. 3- 35), represented by the increased formation of calcium deposits in the irradiated anatase groups. Differentiation of osteoblast, however, was less enhanced by UVA irradiation than proliferation. The enhancement of differentiation by UVA was tested under normal as well as under differentiation inducing culture conditions, using an inducing medium with additives. Under normal culture conditions, calcium deposition was most pronounced on the S/A surface, being more than two times enhanced compared to the original S surface. Owing to the enhancement by UVA irradiation, the amount of calcium deposits on the SPS surface also reached this level. Moreover, under osteogenic culture conditions (Fig. 3- 40), the calcium deposition of the SPS-UV group even

outnumbered that of the S/A surface. On the other hand, cells on the PVD surface, which exhibited the strongest proliferation in the previous tests, displayed an indifferent osteogenic differentiation state that showed no significant difference compared with the original S surface. What is interesting to be discussed is the differentiation of osteoblasts on the PLC surface, which is inhomogeneous as can be seen in Fig. 3- 33. Some areas on the PLC surface are quite suitable for osteoblasts to differentiate since the calcium deposits in these areas are dense and large compared with other surfaces. Even so, still other areas are quite unfavorable for osteoblasts to differentiate so that almost no deposition can be found in these areas. Accordingly, the augmentation of differentiation by the osteogenic induction on the PLC surface might be confined in limited areas, resulting in a compromised average enhanced extent as being evaluated as a whole (Fig. 3- 40). Actually, unlike on other surfaces with homogenously distributed mineral deposition, the amounts of the mineral nodules on the PLC surfaces under inducing conditions decreased from the center to the edge (Fig. 3- 38), which generated a height difference between the nodules in the center and on the edge. This difference was so obvious in the non-irradiated group that, when taking the pictures in high magnification, the center and the edge of PLC samples even cannot be viewed simultaneously clear with the same focus distance. Interestingly, the UVA irradiation appeared to ease this situation. The nodules were distributed more evenly and the height difference seemed to decrease in the irradiated PLC group compared to the non-irradiated one.

From the results above, we can conclude that, through the improvement of the biological activity of anatase surfaces, the influence of UVA irradiation on osteoblast behavior at least lasted to three weeks after the cells were seeded on the surface. This time point is regarded clinically critical during the survival of implant, since the total stability of most clinical-used implants normally reaches

the lowest level during this period after implantation. The enhancement of the proliferation and differentiation of osteoblasts in the initial three weeks could clinically support the acceleration of new bone formation, which would enhance the total stability of the implant and make early or even immediate loading possible. Many hydrophilic surfaces, e.g. modSLA, were found to significantly enhance the proliferation and differentiation of osteoblasts compared to the hydrophobic surfaces during three weeks long investigations [78, 79]. Our results indicated that the stimulation from the UVA-induced photocatalysis via the anatase surfaces tested in this study obviously lasts as long as the effects of the hydrophilic surfaces in other studies.

(3) Mechanisms of the bioactivity improvement by UVA-induced photocatalysis

Currently, there are three widely accepted explanations for the physiochemical alteration of the titanium surface caused by the UV-induced photocatalysis, which subsequently enhances the cell responses.

The first one is the decomposition of the hydrocarbon contaminations. Under ambient conditions, organic molecules continuously accumulate at the implant surface. The amount of accumulated organic contaminants is strongly correlated with the osteoblast activity [80]. When UVA illuminated the anatase coatings, the oxygen molecules reacted with the excited electrons, while the water molecules reacted with the electron holes. Both of these reactions created active radicals, such as O^{2-} and $\cdot OH$, which decompose the organic contaminants by breaking the chemical bonds by oxidation, and eventually clean the titanium surface and make it hydrophilic [81].

The second suggested reason for the enhancement of cell response is the introduction of hydroxyl groups at the surface. During photocatalysis, the water molecules occupy the oxygen vacancies, generating a hydroxyl group layer on the surface in the form of Ti-OH. This process is described as the surface hydroxylation of TiO_2 by water dissociation [82]. Like decontamination, the increasing number of hydroxyl groups here leads to a hydrophilic conversion of the titanium surface [83]. Besides, these hydroxyl groups also facilitate the chemical interaction between the titanium surface and the osteoblasts [84], which makes the hydrophilic surface also "protein- and cell-philic", and subsequently exhibits the significantly increased cell proliferation and differentiation compared to the surface without UVA irradiation, as demonstrated in this study.

Last but not the least, the UV-induced photocatalysis also results in a transformation of the electrostatic status of the TiO_2 surface from electronegative to electropositive [51]. In general, most proteins, including fibronectin that plays a major role in cell adhesion [85], are negatively charged in the physiological environment. Therefore, the UV-induced electrostatic status transformation promotes the adsorption of cell attachment-related proteins on the titanium surface. Besides, the positively charged surface could even directly attract the anionic cells to attach without protein as an intermediate layer [50].

As the result of the synergistic effects of the factors discussed above, a positively charged, hydrophilic surface with increased amount of hydroxyl groups is generated by UVA irradiation of the anatase coatings in this study. These physiochemical surface alterations give rise to a different conditioning by the proteins absorbed on the titanium surface. For example, the hydrophilicity has been described as a critical determinant for the adsorption of proteins. Wei et al. [86] studied the influence of surface wettability on the competitive protein

adsorption and the initial attachment of osteoblasts. They found that, in the presence of a cell adhesion-promoting protein such as fibronectin (Fn) and a cell adhesion-inhibiting protein such as albumin (Alb), the Fn preferred to adsorb on the hydrophilic surface, whereas the Alb was prone to adsorb on the hydrophobic surface. The efficiency of the subsequent osteoblast adhesion was considered to depend on the balance of the competing adsorption between the adhesion-promoting and adhesion-inhibiting protein. Accordingly, the hydrophilic surface, which adsorbed more Fn, resulted in enhanced cell attachment, instead of the hydrophobic one with Alb that interfered with osteoblast attachment.

Fn is a glycoprotein of the extracellular matrix that binds to membrane-spanning receptor proteins, the integrins [85]. The increased amount of adsorbed fibronectins on the hydrophilic surface provides more sites for cells to anchor. Besides, this physical linkage between the integrins and the extracellular matrix also participates in various signal transduction processes. Cellular events influenced by the integrin-mediated signalling include cell mobility, proliferation, differentiation and others [87]. One of the well-known signalling mechanisms is the FAK-MAPK pathway. The mitogen-activated protein kinase (MAPK) superfamily is essential in regulating cell mitosis and differentiation [88]. Ge et al. [89] reported that the ligand–integrin binding recruited focal adhesion kinase (FAK) and induced phosphorylation of the molecule, which subsequently activated the extracellular signal-regulated kinases 1/2 (Erk 1/2, members of MAPK family). ERK 1/2 then activated transcription factors, e.g. RUNX2, which eventually enhanced osteoblast differentiation; or allowed cells to progress from G1 to S phase in the cell cycle regulation, which promoted proliferation [90]. The mechanism discussed above illustrates possible ways for the UVA-induced photocatalysis to improve the biological activity of the anatase coatings in this study.

(4) Hydrophilicity versus Contamination degradation

Aita et al. [91] reported that no evidence supporting a direct link between superhydrophilicity and the enhanced bioactivity of titanium surface has been provided in their study. Instead, the level of organic contaminants was strongly correlated with the rates of protein adsorption and cell adhesion [44]. However, these studies did not prove that the improved osseointegration could be induced without superhydrophilicity. Moreover, many studies [92] have demonstrated that the degree of osseointegration in the early healing stage was superior on hydrophilic surfaces compared with hydrophobic ones. Thus, although we cannot propose that hydrophilicity alone is a sufficient condition for bioactivity enhancement, it obviously is a necessary condition, which is beneficial to osseointegration.

From another perspective, the elimination of hydrophobic hydrocarbons from the implant surface is still an important contribution involved in the enhancement of osseointegration. In this study, because the PVD coating was superhydrophilic after a ten-minute UVA irradiation, and the photocatalytic activity of the SPS coating was even higher, taking the convenience of clinical application into consideration, we chose ten minutes as the standard UVA treatment time for the subsequent biological tests.

(5) UVA versus UVC

The UV-induced photofunctionalization of titanium implants has been confirmed by many studies [93-95], indicating that UV promoted several cellular mechanisms involved in osseointegration. Both UVA and UVC irradiation can trigger photofunctionalization; however, the underlying mechanisms are different. The UVA-induced photofunctionalization is achieved by photocatalytic reactions, while the UVC light directly causes the photolysis of contaminants, which cannot

be obtained by UVA due to the lower light intensity [96]. Aita et al. [91] proved that proliferation and differentiation of human mesenchymal stem cells on an acid-etched titanium surface were enhanced by a 48-hour UVC (wavelength 250 nm) pretreatment. They also demonstrated that, although a UVA (wavelength 360 nm) irradiation can generate superhydrophilicity of the titanium surface, neither the proliferative nor the differentiative activity was enhanced by the UVA irradiation. A study from Gao et al. [97] showed similar results, the attachment, spreading, proliferation and differentiation of MG63 human osteoblast cells were promoted by UVC (wavelength 250 nm) instead of UVA (wavelength 360 nm) irradiation on a micro-arc oxidation (MAO) titanium surface for 24 hours. However, in these studies, either the titanium samples were covered by the amorphous titanium dioxide that forms naturally in ambient air, or the superficial films were manufactured by MAO without annealing process which did not produce anatase and rutile effectively [98]. Accordingly, in these studies, due to the lack of catalysts, the rates of UVA-induced photocatalysis should be negligible. Consequently, a decontamination or hydrophilization by UVA irradiation cannot be expected on these surfaces. In contrast, in this study, the results showed that the amounts of anatase in the coatings manufactured by SPS and PVD were sufficient to catalyze UVA-induced photocatalysis which enhanced the proliferation and differentiation of human osteoblasts.

Actually, compared with the direct photolysis induced by UVC, the photocatalysis induced by UVA has the following advantages. First, it takes less time to convert the hydrophobic titanium surface into the hydrophilic one. For example, in this study, it took only ten minutes for the UVA treatment to reduce the contact angle of PVD surface from 40° to 0°, whereas most researchers in other studies mentioned before conducted UVC irradiation continuously for at least 24 hours to switch the amorphous titanium dioxide surface from hydrophobic to hydrophilic.

The results of our study, however, demonstrated that the efficiency of the photocatalysis by UVA catalyzed by the tested anatase coatings was higher than that of the photolysis by UVC.

More importantly, the application of UVA is much safer than that of UVC. Fig. 4-1 [99] shows the effects of ultraviolet light with different wavelengths on the biological activity of cells and biomacromolecules (DNA and protein). As can be seen from the spectral curve of cell inactivation, UVC has the highest cell inactivation capacity, because DNA absorbs mainly UVC irradiation. The most commonly used Hg-low pressure lamps in the relevant studies have their maximum energy output in this range. Thus, the optical energy of UVC, which directly decomposes the organic contaminations on the "aged" titanium surface, irreversibly damages the DNA as well. On the contrary, the UVA with a wavelength of 385 nm barely shows capability to inactivate cells, because it is
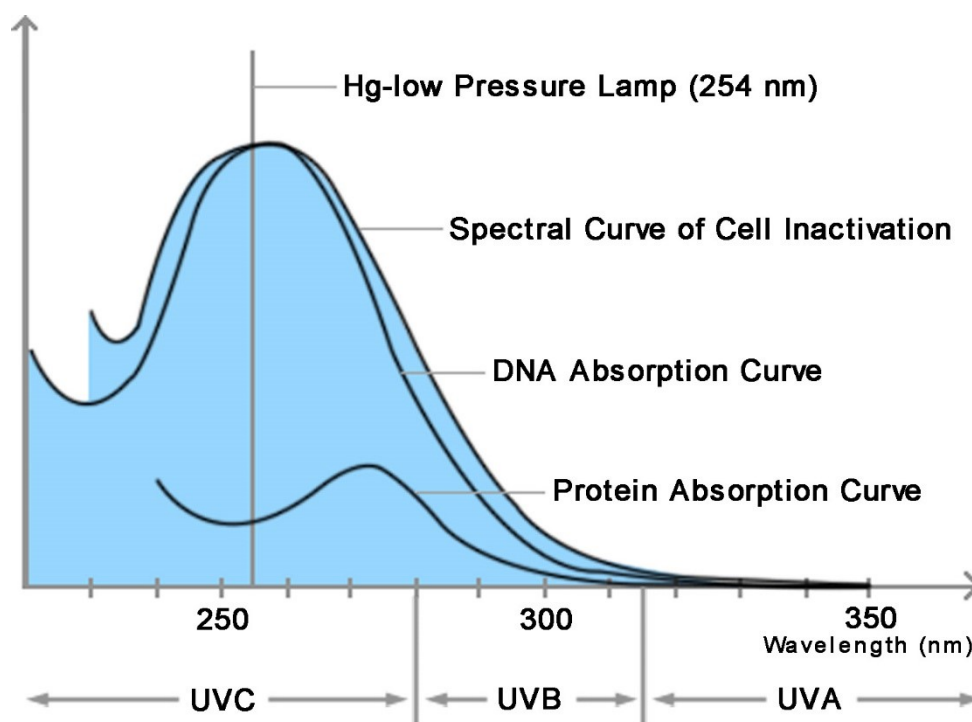
Fig. 4- 1 Effects of ultraviolet light with different wavelengths on the biological activity of cell and biomacromolecules (DNA and protein) [99]

not absorbed by native DNA and proteins [100]. This indicates a safer application scenario in the clinic, especially for the proposed treatment of patients with peri-implantitis, who need a thorough removal of the bacterial and organic contaminants from the implant surfaces in the mouth. The currently recommended protocol to deal with this situation is either to mechanically brush and polish the implant surface for mild symptoms, or directly grind off all the threads and surface structures in the peri-implantitis area, followed by smoothing and polishing of this section of the implant in case of severe symptoms [101]. Both of the measures damage the morphology of the implant surface to various degrees, which might compromise the reintegration of the implant into the bone. The UVA-induced photocatalysis by anatase coatings, as was shown in this study, offers an alternative way to support cleaning of the implant surface that not only maintains the surface morphology, but also regenerates a biologically active surface for the osseointegration.

Actually, UVA (340-400 nm) has been applied in the phototherapy for a variety of skin diseases, including psoriasis and mycosis fungoides that present oral manifestations [102]. Moreover, the intensity of UVA used in this study (25 mW/cm^2 for 10 min) is classified as the low dose of UVA irradiation (10-20 J/cm^2) applied clinically [103]. The dose-related increased risks of acute or long-term side effects, e.g. carcinogenesis, are greatly minimized for this dose [102], let alone the frequency of the UVA therapy which is normally 2-3 sessions per week [104]. However, since the radical oxygen species produced by the photocatalytic reactions also damage DNA via indirect photosensitizing reactions [100], it is still recommended to separate the tissue from the photocatalytic surface as far as possible. General safety precautions should also be established for both the patients and medical staff if this technique is applied. Further studies may continually optimize novel manufacturing methods to produce anatase coatings

that have higher photocatalysis activity under UVA irradiation, in order to improve the elimination effect of organics. Another approach is to modify the anatase coatings, which shifts the absorption spectrum of the coatings towards longer wavelengths, into the visible light range [105].

4.2 Effect of the surface morphology on the biological response of human osteoblasts

Apart from the physiochemical alterations caused by the UVA-induced photocatalysis, the different surface morphology manufactured by various technologies is also crucial for the biological response of osteoblasts during the early phase of osseointegration [106]. Recently, correlational studies have mainly focused on the micro- and nanomorphology.

(1) Effect of surface micromorphology

Currently, the most commonly used surface modification method for dental implants is the sandblasting and acid etching technique that produces a surface with microroughness that exhibits a favorable osseointegration compared to the smooth surface of machined implants. Previous studies indicated that the micromorphology had impacts on the metabolism, proliferation, as well as the growth factor production of osteoblasts [107, 108]. More importantly, it also gave rise to an enhanced osteogenic differentiation represented by up-regulating the expression of bone-related proteins [109], which eventually increased the level of BIC [110, 111].

In this study, in order to characterize the micromorphology of the experimental surfaces, we first qualitatively documented their surface structures by SEM, and then the 2D and 3D roughness of the samples was quantitatively measured. Except for the PVD surface that showed almost the same micromorphology of

the S surface (because the anatase coating on the PVD surface was too thin to alter the original micromorphology), SEM pictures indicated distinctly different appearances on the micrometer scale among the investigated surfaces.

As suggested by Albrektsson and Wennerberg [112], moderately rough surfaces (Sa between 1.0 and 2.0 µm) exhibited an optimal degree of roughness to promote osseointegration compared with either smoother or rougher surfaces. In this study, the Sa value of all the experimental surfaces, except for the SPS surface, were in this reported optimal roughness range. As mentioned before, unlike all other surfaces, the SPS surface exhibited superhydrophilicity already before UVA irradiation. Even though, maybe because it was too rough for optimal osteoblast adhesion or growth, the proliferation rate of cells in the SPS group was not superior to those of other surfaces during the four-day culture. Besides, Arvidsson et al. [113] suggested to use the core fluid retention index (Sci) to predict the biological outcome of implants. They claimed that a low Sci seemed to be beneficial for bone-anchored implants. The SPS surface, again, showed a significantly larger Sci compared to the other surfaces. This result confirmed the hypothesis above and indicated that not only the vertical height but also the horizontal dimension of the SPS surface were not as ideal as those of the other investigated surfaces were. However, based on the roughness parameters alone, not all effects caused by the surface micromorphology can be predicted. For instance, in this study, the micromorphology of the S/A and PLC surfaces represented dissimilar and specific features in the SEM pictures, and the proliferation rate of the PLC group was significantly lower than that of the S/A group was, but all the tested 3D roughness parameters of the S/A and PLC surfaces were without significant difference.

Last but not the least, the surface micromorphology also affected the differentiation of osteoblasts in this study. In the ARS staining test without osteogenic induction, osteoblasts showed strongly enhanced differentiation on the S/A surface compared to the original S surface, and the amount of mineral deposition in the S/A group was also the largest among all the non-irradiated groups. This result confirmed again that the typical pit structures of the S/A surface promoted a tendency of Saos-2 cells to shift toward an osteogenic phenotype as a previous study [114] suggested, and also indicated that, among all the tested surfaces, the S/A surface had the most favorable micromorphology for osteoblasts to differentiate.

(2) Effect of surface nanomorphology

Apart from the micromorphology, the influence of nano-featured surface structures on the cell response is another important factor. Studies indicated that, by influencing the cell movement, or through the cytomembrane deformation it caused, the nanomorphology at the cell–surface interface could be sensed by cells through several channels. Signal transduction can be mediated by integrins, by stretching-activated ion channels, or the CD44 transmembrane proteins on the cell surface [115]. The sensed information could be transmitted by the cytoskeleton reorganization or the corresponding signal pathway, and eventually regulate gene transcription and protein translation [116]. Many studies [117-119] demonstrated that the nanomorphology of the implant surface played a vital role in osteoblast reactions such as adhesion, proliferation, differentiation, and the final bone formation. The size, shape, and arrangement of the nano-features, as well as the distance between them were all proven to affect the cell behavior in response to the surface nanomorphology [120-122].

In this study, the SEM images (Fig. 4- 2) depicted that the PVD treatment superimposed an extremely thin anatase coating in the form of spherical nano-features on the original S surface, which barely changed micromorphology of the sandblasted samples. In the XTT test, the non-irradiated PVD surface significantly increased the proliferation rate of osteoblasts compared with all the non-irradiated groups, including the original S surface. Since the micromorphology of the S and PVD surfaces basically shows no difference, this stimulation of proliferation is obviously mainly triggered by the nanostructure on the PVD samples.
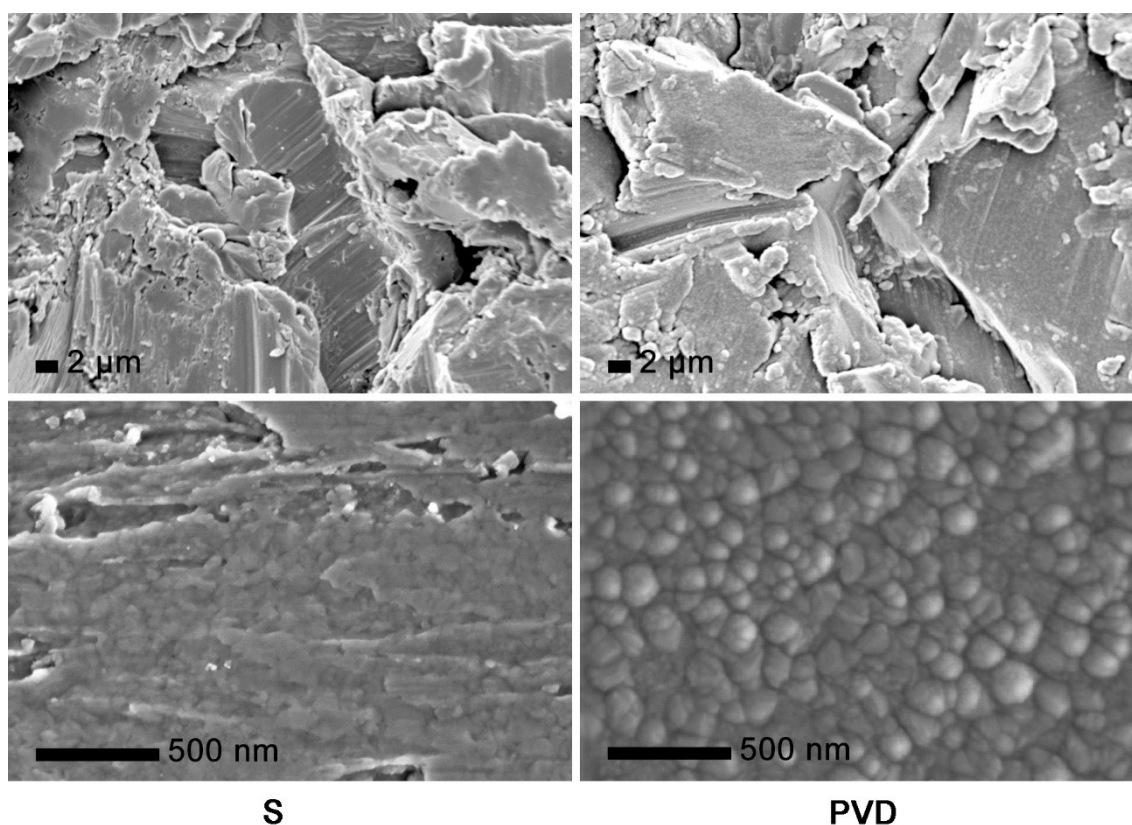
Fig. 4- 2 Comparison of the morphology of the S and PVD surfaces at micro- and nanoscale

The biological stimulating effect of nanomorphology observed in this in vitro study has also been found in vivo. Ogawa et al. [123] , as well, used the PVD method to produce a nanostructured titanium surface, and evaluated the degree of osseointegration. In an animal study, they found that the push-in value of the

implants with nanostructured surface was 3.1 times higher than that of the original acid-etched implants after healing for two weeks.

Additionally, the nanostructures on the S/A and SPS surfaces are interesting to be discussed as well. In the SEM images at high magnification (Fig. 4- 3), we can see that countless punctiform nanostructures are distributed dispersedly on the S/A and SPS surfaces, respectively. The density of the nano-points on the SPS surface is higher compared with the S/A surface.

S/A   **SPS**
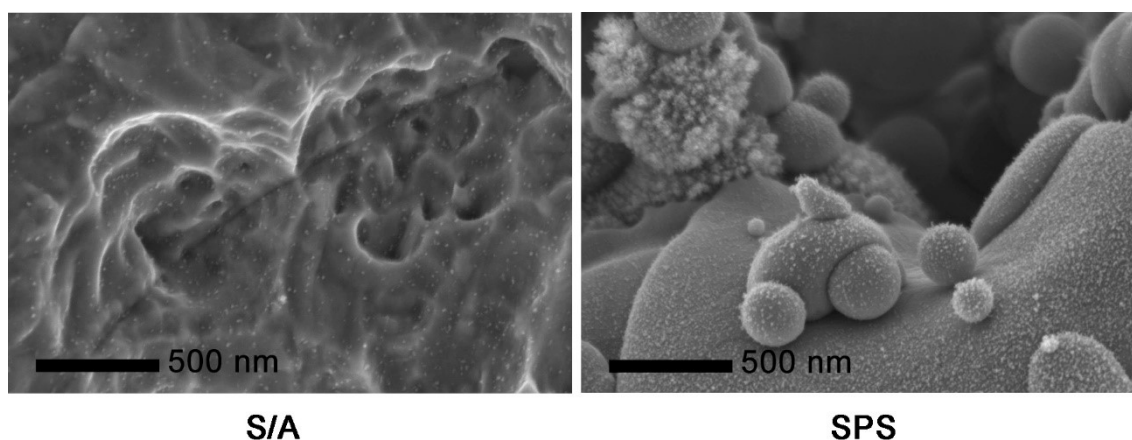
Fig. 4- 3 SEM images of the nanomorphology of the S/A and SPS surfaces

Coincidentally, other publications also demonstrated similar nanostructures developed on a modified sandblasted and acid-etched titanium surface (SLActive). The SLActive manufacturing process requires that the implants are kept in a protective gas atmosphere after etching and subsequently stored in liquid until use. Wennerberg et al. [124] found that the SLActive surface was evenly patterned with point-like nanostructures. They speculated that the acid etching in association with storage in aqueous solution caused restructuring of the outermost titanium oxide layer. In one of their previous studies that also reported these characteristic nanostructures [125], they discussed that, first, the etching process resulted in a hydride layer, which acted as nucleation center; then, the dissociative adsorption of water and the subsequent titanium diffusion

were responsible for the growth of the nanostructures. Thus, in their study, there were no nanostructures present on the sandblasted and acid-etched surface (SLA), whereas all other surface modifications based on the SLActive process clearly exhibited representative nanostructures with different sizes and densities (Fig. 4- 4). However, in this study, we found similar nanoparticles as well on the sandblasted and acid-etched surface (abbreviated as S/A in this study) but with lower density and smaller size compared to those reported by Wennerberg on the SLActive surfaces. The nanoparticles on the SPS surface should be generated from the nano-sized raw materials in the suspension liquid sprayed out from the plasma.
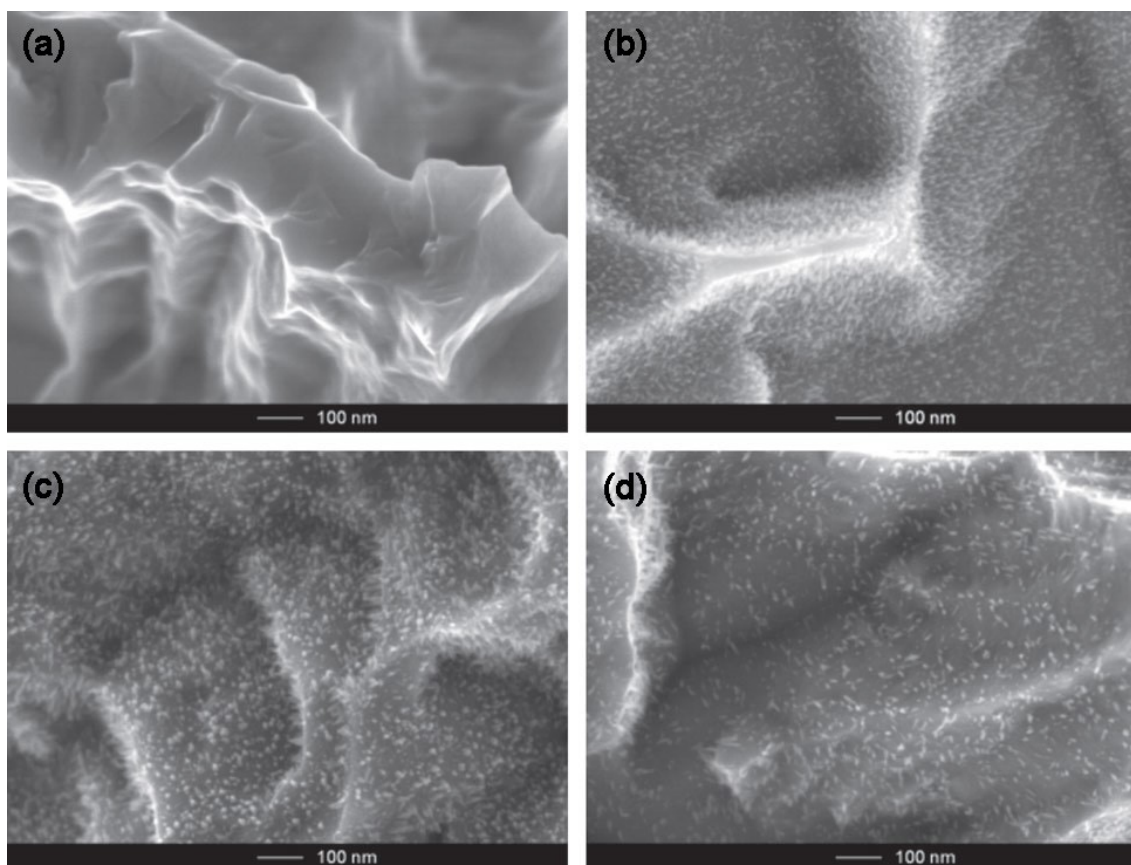
Fig. 4- 4 SEM images [124] of the nanomorphology of (a) the sandblasted and acid-etched surface (SLA); (b) the SLActive surface after aging in aluminum foil; (c) the SLA surface stored in 0.9% NaCl solution (SLActive); and (d) the SLA surface cleaned by oxygen plasma before stored in 0.9% NaCl solution

To investigate the biological effect of the nanomorphology, Wennerberg et al. [124] evaluated the bone response by biomechanical pull-out measurements in the same study. The results showed that the surfaces with nanostructures demonstrated higher pull-out values after healing for four and eight weeks compared to the surface without nanostructures, suggesting that the nanomorphology is important for osseointegration. Besides, many other studies demonstrated the significant influence of nanomorphology on the osteogenic differentiation of both osteoblasts [126] and mesenchymal stem cells [127]. Gittens et al. [128] concluded that, in vitro, the combination of micro- and nanostructures on the superhydrophilic surface had been proven to enhance the differentiation of osteoblasts and the production of local factors.

The results from this study were in accordance with the statements above. Without osteogenic induction (more related to the clinical scenario compared to the induced groups), the S/A surface that showed the punctiform nanostructures enhanced the osteoblast differentiation most among all non-irradiated groups, while the osteoblast differentiation of the SPS group increased and achieved the same level of that of the S/A surface after UVA irradiation. Compared to the hemisphere-like nanostructures on the PVD surface which were more favorable for the osteoblast proliferation, the nanoparticles on the S/A and SPS surfaces seemed to be more advantageous for osteogenic differentiation. However, all the characterization of nanomorphology in this study was qualitatively conducted by SEM, other quantitative investigation methods, such as atomic force microscopy, should be chosen to further evaluate the surface nanomorphology in future investigations.

In summary, this study revealed that both the UVA-induced photocatalysis and the micro- and nanomorphology of the anatase coatings contribute synergistically

to a favorable biological response. The PVD surface excels in promoting the osteoblast proliferation even without UVA irradiation, while the SPS surface has the advantage to enhance the osteogenic differentiation after "activation" by UVA illumination.

5. Conclusion

The aims of this study were to characterize three anatase surface modifications, manufactured by different production processes (SPS, PLC, and PVD), and to evaluate the influence of UVA-induced photocatalysis as well as of the micro- and nanomorphology of these anatase coatings on the biological response of human osteoblasts. The representative sandblasted (S) and sandblasted and acid-etched (S/A) surfaces were used as references for already established surface modifications for titanium dental implants.

First, the micro- and nanomorphology of the experimental surfaces was characterized through SEM images and roughness parameters. The results revealed that, except for the PVD surface that shared a similar micromorphology with the original S surface, all the other three modifications (S/A, SPS, PLC) significantly altered the micro- and nanomorphology of the reference S. The thin PVD coating remarkably modified the S surface at the nanoscale.

The photocatalytic activity of the tested surfaces was assessed by two different effects, i.e. the induction of hydrophilicity (contact angle measurement), and the degradation of an organic reference substance (methylene blue). The results showed that the SPS surface possessed the highest photocatalytic activity, followed by the PVD surface, while the photocatalytic activity of the PLC surface was very low, showing no significant difference to the S and S/A surfaces. Besides, the results of the corrosion immersion test indicated that the SPS and PLC coatings significantly enhance the corrosion resistance of the original surface.

In addition, to distinguish the influence of the irradiation regime from that of the different surface morphology, human osteoblast cells were cultured on the

experimental surfaces with and without UVA pretreatment before onset of the biological tests. The cell proliferation, surface colonization, and osteogenic differentiation were quantified by XTT reduction test, by crystal violet staining, and by alizarin red staining, respectively. The tests revealed that all UVA-irradiated anatase groups demonstrated significantly improved proliferation, surface coverage, and osteogenic differentiation compared with the non-irradiated ones, with one exception: in the PLC group, differentiation was not enhanced by UVA illumination. Moreover, the biological response of osteoblasts was influenced by the different surface morphology of the anatase coatings as well. For instance, the superior proliferation of the cells in the non-irradiated PVD group was obviously triggered by the nanostructures generated on the surface by the PVD process. Additionally to this effect, the UVA irradiation synergistically led to an even further enhanced proliferation based on the effect of photocatalysis. The differentiation of the S/A group was also positively influenced by the presence of micro- and nanostructures. The irradiated SPS surface, which exhibited similar nanostructures as those on the S/A surface, showed the highest osteogenic differentiation capacity among all experimental surfaces.

In conclusion, the results of our study suggest that the UVA-induced photocatalysis in combination with the micro-nano hybrid morphology of the anatase-modified titanium surfaces has the potential to improve the biological response of osteoblasts concerning bony anchorage of implants significantly, which might be of importance in enhancing the bone formation in the initial stage of osseointegration.

6. Zusammenfassung

Die Zielsetzungen dieser Studie bestanden darin, drei unterschiedlich hergestellte Anatas-Beschichtungen (SPS, PLC und PVD) zu charakterisieren, und die Einflüsse der UVA-induzierten Photokatalyse sowie der Mikro- und Nanomorphologie dieser Anatas-Beschichtungen auf die biologische Reaktion von humanen Osteoblasten zu bewerten. Als Referenzen für bereits etablierte Oberflächenmodifikationen von dentalen Titanimplantaten wurden repräsentativ sandgestrahlte (S) und sandgestrahlte und säuregeätzte (S/A) Oberflächen verwendet.

Zuerst wurde die Mikro- und Nanomorphologie der experimentellen Oberflächen durch SEM-Bilder und Rauheitsparameter charakterisiert. Die Ergebnisse zeigten, dass außer der PVD-Oberfläche, die eine ähnliche Mikromorphologie wie die ursprüngliche S-Oberfläche aufwies, alle anderen drei Modifikationen (S/A, SPS, PLC) die Mikro- und Nanomorphologie der Ausgangsoberfläche S signifikant veränderten. Die dünne PVD Beschichtung modifizierte die S-Oberfläche erheblich im Nanometerbereich.

Die photokatalytische Aktivität der getesteten Oberflächen wurde durch zwei verschiedene Effekte untersucht, durch die Induktion der Hydrophilie (Kontaktwinkelmessung) und den Abbau einer organischen Referenzsubstanz (Methylenblau). Die Ergebnisse zeigten, dass die SPS-Oberfläche die höchste photokatalytische Aktivität besaß, gefolgt von der PVD-Oberfläche, während die photokatalytische Aktivität der PLC-Oberfläche keinen signifikanten Unterschied zu den S- und S/A-Oberflächen aufwies. Außerdem zeigten die Ergebnisse der Korrosions-Immersionstests, dass die SPS- und PLC- Beschichtungen die Korrosionsbeständigkeit der ursprünglichen Oberfläche signifikant verbesserten.

Für die biologischen Tests wurden humane Osteoblasten auf den experimentellen Oberflächen (mit und ohne UVA-Vorbehandlung) kultiviert, um den Einfluss des Bestrahlungsregimes von dem der verschiedenen Oberflächenmorphologie zu unterscheiden. Die Zellproliferation, die Oberflächenkolonisierung und die osteogene Differenzierung wurden mittels XTT-Reduktionstest, Kristallviolett-Färbung beziehungsweise Alizarin-Rot-Färbung quantifiziert. Die Ergebnisse zeigten, dass abgesehen von der Zelldifferenzierung in der PLC-Gruppe, die nicht durch UVA-Belichtung verstärkt wurde, alle UVA-bestrahlten Anatas-Gruppen eine signifikant verbesserte Proliferation, flächige Ausdehnung der Osteoblasten und osteogene Differenzierung im Vergleich zu den nicht bestrahlten zeigten. Außerdem wurde die biologische Reaktion der Osteoblasten von der unterschiedlichen Oberflächenmorphologie der Anatas-Beschichtungen beeinflusst. Zum Beispiel war die überlegene Proliferation in der nicht bestrahlten PVD-Gruppe offenbar auf die durch den PVD- Prozess an der Oberfläche generierten Nanostrukturen zurückzuführen. Die UVA-Bestrahlung führte synergistisch zu einer noch weiter verbesserten Proliferation, die auf der Wirkung der Photokatalyse beruhte. Die Differenzierung in der S/A-Gruppe wurde ebenfalls durch die Mikro- und Nanostrukturen positiv beeinflusst. Die bestrahlte SPS-Oberfläche, die ähnliche Nanostrukturen wie die S/A-Oberfläche zeigte, bewirkte die höchste Steigerung der osteogenen Differenzierung unter allen experimentellen Oberflächen.

In Summe zeigen die Ergebnisse dieser Studie, dass die UVA-induzierte Photokatalyse in Kombination mit der Mikro-Nano-Hybrid-Morphologie der Anatas-modifizierten Titanoberflächen das Potential hat, die biologische Antwort von Osteoblasten bezüglich der knöchernen Verankerung von Implantaten signifikant zu verbessern, was für die Verbesserung der Knochenneubildung im Anfangsstadium der Osseointegration von Bedeutung sein könnte.

7. References

[1] Anil Kumar S, Sahoo N, Radhakrishnan V, Sandhu HS. Clinical evaluation of early loaded and unloaded implants in edentulous mandible. Journal of maxillofacial and oral surgery. 2012;11:21-8.

[2] Ganeles J, Zollner A, Jackowski J, ten Bruggenkate C, Beagle J, Guerra F. Immediate and early loading of Straumann implants with a chemically modified surface (SLActive) in the posterior mandible and maxilla: 1-year results from a prospective multicenter study. Clinical oral implants research. 2008;19:1119-28.

[3] Nicolau P, Korostoff J, Ganeles J, Jackowski J, Krafft T, Neves M, et al. Immediate and early loading of chemically modified implants in posterior jaws: 3-year results from a prospective randomized multicenter study. Clinical implant dentistry and related research. 2013;15:600-12.

[4] Davies JE. Understanding peri-implant endosseous healing. Journal of dental education. 2003;67:932-49.

[5] Terheyden H, Lang NP, Bierbaum S, Stadlinger B. Osseointegration--communication of cells. Clinical oral implants research. 2012;23:1127-35.

[6] Salvi GE, Bosshardt DD, Lang NP, Abrahamsson I, Berglundh T, Lindhe J, et al. Temporal sequence of hard and soft tissue healing around titanium dental implants. Periodontology 2000. 2015;68:135-52.

[7] Abrahamsson I, Linder E, Lang NP. Implant stability in relation to osseointegration: an experimental study in the Labrador dog. Clinical oral implants research. 2009;20:313-8.

[8] Branemark PI. Osseointegration and its experimental background. The Journal of prosthetic dentistry. 1983;50:399-410.

[9] Anderson JM, Rodriguez A, Chang DT. Foreign body reaction to biomaterials. Seminars in immunology. 2008;20:86-100.

[10] Corselli M, Chen CW, Crisan M, Lazzari L, Peault B. Perivascular ancestors of adult multipotent stem cells. Arteriosclerosis, thrombosis, and vascular biology. 2010;30:1104-9.

[11] Boudreau NJ, Jones PL. Extracellular matrix and integrin signalling: the shape of things to come. The Biochemical journal. 1999;339 (Pt 3):481-8.

[12] Miyamoto S, Teramoto H, Coso OA, Gutkind JS, Burbelo PD, Akiyama SK, et al. Integrin function: molecular hierarchies of cytoskeletal and signaling molecules. The Journal of cell biology. 1995;131:791-805.

[13] Schwartz MA. Integrins and extracellular matrix in mechanotransduction. Cold Spring Harbor perspectives in biology. 2010;2:a005066.

[14] Ribeiro AR, Oliveira F, Boldrini LC, Leite PE, Falagan-Lotsch P, Linhares AB, et al. Micro-arc oxidation as a tool to develop multifunctional calcium-rich surfaces for dental implant applications. Materials science & engineering C, Materials for biological applications. 2015;54:196-206.

[15] Shen XK, Ma PP, Hu Y, Xu GQ, Xu K, Chen WZ, et al. Alendronate-loaded hydroxyapatite-TiO2 nanotubes for improved bone formation in osteoporotic rabbits. J Mater Chem B. 2016;4:1423-36.

[16] Protivinsky J, Appleford M, Strnad J, Helebrant A, Ong JL. Effect of chemically modified titanium surfaces on protein adsorption and osteoblast precursor cell behavior. The International journal of oral & maxillofacial implants. 2007;22:542-50.

[17] Jimbo R, Ivarsson M, Koskela A, Sul YT, Johansson CB. Protein adsorption to surface chemistry and crystal structure modification of titanium surfaces. Journal of oral & maxillofacial research. 2010;1:e3.

[18] Sethuraman A, Han M, Kane RS, Belfort G. Effect of surface wettability on the adhesion of proteins. Langmuir : the ACS journal of surfaces and colloids. 2004;20:7779-88.

[19] Roach P, Farrar D, Perry CC. Interpretation of protein adsorption: surface-induced conformational changes. Journal of the American Chemical Society. 2005;127:8168-73.

[20] Roach P, Farrar D, Perry CC. Surface tailoring for controlled protein adsorption: effect of topography at the nanometer scale and chemistry. Journal of the American Chemical Society. 2006;128:3939-45.

[21] Keller TF, Reichert J, Thanh TP, Adjiski R, Spiess L, Berzina-Cimdina L, et al. Facets of protein assembly on nanostructured titanium oxide surfaces. Acta biomaterialia. 2013;9:5810-20.

[22] Sousa SR, Manuela Bras M, Moradas-Ferreira P, Barbosa MA. Dynamics of fibronectin adsorption on TiO2 surfaces. Langmuir : the ACS journal of surfaces and colloids. 2007;23:7046-54.

[23] Karazisis D, Ballo AM, Petronis S, Agheli H, Emanuelsson L, Thomsen P, et al. The role of well-defined nanotopography of titanium implants on osseointegration: cellular and molecular events in vivo. International journal of nanomedicine. 2016;11:1367-82.

[24] Berglundh T, Gotfredsen K, Zitzmann NU, Lang NP, Lindhe J. Spontaneous progression of ligature induced peri-implantitis at implants with different surface roughness: an experimental study in dogs. Clinical oral implants research. 2007;18:655-61.

[25] Schmidlin PR, Muller P, Attin T, Wieland M, Hofer D, Guggenheim B. Polyspecies biofilm formation on implant surfaces with different surface characteristics. Journal of applied oral science : revista FOB. 2013;21:48-55.

[26] Alghamdi HS, van Oirschot BA, Bosco R, van den Beucken JJ, Aldosari AA, Anil S, et al. Biological response to titanium implants coated with nanocrystals calcium phosphate or type 1 collagen in a dog model. Clinical oral implants research. 2013;24:475-83.

[27] Lee SW, Hahn BD, Kang TY, Lee MJ, Choi JY, Kim MK, et al. Hydroxyapatite and collagen combination-coated dental implants display better bone formation in the peri-implant area than the same combination plus bone

morphogenetic protein-2-coated implants, hydroxyapatite only coated implants, and uncoated implants. Journal of oral and maxillofacial surgery : official journal of the American Association of Oral and Maxillofacial Surgeons. 2014;72:53-60.

[28] Hunziker EB, Enggist L, Kuffer A, Buser D, Liu Y. Osseointegration: the slow delivery of BMP-2 enhances osteoinductivity. Bone. 2012;51:98-106.

[29] Peterson AM, Pilz-Allen C, Kolesnikova T, Mohwald H, Shchukin D. Growth factor release from polyelectrolyte-coated titanium for implant applications. ACS applied materials & interfaces. 2014;6:1866-71.

[30] Chang YC, Lee WF, Feng SW, Huang HM, Lin CT, Teng NC, et al. In Vitro Analysis of Fibronectin-Modified Titanium Surfaces. PloS one. 2016;11:e0146219.

[31] Chua PH, Neoh KG, Kang ET, Wang W. Surface functionalization of titanium with hyaluronic acid/chitosan polyelectrolyte multilayers and RGD for promoting osteoblast functions and inhibiting bacterial adhesion. Biomaterials. 2008;29:1412-21.

[32] Goodman SB, Yao Z, Keeney M, Yang F. The future of biologic coatings for orthopaedic implants. Biomaterials. 2013;34:3174-83.

[33] Luttrell T, Halpegamage S, Tao J, Kramer A, Sutter E, Batzill M. Why is anatase a better photocatalyst than rutile?--Model studies on epitaxial TiO2 films. Scientific reports. 2014;4:4043.

[34] Ahmed MH, Byrne JA, Keyes TE, Ahmed W, Elhissi A, Jackson MJ, et al. Characteristics and applications of titanium oxide as a biomaterial for medical implants. Woodh Publ Rev-Mech. 2012:1-113.

[35] Att W, Hori N, Takeuchi M, Ouyang J, Yang Y, Anpo M, et al. Time-dependent degradation of titanium osteoconductivity: an implication of biological aging of implant materials. Biomaterials. 2009;30:5352-63.

[36] Massaro C, Rotolo P, De Riccardis F, Milella E, Napoli A, Wieland M, et al. Comparative investigation of the surface properties of commercial titanium dental implants. Part I: chemical composition. Journal of materials science Materials in medicine. 2002;13:535-48.

[37] Shibata Y, Suzuki D, Omori S, Tanaka R, Murakami A, Kataoka Y, et al. The characteristics of in vitro biological activity of titanium surfaces anodically oxidized in chloride solutions. Biomaterials. 2010;31:8546-55.

[38] Rajagopal G, Maruthamuthu S, Mohanan S, Palaniswamy N. Biocidal effects of photocatalytic semiconductor TiO2. Colloids and surfaces B, Biointerfaces. 2006;51:107-11.

[39] Mills A, LeHunte S. An overview of semiconductor photocatalysis. J Photoch Photobio A. 1997;108:1-35.

[40] Ajmal A, Majeed I, Malik RN, Idriss H, Nadeem MA. Principles and mechanisms of photocatalytic dye degradation on TiO2 based photocatalysts: a comparative overview. Rsc Adv. 2014;4:37003-26.

[41] Rupp F, Haupt M, Klostermann H, Kim HS, Eichler M, Peetsch A, et al. Multifunctional nature of UV-irradiated nanocrystalline anatase thin films for biomedical applications. Acta biomaterialia. 2010;6:4566-77.

[42] Nakata K, Fujishima A. TiO2 photocatalysis: Design and applications. J Photoch Photobio C. 2012;13:169-89.

[43] Rupp F, Scheideler L, Geis-Gerstorfer J. Effect of heterogenic surfaces on contact angle hysteresis: Dynamic contact angle analysis in material sciences. Chem Eng Technol. 2002;25:877-82.

[44] Aita H, Hori N, Takeuchi M, Suzuki T, Yamada M, Anpo M, et al. The effect of ultraviolet functionalization of titanium on integration with bone. Biomaterials. 2009;30:1015-25.

[45] Al Qahtani MSA, Wu YY, Spintzyk S, Krieg P, Killinger A, Schweizer E, et al. UV-A and UV-C light induced hydrophilization of dental implants. Dental Materials. 2015;31:E157-E67.

[46] Takata Y, Hidaka S, Masuda M, Ito T. Pool boiling on a superhydrophilic surface. Int J Energ Res. 2003;27:111-9.

[47] Miyauchi M, Nakajima A, Fujishima A, Hashimoto K, Watanabe T. Photoinduced Surface Reactions on TiO2 and SrTiO3 Films: Photocatalytic Oxidation and Photoinduced Hydrophilicity. Chem Mater. 2000;12:3-5.

[48] Hirakawa Y, Jimbo R, Shibata Y, Watanabe I, Wennerberg A, Sawase T. Accelerated bone formation on photo-induced hydrophilic titanium implants: an experimental study in the dog mandible. Clinical oral implants research. 2013;24 Suppl A100:139-44.

[49] Klinger A, Steinberg D, Kohavi D, Sela MN. Mechanism of adsorption of human albumin to titanium in vitro. Journal of biomedical materials research. 1997;36:387-92.

[50] Iwasa F, Hori N, Ueno T, Minamikawa H, Yamada M, Ogawa T. Enhancement of osteoblast adhesion to UV-photofunctionalized titanium via an electrostatic mechanism. Biomaterials. 2010;31:2717-27.

[51] Hori N, Ueno T, Minamikawa H, Iwasa F, Yoshino F, Kimoto K, et al. Electrostatic control of protein adsorption on UV-photofunctionalized titanium. Acta biomaterialia. 2010;6:4175-80.

[52] Miyauchi T, Yamada M, Yamamoto A, Iwasa F, Suzawa T, Kamijo R, et al. The enhanced characteristics of osteoblast adhesion to photofunctionalized nanoscale TiO2 layers on biomaterials surfaces. Biomaterials. 2010;31:3827-39.

[53] Shayan M, Jung Y, Huang PS, Moradi M, Plakseychuk AY, Lee JK, et al. Improved osteoblast response to UV-irradiated PMMA/TiO2 nanocomposites with controllable wettability. Journal of materials science Materials in medicine. 2014;25:2721-30.

[54] Tsukimura N, Yamada M, Iwasa F, Minamikawa H, Att W, Ueno T, et al. Synergistic effects of UV photofunctionalization and micro-nano hybrid

topography on the biological properties of titanium. Biomaterials. 2011;32:4358-68.

[55] Hori N, Iwasa F, Tsukimura N, Sugita Y, Ueno T, Kojima N, et al. Effects of UV photofunctionalization on the nanotopography enhanced initial bioactivity of titanium. Acta biomaterialia. 2011;7:3679-91.

[56] Kawano T, Prananingrum W, Ishida Y, Goto T, Naito Y, Watanabe M, et al. Blue-violet laser modification of titania treated titanium: antibacterial and osteo-inductive effects. PloS one. 2013;8:e84327.

[57] Sandhu D, Kheur D, Kheur D. Comparative evaluation of the ISQ trends, clinical performance and survival of photofunctionalized & untreated dental implants – A split mouth study. Clinical oral implants research. 2015;26:184-.

[58] Sennerby L, Meredith N. Implant stability measurements using resonance frequency analysis: biological and biomechanical aspects and clinical implications. Periodontology 2000. 2008;47:51-66.

[59] Buser D, Broggini N, Wieland M, Schenk RK, Denzer AJ, Cochran DL, et al. Enhanced bone apposition to a chemically modified SLA titanium surface. Journal of dental research. 2004;83:529-33.

[60] Olivares-Navarrete R, Hyzy SL, Hutton DL, Erdman CP, Wieland M, Boyan BD, et al. Direct and indirect effects of microstructured titanium substrates on the induction of mesenchymal stem cell differentiation towards the osteoblast lineage. Biomaterials. 2010;31:2728-35.

[61] Lee JW, An JH, Park SH, Chong JH, Kim GS, Han J, et al. Retrospective clinical study of an implant with a sandblasted, large-grit, acid-etched surface and internal connection: analysis of short-term success rate and marginal bone loss. Maxillofacial plastic and reconstructive surgery. 2016;38:42.

[62] Khang W, Feldman S, Hawley CE, Gunsolley J. A multi-center study comparing dual acid-etched and machined-surfaced implants in various bone qualities. Journal of periodontology. 2001;72:1384-90.

[63] Hansson S, Norton M. The relation between surface roughness and interfacial shear strength for bone-anchored implants. A mathematical model. Journal of biomechanics. 1999;32:829-36.

[64] Amini AR, Laurencin CT, Nukavarapu SP. Bone tissue engineering: recent advances and challenges. Critical reviews in biomedical engineering. 2012;40:363-408.

[65] Simon SR. Orthopaedic basic science: Amer Academy of Orthopaedic; 1994.

[66] Palin E, Liu HN, Webster TJ. Mimicking the nanofeatures of bone increases bone-forming cell adhesion and proliferation. Nanotechnology. 2005;16:1828-35.

[67] Teixeira AI, Abrams GA, Bertics PJ, Murphy CJ, Nealey PF. Epithelial contact guidance on well-defined micro- and nanostructured substrates. Journal of cell science. 2003;116:1881-92.

[68] Sato M, Sambito MA, Aslani A, Kalkhoran NM, Slamovich EB, Webster TJ. Increased osteoblast functions on undoped and yttrium-doped

nanocrystalline hydroxyapatite coatings on titanium. Biomaterials. 2006;27:2358-69.

[69] Yao C, Slamovich EB, Webster TJ. Enhanced osteoblast functions on anodized titanium with nanotube-like structures. Journal of biomedical materials research Part A. 2008;85:157-66.

[70] Oh S, Daraio C, Chen LH, Pisanic TR, Finones RR, Jin S. Significantly accelerated osteoblast cell growth on aligned TiO2 nanotubes. Journal of biomedical materials research Part A. 2006;78:97-103.

[71] Meirelles L, Arvidsson A, Albrektsson T, Wennerberg A. Increased bone formation to unstable nano rough titanium implants. Clinical oral implants research. 2007;18:326-32.

[72] Akpan UG, Hameed BH. Parameters affecting the photocatalytic degradation of dyes using TiO2-based photocatalysts: A review. Journal of hazardous materials. 2009;170:520-9.

[73] Lorenzetti M, Pellicer E, Sort J, Baro MD, Kovac J, Novak S, et al. Improvement to the Corrosion Resistance of Ti-Based Implants Using Hydrothermally Synthesized Nanostructured Anatase Coatings. Materials. 2014;7:180-94.

[74] Montazerozohori M, Nasr-Esfahani M, Joohari S. Photocatalytic Degradation of an Organic Dye in Some Aqueous Buffer Solutions Using Nano Titanium Dioxide: A Kinetic Study. Environ Prot Eng. 2012;38:45-55.

[75] Rochkind M, Pasternak S, Paz Y. Using Dyes for Evaluating Photocatalytic Properties: A Critical Review. Molecules. 2015;20:88-110.

[76] Xu NP, Shi ZF, Fan YQ, Dong JH, Shi J, Hu MZC. Effects of particle size of TiO2 on photocatalytic degradation of methylene blue in aqueous suspensions. Ind Eng Chem Res. 1999;38:373-9.

[77] L. Scheideler L RF, Füger C, Denzer A, Geis-Gerstorfer J. Anatase coating of blasted/etched titanium implant surfaces promotes metabolic activity and cell proliferation of human osteoblasts. Poster 4th International Symposium Interface Biology of Implants; Warnemünde, Germany. 9-11 May 2012.

[78] Bang SM, Moon HJ, Kwon YD, Yoo JY, Pae A, Kwon IK. Osteoblastic and osteoclastic differentiation on SLA and hydrophilic modified SLA titanium surfaces. Clinical oral implants research. 2014;25:831-7.

[79] Eriksson C, Nygren H, Ohlson K. Implantation of hydrophilic and hydrophobic titanium discs in rat tibia: cellular reactions on the surfaces during the first 3 weeks in bone. Biomaterials. 2004;25:4759-66.

[80] Hayashi R, Ueno T, Migita S, Tsutsumi Y, Doi H, Ogawa T, et al. Hydrocarbon Deposition Attenuates Osteoblast Activity on Titanium. Journal of dental research. 2014;93:698-703.

[81] Fujishima A, Zhang XT, Tryk DA. TiO2 photocatalysis and related surface phenomena. Surf Sci Rep. 2008;63:515-82.

[82] Wendt S, Schaub R, Matthiesen J, Vestergaard EK, Wahlström E, Rasmussen MD, et al. Oxygen vacancies on TiO2(110) and their interaction

with H2O and O2: A combined high-resolution STM and DFT study. Surface Science. 2005;598:226-45.

[83] Takeuchi M, Sakamoto K, Martra G, Coluccia S, Anpo M. Mechanism of photoinduced superhydrophilicity on the TiO2 photocatalyst surface. The journal of physical chemistry B. 2005;109:15422-8.

[84] Feng B, Weng J, Yang BC, Qu SX, Zhang XD. Characterization of surface oxide films on titanium and adhesion of osteoblast. Biomaterials. 2003;24:4663-70.

[85] Pankov R, Yamada KM. Fibronectin at a glance. Journal of cell science. 2002;115:3861-3.

[86] Wei J, Igarashi T, Okumori N, Igarashi T, Maetani T, Liu B, et al. Influence of surface wettability on competitive protein adsorption and initial attachment of osteoblasts. Biomedical materials. 2009;4:045002.

[87] Howe A, Aplin AE, Alahari SK, Juliano RL. Integrin signaling and cell growth control. Current opinion in cell biology. 1998;10:220-31.

[88] Pearson G, Robinson F, Beers Gibson T, Xu BE, Karandikar M, Berman K, et al. Mitogen-activated protein (MAP) kinase pathways: regulation and physiological functions. Endocrine reviews. 2001;22:153-83.

[89] Ge C, Yang Q, Zhao G, Yu H, Kirkwood KL, Franceschi RT. Interactions between extracellular signal-regulated kinase 1/2 and p38 MAP kinase pathways in the control of RUNX2 phosphorylation and transcriptional activity. Journal of bone and mineral research : the official journal of the American Society for Bone and Mineral Research. 2012;27:538-51.

[90] Moreno-Layseca P, Streuli CH. Signalling pathways linking integrins with cell cycle progression. Matrix biology : journal of the International Society for Matrix Biology. 2014;34:144-53.

[91] Aita H, Att W, Ueno T, Yamada M, Hori N, Iwasa F, et al. Ultraviolet light-mediated photofunctionalization of titanium to promote human mesenchymal stem cell migration, attachment, proliferation and differentiation. Acta biomaterialia. 2009;5:3247-57.

[92] Wennerberg A, Galli S, Albrektsson T. Current knowledge about the hydrophilic and nanostructured SLActive surface. Clinical, cosmetic and investigational dentistry. 2011;3:59-67.

[93] Ogawa T. Ultraviolet photofunctionalization of titanium implants. The International journal of oral & maxillofacial implants. 2014;29:e95-102.

[94] Att W, Ogawa T. Biological aging of implant surfaces and their restoration with ultraviolet light treatment: a novel understanding of osseointegration. The International journal of oral & maxillofacial implants. 2012;27:753-61.

[95] Lee JH, Ogawa T. The biological aging of titanium implants. Implant dentistry. 2012;21:415-21.

[96] Son HS, Ko G, Zoh KD. Kinetics and mechanism of photolysis and TiO2 photocatalysis of triclosan. Journal of hazardous materials. 2009;166:954-60.

[97] Gao Y, Liu Y, Zhou L, Guo Z, Rong M, Liu X, et al. The effects of different wavelength UV photofunctionalization on micro-arc oxidized titanium. PloS one. 2013;8:e68086.

[98] Jin FY, Chu PK, Wang K, Zhao J, Huang AP, Tong HH. Thermal stability of titania films prepared on titanium by micro-arc oxidation. Mat Sci Eng a-Struct. 2008;476:78-82.

[99] Hamblin MR, Huang Y. Handbook of Photomedicine: CRC Press; 2013.

[100] Rastogi RP, Richa, Kumar A, Tyagi MB, Sinha RP. Molecular mechanisms of ultraviolet radiation-induced DNA damage and repair. Journal of nucleic acids. 2010;2010:592980.

[101] Lang NP, Berglundh T, Heitz-Mayfield LJ, Pjetursson BE, Salvi GE, Sanz M. Consensus statements and recommended clinical procedures regarding implant survival and complications. Int J Oral Max Impl. 2004;19:150-4.

[102] Vangipuram R, Feldman SR. Ultraviolet phototherapy for cutaneous diseases: a concise review. Oral diseases. 2016;22:253-9.

[103] Kreuter A, Hyun J, Stucker M, Sommer A, Altmeyer P, Gambichler T. A randomized controlled study of low-dose UVA1, medium-dose UVA1, and narrowband UVB phototherapy in the treatment of localized scleroderma. Journal of the American Academy of Dermatology. 2006;54:440-7.

[104] Farahnik B, Nakamura M, Singh RK, Abrouk M, Zhu TH, Lee KM, et al. The Patient's Guide to Psoriasis Treatment. Part 2: PUVA Phototherapy. Dermatology and therapy. 2016;6:315-24.

[105] Wu Y, Geis-Gerstorfer J, Scheideler L, Rupp F. Photocatalytic antibacterial effects on TiO2-anatase upon UV-A and UV-A/VIS threshold irradiation. Biofouling. 2016;32:583-95.

[106] Smeets R, Stadlinger B, Schwarz F, Beck-Broichsitter B, Jung O, Precht C, et al. Impact of Dental Implant Surface Modifications on Osseointegration. BioMed research international. 2016;2016:6285620.

[107] Boyan BD, Lossdorfer S, Wang L, Zhao G, Lohmann CH, Cochran DL, et al. Osteoblasts generate an osteogenic microenvironment when grown on surfaces with rough microtopographies. European cells & materials. 2003;6:22-7.

[108] Shibata Y, Tanimoto Y. A review of improved fixation methods for dental implants. Part I: Surface optimization for rapid osseointegration. Journal of prosthodontic research. 2015;59:20-33.

[109] Hayes JS, Khan IM, Archer CW, Richards RG. The role of surface microtopography in the modulation of osteoblast differentiation. European cells & materials. 2010;20:98-108.

[110] Trisi P, Lazzara R, Rao W, Rebaudi A. Bone-implant contact and bone quality: evaluation of expected and actual bone contact on machined and osseotite implant surfaces. The International journal of periodontics & restorative dentistry. 2002;22:535-45.

[111] Abrahamsson I, Berglundh T, Linder E, Lang NP, Lindhe J. Early bone formation adjacent to rough and turned endosseous implant surfaces. An experimental study in the dog. Clinical oral implants research. 2004;15:381-92.

[112] Albrektsson T, Wennerberg A. Oral implant surfaces: Part 1--review focusing on topographic and chemical properties of different surfaces and in vivo responses to them. The International journal of prosthodontics. 2004;17:536-43.

[113] Arvidsson A, Sater BA, Wennerberg A. The role of functional parameters for topographical characterization of bone-anchored implants. Clinical implant dentistry and related research. 2006;8:70-6.

[114] Ramaglia L, Postiglione L, Di Spigna G, Capece G, Salzano S, Rossi G. Sandblasted-acid-etched titanium surface influences in vitro the biological behavior of SaOS-2 human osteoblast-like cells. Dental materials journal. 2011;30:183-92.

[115] Wang JH, Thampatty BP, Lin JS, Im HJ. Mechanoregulation of gene expression in fibroblasts. Gene. 2007;391:1-15.

[116] Marie PJ, Hay E, Saidak Z. Integrin and cadherin signaling in bone: role and potential therapeutic targets. Trends in endocrinology and metabolism: TEM. 2014;25:567-75.

[117] Karazisis D, Petronis S, Agheli H, Emanuelsson L, Norlindh B, Johansson A, et al. The influence of controlled surface nanotopography on the early biological events of osseointegration. Acta biomaterialia. 2017;53:559-71.

[118] L MSC-R, M SF, L NT, E PF, H BL, P TdO, et al. Titanium With Nanotopography Induces Osteoblast Differentiation by Regulating Endogenous Bone Morphogenetic Protein Expression and Signaling Pathway. Journal of cellular biochemistry. 2016;117:1718-26.

[119] He J, Zhou W, Zhou X, Zhong X, Zhang X, Wan P, et al. The anatase phase of nanotopography titania plays an important role on osteoblast cell morphology and proliferation. Journal of materials science Materials in medicine. 2008;19:3465-72.

[120] Wang K, Bruce A, Mezan R, Kadiyala A, Wang L, Dawson J, et al. Nanotopographical Modulation of Cell Function through Nuclear Deformation. ACS applied materials & interfaces. 2016;8:5082-92.

[121] Dalby MJ, Gadegaard N, Tare R, Andar A, Riehle MO, Herzyk P, et al. The control of human mesenchymal cell differentiation using nanoscale symmetry and disorder. Nature materials. 2007;6:997-1003.

[122] Kunzler TP, Huwiler C, Drobek T, Voros J, Spencer ND. Systematic study of osteoblast response to nanotopography by means of nanoparticle-density gradients. Biomaterials. 2007;28:5000-6.

[123] Ogawa T, Saruwatari L, Takeuchi K, Aita H, Ohno N. Ti nano-nodular structuring for bone integration and regeneration. Journal of dental research. 2008;87:751-6.

[124] Wennerberg A, Jimbo R, Stubinger S, Obrecht M, Dard M, Berner S. Nanostructures and hydrophilicity influence osseointegration: a biomechanical study in the rabbit tibia. Clinical oral implants research. 2014;25:1041-50.

[125] Wennerberg A, Svanborg LM, Berner S, Andersson M. Spontaneously formed nanostructures on titanium surfaces. Clinical oral implants research. 2013;24:203-9.

[126] Gittens RA, McLachlan T, Olivares-Navarrete R, Cai Y, Berner S, Tannenbaum R, et al. The effects of combined micron-/submicron-scale surface roughness and nanoscale features on cell proliferation and differentiation. Biomaterials. 2011;32:3395-403.

[127] Dalby MJ, Gadegaard N, Tare R, Andar A, Riehle MO, Herzyk P, et al. The control of human mesenchymal cell differentiation using nanoscale symmetry and disorder. Nature materials. 2007;6:997-1003.

[128] Gittens RA, Scheideler L, Rupp F, Hyzy SL, Geis-Gerstorfer J, Schwartz Z, et al. A review on the wettability of dental implant surfaces II: Biological and clinical aspects. Acta biomaterialia. 2014;10:2907-18.

Declaration of Contribution

This study was performed in the Section of Medical Material Science and Technology, University Hospital Tübingen under the supervision of Prof. Dr. Jürgen Geis-Gerstorfer.

Prof. Dr. Jürgen Geis-Gerstorfer, PD Dr. Frank Rupp and Dr. Lutz Scheideler were involved in the development of concepts and hypotheses, and have supervised the work. Dr. Lutz Scheideler has corrected the manuscript.

The Dentaurum GmbH & Co. KG (Ispringen) has provided the sandblasted titanium samples and the sandblasted and acid-etched samples. Prof. Dr. rer. nat. Andreas Killinger and Dipl.–Ing. Peter Krieg (Institute for Manufacturing Technologies of Ceramic Components and Composites, Stuttgart) have performed the SPS and PLC modifications and the 3D roughness measurement. They also have provided the SEM images at 10.000x and 50.000 x magnifications. Dr. Gunther Richter (Max-Planck-Institute for Intelligent Systems, Stuttgart) has provided the PVD modification.

Mr. Ernst Schweizer has provided the rest of SEM images and carried out the ICP-OES analysis. Mr. Sebastian Spintzyk was involved in the 2D roughness measurement. Ms. Christine Schille has carried out the immersion test. Ms. Ingrid Stephan was involved in the contact angle measurement. Ms. Cornelia Füger and Ms. Evi Kimmerle-Müller have provided the osteoblasts.

I myself have carried out all other experiments, data analysis, and statistical evaluation. I hereby declare that the thesis submitted is my own unaided work. All direct or indirect sources used are acknowledged as references.

Tuebingen

Lanchen Liang

Acknowledgment

First, I thank my academic supervisor, Prof. Dr. Jürgen Geis-Gerstorfer, for accepting me into his group. With his support, I gain a life-enhancing study experience by engaging in new ideas, attending at various conferences, and enjoying intellectual freedom in my work.

Furthermore, I was fortunate to have the chance to work with PD Dr. Frank Rupp and Dr. Lutz Scheideler. I greatly benefited from their keen scientific insight, and the ability to transform complex ideas into simple terms. I thank them for their systematic guidance for training me in the scientific field.

I acknowledge my sincere gratitude to my colleagues Mr. Ernst Schweizer, Mr. Sebastian Spintzyk, Ms. Christine Schille, Ms. Ingrid Stephan, Ms. Cornelia Füger and Ms. Evi Kimmerle-Müller, who patiently taught me the laboratory techniques. I also wish to thank all of my colleagues for the help and support, for the fun time I had in the MWT.

I am grateful to Prof. Dr. rer. nat. Andreas Killinger, Dipl.–Ing. Peter Krieg, Dr. Gunther Richter, and the Dentaurum GmbH & Co. for their kind cooperation that makes this thesis possible.

With special thanks to the Chinese Scholarship Council for providing me the financial assistance.

Additionally, I profoundly appreciate Prof. Dr. Heiner Weber for his cordial concern and help. I would also like to thank my committee member Professor Dr. Dr. Michael Krimmel for his interest in my work.

Last but not the least, I am deeply grateful to my beloved parents, Yanling Cui and Wenyu Liang, who provide me moral support in my life. I am also grateful to my other family members and friends who have supported me along the way.

Curriculum Vitae

Personal Information

Name: Lanchen Liang

Gender: Female

Date of birth: 27.11.1989

Nationality: Chinese

Education

09. 2004 – 06. 2007	Shenzhen Middle School, Guangdong Province
09. 2007 – 06. 2012	School of Stomatology, Sun Yat-sen University, Bachelor Degree
09. 2012 – 06. 2014	School of Stomatology, Sun Yat-sen University, Master Degree
08. 2013	National Dental Board Examinations, China
07. 2014 – 08. 2014	German Language Course, Guangdong University of Foreign Studies
since 10. 2014	Department of Prosthodontics and Section "Medical Materials and Technology", University Hospital Tuebingen, Doctor Degree

Science Activities and Scholarships

- Poster presentation of <Influence of Different Anatase Surface Modifications on Cellular Reactions of Human Osteoblasts> at the fifth International Symposium Interface Biology of Implants (IBI), Rostock, 2015

- Poster presentation of <Corrosion Resistance of Differently Manufactured Anatase Coatings for Titanium Implants> at the annual conference of the 40th European Prosthodontic Association (EPA) and the 65th German Society for Prosthetic Dentistry and Biomaterials (DGPro), Halle, 2016

- Scholarship from the Chinese Scholarship Council, 2014 – 2017

- Scholarship from the Sun Yat-sun University, 2008 – 2012